



THE UNIVERSITY OF
MELBOURNE

HIGH RESOLUTION PHASE CONTRAST X-RAY RADIOGRAPHY

by

Benedicta Dewi Arhatari

A thesis submitted in total fulfilment of
the requirements
of the degree of Doctor of Philosophy

School of Physics
University of Melbourne
Australia

January 2006

Abstract

High Resolution Phase Contrast X-ray Radiography

Benedicta Dewi Arhatari

University of Melbourne

Supervisors: Keith A. Nugent and Andrew G. Peele

2006

The conventional approach for x-ray radiography is absorption contrast. In recent years a new approach that eliminates the usual requirement for absorption and allows the visualization of phase based on refractive index features in a material has been demonstrated. This so-called "phase contrast imaging" has now been applied using a wide range of radiation and samples. In this work we are motivated by the need to find optimal conditions for achieving high quality phase contrast images. We consider image formation using the free space propagation of x-rays from a point source passing through a sample. This imaging model is a lens-less configuration and, as such, is very useful for x-ray wavelengths where lenses are difficult to fabricate. Although no lenses are used, image magnification is still achieved due to the expansion of the wavefront as it propagates from the point source illumination. The short wavelength and penetrating power of x-rays make them ideal for non-destructive studies of microscopic samples. However, these techniques are also important for investigating larger, non-microscopic samples.

An analysis, based on the sensitivity of the method to different feature sizes in the object, was used to successfully develop an image contrast model. It is developed for pure phase samples and samples with a small amount of absorption. The effects of partial coherence are explicitly incorporated. The result of the model is a prediction of the visibility of features of a certain size, which is compared with experimental results. The model gives rise to an objective filtering criterion for optimization of image quality and which allows for the combination of retrieved phase images in the presence of noise obtained at different distances to produce a single high quality image. The technique was applied experimentally using a laboratory micro-focus x-ray source illuminating a series of periodic spaced grid lines on a polyimide film and a series of copper grid meshes and excellent agreement with the model is found. We apply the technique to metal failure detection by imaging micro cracks and corrosion in an aluminium sheet. The model has also been extended to an analysis of 3D phase contrast tomography. We define a reconstruction quality factor which allows us to optimize the tomographic reconstruction for given feature sizes in an object.

This is to certify that

- the thesis comprises only my original work towards the PhD,
- due acknowledgement has been made in the text to all other material used,
- the thesis is less than 100,000 words in length, exclusive of tables, maps, bibliographies and appendices.

I authorize the Head of the School of Physics to make or have made a copy of this thesis to any person judged to have an acceptable reason for access to the information, i.e., for research, study or instruction.

Signature _____

Date _____

Acknowledgements

I have been fortunate to have Prof. Keith A. Nugent as my main supervisor who has a visceral enthusiasm for physics and its applications. His bright insight into my research has been the opening of a door to a closed room where I existed trapped in research problems. His invaluable guidance encouraged me to work independently, so that I was stimulated to explore freely my own ideas throughout this research project. I am very grateful to him for all his efforts, guidance, support and kindness over the last four years.

My co-supervisor Dr. Andrew G. Peele has always brought a fresh perspective and new ideas to discussions. His excellent ability in numerical computation and his deeply incisive approach in theory and experimental physics was very important to my research. He has followed my project with interest even after he moved to his new position at La Trobe University. He was enthusiastic and very patient when correcting my papers; especially because English is not my first language. He also acquired the tomography experimental data set for this thesis. I am very grateful to him for all his efforts and kindness over the last four years.

I would like to thank to Dr. Andrew Melatos as another member of my supervisory panel. He has followed my research progress with enthusiasm and showed readiness to help. I would like to acknowledge Dr. John Thornton (DSTO) for his contribution on published papers and for supplying aluminium sheets, one sample containing micro cracks and another sample containing corrosion. I would like to acknowledge Dr. Philip McMahon, Dr. Brendan Allman, Dr. D. L. Jacobson, and Dr. M. Arif for use of their neutron image data. I also thank Adrian P. Mancuso for producing phase retrieval images from the neutron data and for all his enthusiasm and help. I would like to acknowledge Dr. Andrew Stevenson (CSIRO) for supplying the gold lithographic mask. I also thank J.P. Hayes (Industrial Research Institute Swinburne) for providing the Kapton sample.

I would like to acknowledge the other members of the Optics Group, A/Prof. Robert Scholten, A/Prof. Ann Roberts and A/Prof. Christopher Chantler for their support of my project. My thanks also to the members of the Electronic and Mechanical Work-

shops of the School of Physics who provided some experimental components of this work.

My office has been a happy place to work thanks to the cheerful nature and humour of my friends Clare, Sean, Catherine, and Fotios. I have particularly enjoyed innumerable lunch times with Celine. I appreciate fruitful discussions with Garth and his help in expressing my research outline for this thesis in good sentences. More widely from the optics group, I also thank Nicoleta, Chanh, Justin, Bipin, Harry, Mark, Sam and Luke.

My deepest thanks to my parents and my family for their constant love and support. Thanks to my husband and my beloved twin daughters, through mostly happy but also some extremely difficult times.

*Glory be to the Father, and to the Son, and to the Holy Spirit.
As it was in the beginning, is now, and ever shall be, world without end.
Amen.*

Contents

1	Introduction	1
1.1	Statement of problem	1
1.1.1	Difference between prior and our research	2
1.2	Research outline	3
2	X-ray imaging	7
2.1	X-ray radiography	7
2.1.1	Phase contrast as a new approach	8
2.2	Basic theory	15
2.2.1	Fresnel diffraction integrals	15
2.2.2	Far field diffraction	21
2.2.3	Fresnel number in phase imaging	22
2.2.4	Two beam diffraction	24
2.2.5	Partial coherence theory in phase imaging	25
2.3	Phase visualization for x-rays	30
2.3.1	Diffraction enhanced imaging	30
2.3.2	Free space propagation phase contrast	32
2.4	Phase measurement	33
2.4.1	X-ray interferometry	33
2.4.2	Phase retrieval	35
3	Experimental facilities	49
3.1	X-ray source	49
3.1.1	X-ray spectrum	50

3.1.2	Focusing the x-ray source	52
3.1.3	Finite source size	54
3.2	X-ray detectors	59
3.2.1	Linearity and uniformity	59
3.2.2	Dark current	61
3.2.3	Signal to noise ratio	61
3.2.4	Quantum efficiency	62
3.2.5	Spread function	63
3.2.6	Dynamic range	64
3.3	Resolution and contrast	65
3.4	Synchrotron facility	66
4	Image modelling for transparent samples	71
4.1	Image formation model for a periodic object	71
4.2	Numerical model	76
4.3	Experimental test of the model	79
4.4	Objective image filtering	82
4.4.1	Implications for quantitative phase retrieval	87
4.4.2	Objective filtering for experimental phase retrieval data	92
5	Image modelling for complex objects	97
5.1	Image modelling for short propagation distances	98
5.1.1	Image formation model	98
5.1.2	Visibility for polychromatic phase contrast	102
5.1.3	Experimental test of the model	104
5.1.4	Applications	107
5.2	Image modelling for long propagation distances	114
5.2.1	Talbot effect	117
5.3	Simulation results	120
5.4	Conclusions	124

6	Tomography	125
6.1	Principle	126
6.1.1	Radon transform theory	127
6.1.2	Fourier slice theorem	128
6.1.3	Filtered back projection	130
6.2	Extended model for tomography	131
6.2.1	Sampling requirements	139
6.3	Numerical simulation	140
6.3.1	Effect of noise	145
6.4	Experiment results	147
7	Conclusion	155
7.1	Overview	155
7.2	Summary of results	156
7.3	Suggestions for further research	158
	Appendices	158
	A Publications	159
	Bibliography	159

Chapter 1

Introduction

1.1 Statement of problem

Phase methods may be categorized in two broad ways: the forward problem and the inverse problem. The forward problem describes systems for which the phase is rendered visible but does not yield quantitative information about the phase. Usually it is done by measuring intensity which contains phase information. In the forward problem, the wave equation and knowledge of the intensity and phase of the monochromatic wave in the sample plane are used to calculate the intensity distribution downstream of the sample (e.g. on the detector plane). The inverse problem, on the other hand, yields quantitative phase information with phase retrieval algorithms using the measured intensity. Quantitative information about the phase of the wave exiting the sample can, for example, be retrieved from a set of Fresnel diffraction patterns recorded at different distances. In this case, the free space propagation technique, the phase of the field is determined indirectly.

The free space propagation technique uses a unique contrast mechanism in comparison with other phase sensitive imaging techniques that has advantages concerning the simplicity of the experimental set-up, which requires no optics to form images. This technique is very useful at x-ray wavelengths where lenses are difficult to fabricate and, as there are no optical elements, produces no aberrations. This technique is applicable across a broad range of areas and has become an area of active development

[Sni95; Wil96; Ste99; McM01].

Using free space propagation based phase contrast, high quality imaging becomes a possibility for many research application. Good contrast with high resolution imaging is still being pursued in current x-ray imaging research [Bur84; Coe92; Sch94; Sni95; Pog97; Clo99a; McM03a]. The need to find a suitable solution for improving image quality and how it varies with different spatial frequencies has been a motivating factor in undertaking the present study. The aim of this research is therefore to develop an imaging model that explicitly incorporates a host of realistic experimental effects, including a partial coherence, and which can be applied to both pure phase samples and samples with some degree of absorption (complex objects).

Our investigation of x-ray imaging is done in the Fresnel regime, with a coaxial radiation source, sample and detector, and where the phase changes introduced to the radiation field by the sample are sufficiently small that the radiation remains paraxial. The visibility function is used extensively to characterize the optimal imaging conditions of the systems investigated in this thesis. The main approach in this research study will be to undertake theoretical analysis then to simulate numerically and to experimentally test the theoretical results using a micro focus x-ray laboratory source and a synchrotron source.

1.1.1 Difference between prior and our research

A general formalism for free space propagation based phase contrast using an x-ray point source has been developed [Gui77; Wil96; Pog97; Gur98; Wu03] that covers both the near Fresnel regime and the holographic regime. In this work we explicitly include the source spatial and spectral distribution into the formalism we developed . Another problem in x-ray phase contrast radiography imaging is that the x-ray radiography image for most objects will display a combination of phase and absorption contributions [Wu03; Pog97]. Some formalisms show only the role of phase or absorption contributions. In this work we develop a formalism that explicitly show separately the phase and absorption contributions to the image contrast.

1.2 Research outline

This investigation starts with an overview of past and present research concerning phase imaging and phase measurement (Chapter 2). Phase contrast imaging as a new approach in x-ray radiography is described and contrasted with the conventional absorption based methods. Some relevant basic theories about diffraction and imaging will be also discussed. Then, phase contrast imaging with hard x-rays as a forward problem is described. An overview of the existing phase retrieval methods to solve the inverse problem is also provided. We apply these phase retrieval methods throughout this study.

Chapter 3 describes the instrumentation we used in our experiment in phase sensitive radiography. The micro focus x-ray laboratory source we used is described in detail including its polychromatic energy spectrum, focusing of the source and its focal spot size. The sensitivity, noise characteristics and spatial resolution of the detector is described. The role of resolution and contrast as two important factors in quantifying the quality of an image are also discussed.

In the forward problem, one determines an equation which maps the complex wave function over the sample to the intensity distribution downstream of the sample. We simplify the matter for short propagation distances, where we are allowed linearize the Fresnel integral. This description of the phase contrast imaging technique is described in Chapter 4 for a pure phase sample. The model also incorporates the extended size of the source. This formalism is particularly suitable for a laboratory based micro focus x-ray source where the size of the source and magnification factor due to projection is important. In this case, the distance from the sample to the image plane is relatively large compared to the sample to source distance and results in Fresnel diffraction of the wave. The distances along the optical axis are very large compared to the transverse distances subtended by the image so that the small angle approximation can be used with good accuracy. This formulation predicts the contrast in the intensity distribution recorded at the image plane. After we tested the model experimentally using a series of periodic grid lines on a polyimide film, it was used to define an objective filtering criterion that can be applied to improve the image quality by combining phase images obtained at different propagation distances in order to recover a single high-quality

image. The application of this objective filtering criterion is presented for phase images in the presence of noise and using experimental neutron data.

In Chapter 5, an extended theoretical framework of the free space propagation phase contrast mechanism is developed for complex objects. That is, the object has both phase and absorption contrast. The complex index of refraction is used to express the distribution of intensity and phase directly after the sample. A sample illuminated by an extended source is imaged under geometric magnification some distance downstream of the sample. In this way, small samples can be imaged under high magnification without the need for lenses. The phase and absorption contributions are clearly apparent in this formalism as a function of object size and magnification. Simulation results are used to test this contrast formalism. The imaging model was tested using a series of copper grid meshes using a laboratory micro focus x-rays source to study the agreement between theory and experiment. The polychromaticity of the x-rays from a micro focus x-ray tube is explicitly investigated. In some cases, x-ray phase contrast experiments need to be more carefully designed to achieve an optimum contrast. Application of the developed model to image micro cracks and corrosion in aluminium sheet demonstrate that this analytical form of imaging is useful for identifying the optimum parameters for a given radiography experiment.

In Chapter 6, an analytical model is developed for 3D phase contrast tomography of a pure phase object. This is an extension of the two dimensional formalism in chapter 4. We model the angular dependent phase change which arises after repeating the projection radiography for a large number of angular positions of the sample. By measuring the intensities and by retrieving the phase distribution in each of the angular positions, we can reconstruct quantitative information about the 3D real refractive index distribution in the sample. The theory quantifies the reconstruction quality as a function of the spatial frequencies present in the object. A definition of image quality is introduced to provide a comparison between a reconstruction and the real distribution of the object. We then simulate a tomography experiment numerically, apply our model and hence assess the quality of the reconstruction. Experimental data of different diameter of polystyrene micro spheres is used in this work to verify the theory.

Finally, Chapter 7 summarizes the results of the research.

Chapter 2

X-ray imaging

This chapter describes an overview of past and present research concerning phase contrast imaging and some relevant theories. We begin in Section 2.1 with a brief description of conventional, absorption-based, x-ray radiography and include phase contrast as a new approach. In Section 2.2, we describe some relevant basic theories about diffraction and imaging important to this work. Various techniques for directly encoding phase information and measuring these intensities will be described in Section 2.3. Finally, phase measurement including phase retrieval techniques will be discussed in Section 2.4.

2.1 X-ray radiography

The enormous benefit of x-ray radiography has been recognized since the discovery of x-rays. X-ray radiography plays a central role in many diverse areas such as industrial inspections, medicine, materials science, chemistry and bio-medical imaging. Examples of x-ray radiography include: x-ray screening of baggage, mammography for tumor or cancer detection, x-ray radiology for medical diagnostic purposes, x-ray radiography for detecting failures in materials such as cracks, porosities and welding imperfections. Due to the high penetrating power of x-rays, this technique can be used as a non-destructive imaging technique. X-ray radiography can produce images of the internal structure of an object, without damaging the object [Bur84]. Due to their short

wavelength, x-rays can detect many kinds of microscopic scale samples.

For many years, the methods of x-ray radiography were based on the absorption of the radiation [Wat79; Hal79]. The contrast in these images is based on different x-ray absorption in different parts of the sample. In this approach, a film or other detector is placed directly after the sample, where the geometric shadow of highly absorbing parts of object produces intensity contrast. Conventional absorption radiography is not an ideal imaging technique as it is based on the inhomogeneous x-ray dose deposition and so can require long exposures and a relatively high x-ray dose to get good contrast. This is generally undesirable, especially in radiological clinical imaging that may involve significant risks for a patient.

X-ray absorption depends on the electron density of the material through which it is passing. X-rays are most strongly absorbed by high Z elements, while small density materials leads to poor contrast.

2.1.1 Phase contrast as a new approach

Absorption is not the only form of interaction between x-rays and matter. Phenomena like refraction relates to the phase of the x-ray waves and represents an interaction which does not deposit energy in the sample. So it is desirable to use phase shifts produced by the object as a new mechanism. Such phase shifts (or gradients) result in *refraction* of the x-ray beam, which in turn produces changes in the propagated intensity that can be detected. This effect is referred to as *phase contrast*. Furthermore, phase information becomes relatively more important at higher energies and will be discussed later in this section. Thus, at higher energies, the visibility of a weakly absorbing object can be very good due to phase contrast [Wil96]. Such a technique is also well suited to imaging features where there is a sudden change in material density and/or material thickness across the x-ray beam, such as for edges and material discontinuities [Clo97a].

Phase contrast imaging has recently been the subject of considerable worldwide research, using both laboratory sources and synchrotrons [Ste99; Sni95; Hwu02; Clo01; Mom03]. Work using a synchrotron has shown that refraction induced x-ray contrast is a very valuable analytical tool, allowing phase to be measured [Nug96; Gur00], and

allowing phase tomographic images to be acquired [Clo99a; McM03b; Spa99; May03]. In laboratory scale sources, Wilkins and co workers [Wil96; Gao98] showed that refraction can significantly augment the image contrast. Using an ultrafast laser-based system where hard x-rays can be produced much more cheaply than with a synchrotron, Toth and Kieffer [Tot05] showed that phase contrast imaging produced edge enhancement and revealed details that are difficult to observe or even undetectable in absorption images. For example, Figure 2.1 shows the difference between an absorption contrast and the corresponding phase contrast image of a bee taken with 17 keV photons. For industrial applications, thermal neutron phase radiography [All00; McM01] has also been developed. In such cases, phase contrast effects can enable the enhanced detection for cracks or edges in metal samples.

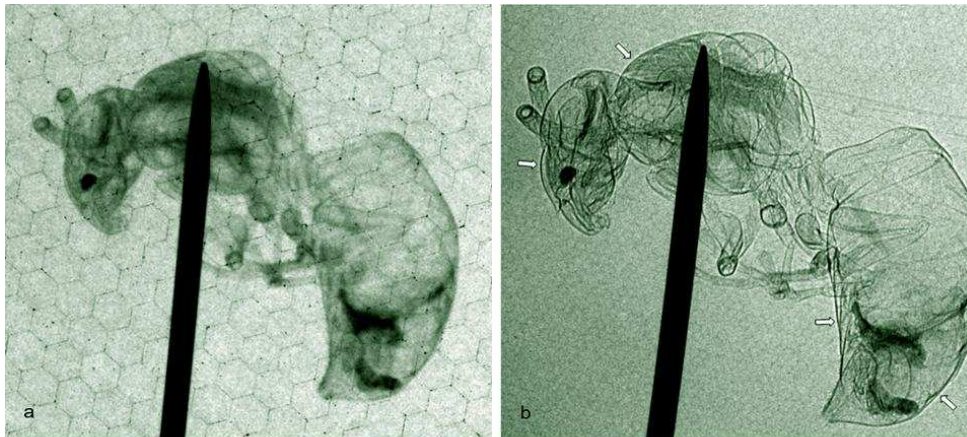


Figure 2.1: Direct comparison between (a) an absorption contrast and (b) a phase contrast imaging of a bee. The arrows indicate features enhanced by phase contrast imaging. Source [Tot05].

In summary, the visibility of an image can be significantly improved using phase contrast imaging. This image improvement is particularly noticeable for edges and is due to the larger variations in the real part of the complex refractive index across edges in the sample. Furthermore, for sources with sufficient spatial coherence, this phase contrast based imaging can provide excellent contrast for imaging at micrometer and sub micrometer scales.

Conceptual background

The full description of the interaction of an x-ray beam with a material can be reasonably complex. In the energy range in which we are interested -a few tenths to a few tens of a keV- the dominant processes include photoelectric absorption, refraction and coherent and incoherent scattering of the beam. The x-ray beam - sample interaction in our case for an amorphous material can be described in a simplified way by a complex transmission function. This is the complex ratio of the wave exiting and entering the sample. It is determined by the projection of the complex refractive index distribution, $n = 1 - \delta + i\beta$ ¹, within the sample. The refractive index of x-rays contains both a real part and imaginary part. The real part, δ , of the refractive index is responsible for refraction and results in a phase shift, while the magnitude of imaginary part, β , determines absorption.

The choice of $+i\beta$ is consistent with a wave description for a plane wave in a material of refractive index n , such that $f(z, t) = f_0 \exp[-i(\omega t - knz)]$, where f_0 is the amplitude, ω is the wave frequency, t is time, k is the wave number and z is the thickness or propagation distance. Substituting the complex refractive index into the plane wave equation we get:

$$f(z, t) = f_0 \exp[-i\omega t + ik(1 - \delta + i\beta)z]$$

$$f(z, t) = \underbrace{f_0 e^{(-i\omega t + ikz)}}_{\text{vacuum propg.}} \underbrace{e^{-ik\delta z}}_{\phi\text{-shift}} \underbrace{e^{-k\beta z}}_{\text{decay}} \quad (2.2)$$

where the first exponential factor represents the phase advance had the wave been propagated in vacuum. The second exponential factor represents the modified phase shift

¹The refractive index can be expressed as [Par54]:

$$1 - \delta + i\beta = 1 - \frac{r_0}{2\pi} \lambda^2 \sum_j n_j f_j \quad (2.1)$$

where $r_0 = 2.8179 \times 10^{-15} \text{m}$ is the classical electron radius, the summation is over all the atoms of form j , with n_j as the atom number density and f_j is the scattering factor for that atom. For forward scattering, the atomic scattering factor has the form: $f_j = f_1 - if_2$, where f_1 is for calculating the decrement of the real part of the refractive index and f_2 is for calculating the imaginary part.

We can use an effective β which includes the contribution to the beam that fails to enter a detector due to scattering as well as the photoelectric absorption. However, we found that for most of the materials and energies considered in this work the standard description (given in Equation 2.1) for photoelectric absorption was sufficient.

due to the medium and the third factor represents the decay of the wave amplitude. Therefore, the intensity and the phase of an x-ray wave are changed by an object as the x-rays travel through it.

In conventional radiography, image contrast is entirely due to the imaginary component of the complex refractive index, i.e., due to absorption. Such images ignore effects due to the real part of the refractive index, although in principle such effects are present. The absorption based contrast mechanism can require long exposures of the imaging radiation to detect small contrast changes. This is particularly true at higher energies because the imaginary part of the refractive index decreases dramatically for all elements at high x-ray energy.

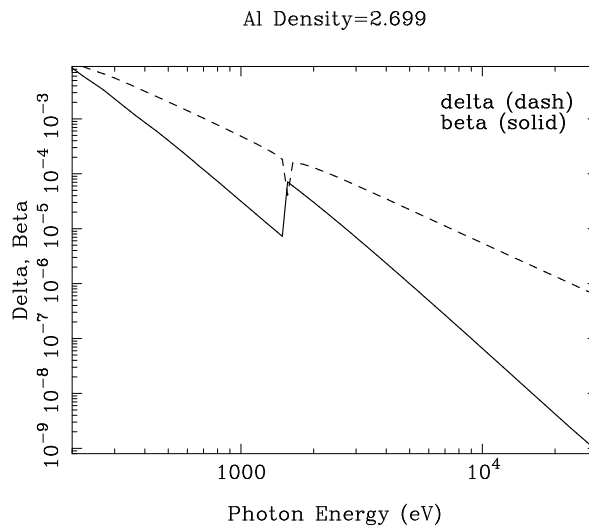


Figure 2.2: Comparison of the real part, δ , and imaginary part, β , of the complex refractive index for aluminium, as a function of the energy. Source http://www-cxro.lbl.gov/optical_constants/.

In the x-ray region, the real part of the index of refraction n , deviates only slightly from unity denoted by the term δ . X-rays that pass through materials of differing δ pick up different relative phases. The resulting phase shift is directly proportional to the projected electron density of the object. This process of refraction produces a distorted wave front and in turn creates contrast at a detector. Furthermore, the difference between the real part of the complex refractive index and the imaginary part is more important as the energy increases. This is shown in Figure 2.2 for aluminium. Compared to the imaginary part of the index of refraction, the real part becomes relatively more

important for harder x-rays. In the hard x-ray range (energies above 6 keV) the ratio of δ/β increases by about three order of magnitude. This means that the absorption contribution can be negligible while significant phase contrast is retained. Mechanisms for achieving and quantifying phase contrast will be discussed in more detailed in Section 2.3.

In phase contrast imaging the coherence of the beam is an important factor in determining image sharpness [Pag98]. In elementary optics, the field at a given point can in general be considered as a superposition of waves with different frequencies and different phases. The result is that the concept of phase tends to lose meaning in the absence of coherence. Coherence is the characteristic of a wave that allows to produce detectable interference and diffraction effects. The effect of spatially imperfect coherence in the beam is often to convolve the coherent intensity image with a function that is directly related in extent to the inverse of the coherence length [Nug91]. This effect can be seen as a blurring of the image [Hwu02]. The effect of temporally imperfect coherence (polychromaticity) in the beam is to also produce blurring in the image, though this can often be less important than the effect of spatial coherence [Pag98].

In a phase contrast image, the visibility improvement of edges between different regions (edge enhancement) is related to the propagation distance. Using the Cornu spiral method for the calculation of Fresnel edge diffraction [Hec97] of an opaque object, it is easily seen that the position of Fresnel diffraction maxima and minima is a function of the distance traveled in the propagation direction of the beam. Therefore, some propagation distance is necessary to be able to show the first intensity maximum, which produces the image edge enhancement, for refraction as well as for diffraction.

A theoretical description of image structure in terms of Kirchhoff formulation will be used here to demonstrate some of the important features of this technique. A hypothetical object was assumed which has a two dimensional intensity and phase distribution, as shown in Figure 2.3². The input intensity and phase have totally different distributions and have no relation to each other (a giraffe representing the intensity and a bird representing the phase shift). These different images were chosen to emphasize

²This figures are photograph taken by a friend, <http://www.paswindar.com/> and is used with permission.



Figure 2.3: (a) An image of a giraffe, representing the input intensity distribution varies from 0.9 (black) to 1 (white) in arbitrary units. (b) An image of a bird, representing the input phase shift distribution varies from 0 (black) to 2 (white) in radians.

the effect of propagation distance on absorption and phase features in an image. In practice, the phase distribution of an object will be strongly correlated with the absorption distribution. The images contain a variety of features of different sizes that will be helpful for showing how the propagation affects various features sizes. The dimensions of the object were $500\mu m$ square = 500 x 500 pixels. The x-ray wavelength was 1 Å. The input intensity transmission leaving the test object has a minimum transmission that $\sim 90\%$ of the maximum. The input phase shift leaving the test object varies from 0 (black) to 2 (white) in radians. Figure 2.4 shows the results of the image simulations. The contact radiograph, Figure 2.4(a), shows only absorption contrast (giraffe image). Phase contrast (the bird image) becomes more obvious with larger propagation distance, Figure 2.4(b), while absorption contrast becomes less important. Phase contrast finally dominates in Figure 2.4(c) where edge effect is clearly observable. The edge enhancement is evidenced by a characteristic black and white fringe. At this x-ray energy, the phase contrast effect would be clearly discernible at distances beginning from a few centimeters. In Figure 2.4(d) the multiple fringes associated with interference effects are starting to be seen. It is no longer possible to attribute the fringes to a specific edge of the sample. Figure 2.4(e) shows that interference effects dominate to the extent that the deformed image gives only rather indirect relation to the original phase structure.

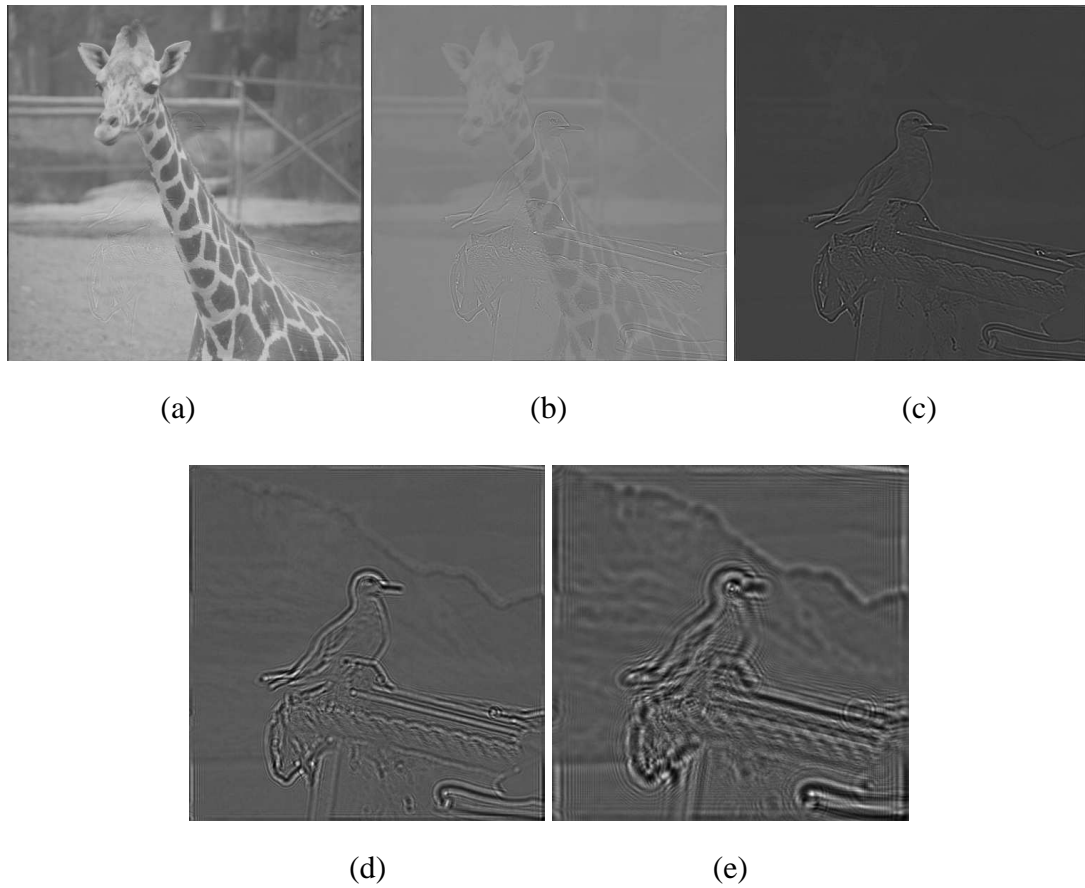


Figure 2.4: Simulation of x-ray images for propagation distance of (a) 0.001 m, (b) 0.01 m, (c) 0.1 m, (d) 0.4 m and (e) 1.4 m respectively.

Introduction of spatial frequency

The example in Figure 2.4(c) shows that the image obtained at a short propagation distance is very sensitive to features such as edges with short scale lengths (high spatial frequency components). Features with long scale lengths (low spatial frequencies) such as smooth variations in the object phase, start to have significant contrast at a longer propagation distance. This is why the mountain background begins to appear in Figure 2.4(d). A simple relation in terms of spatial frequencies for a pure phase object shows [Pog97; Clo01] that details of size a with a corresponding spatial frequency of $u = 1/a$ give optimum contrast at a distance, z , such that:

$$z = \frac{1}{2\lambda u^2}, \quad (2.3)$$

where λ is the wavelength of the imaging radiation. Thus, if we wish to see a feature size of $5\mu\text{m}$, with 1\AA x-rays, we need a propagation distance of 0.125 m to get an optimum contrast. Fortunately, this optimum distance generally falls in the range that is experimentally accessible. However, the optimum distance will intrinsically be difficult to achieve for extremely low spatial frequencies. This is usually due to the physical limitation in the experiment such as the size of the laboratory. Low spatial frequencies are thus typically imaged with less contrast. On the other hand, while extremely high spatial frequencies at their optimum distance would contribute strongly to the image, their representation in the image will be limited by the detector resolution.

2.2 Basic theory

2.2.1 Fresnel diffraction integrals

The Fresnel formulation of the scalar diffraction integral is used to describe two specific illuminating wave fields, i.e. the plane wave and the spherical wave cases. Consider coherent, monochromatic plane wave illumination of wavelength λ incident on a sample in the plane $z = 0$, as shown in Figure 2.5. In the paraxial approximation, the plane

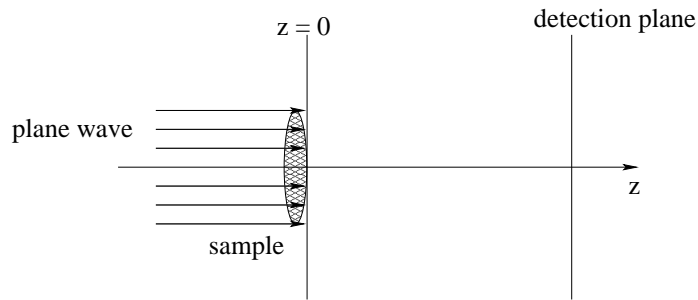


Figure 2.5: Plane wave illumination, the beam are parallel

wave function $f_p(x, y, z)$ at planes $z > 0$ with the $x-y$ plane in the transverse direction, is given by Fresnel diffraction theory [Cow95]:

$$f_p(x, y, z) = \frac{i}{\lambda z} \exp(ikz) \int \int S(X, Y, z = 0) \exp\left(\frac{i\pi}{\lambda z}[(x - X)^2 + (y - Y)^2]\right) dXdY \quad (2.4)$$

where $S(X, Y, z = 0)$ is the field immediately behind the object.

Now, consider the case where the sample is illuminated not by a plane wave but by a spherical wavefront originating from an ideal point source located at a distance z_1 from the plane $z = 0$, as illustrated in Figure 2.6. Illumination by a spherical wave is

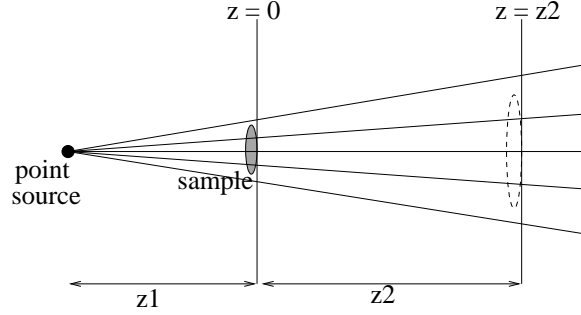


Figure 2.6: Spherical wave illumination

equivalent to adding an additional phase term to the sample corresponding to curvature of the incident wavefront, so that:

$$S_{curv}(x, y, z = 0) = S(x, y, z = 0) \exp\left[\frac{i\pi}{\lambda z_1}(x^2 + y^2)\right] \quad (2.5)$$

where a parabolic approximation have been made for the spherical wave front incident on the plane $z = 0$. Note that illumination of the object by a plane wave is equivalent to making $z_1 \rightarrow \infty$, in which that equation reduces to the expression for the wave field immediately behind the sample.

In the case when a parabolic approximation have been made for the spherical wave, the Taylor series expansion for points $\mathbf{r} = (x, y, z)$ is:

$$\begin{aligned} r &= (x^2 + y^2 + z^2)^{1/2} \\ &= z (1 + \theta^2)^{1/2} = z \left(1 + \frac{\theta^2}{2} - \frac{\theta^4}{8} + \dots\right) \\ &\approx z \left(1 + \frac{\theta^2}{2}\right) = z + \frac{x^2 + y^2}{2z} \end{aligned} \quad (2.6)$$

Where we use $\theta^2 = \frac{x^2 + y^2}{z^2} \ll 1$, when points \mathbf{r} are sufficiently close to the z axis but far away from the source or $z_1 \gg \sqrt{x^2 + y^2}$. The spherical wave eventually resembles the plane wave of $\exp(ikz)$, when $\theta^2 \ll 1$ and the term $\theta^4/8$ may be very small. The

approximation is therefore valid when:

$$\frac{kz\theta^4}{8} \ll 1 \quad \text{or} \quad (x^2 + y^2)^2 \ll z^3\lambda \quad (2.7)$$

For points (x, y) within a circle of radius a , centered about the z -axis, the validity condition is then:

$$a \ll \sqrt[4]{z^3\lambda} \quad (2.8)$$

This is a sufficient condition for the parabolic wave approximation to be valid.

The wave function in Equation 2.4 at the image plane z_2 now becomes, apart from a constant,

$$f_s(x, y, z_2) = \frac{i}{\lambda z_2} \exp(ikz_2) \int \int S(X, Y, z = 0) \exp\left(\frac{i\pi}{\lambda z_1}[X^2 + Y^2]\right) \exp\left(\frac{i\pi}{\lambda z_2}[(x - X)^2 + (y - Y)^2]\right) dXdY \quad (2.9)$$

Expanding the arguments in the second exponential inside the integral gives:

$$f_s(x, y, z_2) = \frac{i}{\lambda z_2} \exp(ikz_2) \exp\left(\frac{i\pi}{\lambda z_2}[x^2 + y^2]\right) \int \int S(X, Y, z = 0) \exp\left(\frac{i\pi}{\lambda z_1}[X^2 + Y^2]\right) \exp\left(\frac{i\pi}{\lambda z_2}[X^2 + Y^2]\right) \exp\left(-\frac{i2\pi}{\lambda z_2}[xX + yY]\right) dXdY \quad (2.10)$$

Rewriting Equation 2.10, we have:

$$f_s(x, y, z_2) = \frac{i}{\lambda z_2} \exp(ikz_2) \exp\left(\frac{i\pi}{\lambda z_2}[x^2 + y^2]\right) \int \int S(X, Y, z = 0) \exp\left(\frac{i\pi}{\lambda}[X^2 + Y^2]\left(\frac{1}{z_1} + \frac{1}{z_2}\right)\right) \exp\left(-\frac{i2\pi}{\lambda z_2}[xX + yY]\right) dXdY \quad (2.11)$$

This is the same expression that would result from an incident plane wave with an effective propagation distance z :

$$\frac{1}{z} = \frac{1}{z_1} + \frac{1}{z_2} \quad \text{or} \quad z = \frac{z_1 \cdot z_2}{z_1 + z_2} \quad \text{or} \quad z = \frac{z_2}{M} \quad (2.12)$$

Image magnification will also occur because of the geometrical projection. The magnification factor M , is given by:

$$M = \frac{z_1 + z_2}{z_1} \quad (2.13)$$

Substituting Equation 2.12 into Equation 2.11 we have:

$$f_s(x, y, z_2) = \frac{i}{\lambda M z} \exp(ikz_2) \exp\left(\frac{i\pi}{\lambda M z}[x^2 + y^2]\right) \iint S(X, Y, z=0) \exp\left(\frac{i\pi}{\lambda z}[X^2 + Y^2]\right) \exp\left(-\frac{i2\pi}{\lambda M z}[xX + yY]\right) dXdY \quad (2.14)$$

The point source intensity at distance z_2 is therefore identical (up to a constant factor) to the plane wave illuminated wave field a distance z beyond the object, magnified by the geometric magnification M . In the case of a large source-sample distance, $z_1 \rightarrow \infty$, the effective propagation distance z , is approximately equal to object detector distance z_2 and magnification factor is approximately equal to 1. If we substitute those parameters to Equation 2.14 we recover the plane wave illumination case.

For the case $z_2 \gg z_1$, the effective propagation distance z is to a good approximation equal to the point source to object distance z_1 . Varying the object to detector distance z_2 changes only the magnification of the diffraction pattern. This is the case where point projection microscopy works and the most important case for the work described in this thesis.

In summary, in the parabolic approximation, the wave function for a spherical wave front, f_s , can be simply expressed in terms of that produced by plane wave illumination, f_p , [Cow95]:

$$f_s(x, y, z_2) \sim f_p\left(\frac{x}{M}, \frac{y}{M}, \frac{z_2}{M}\right) \quad (2.15)$$

and in Fourier space transformation:

$$F_s(u, v, z_2) \sim F_p(Mu, Mv, \frac{z_2}{M}) \quad (2.16)$$

where the z dependence is explicitly retained and F is the Fourier transformation of the wave function f , using the convention:

$$\begin{aligned} F(\mathbf{u}) &= \frac{1}{2\pi} \int f(\mathbf{r}) e^{-i(\mathbf{u}\cdot\mathbf{r})} d\mathbf{r} \\ f(\mathbf{r}) &= \frac{1}{2\pi} \int F(\mathbf{u}) e^{i(\mathbf{u}\cdot\mathbf{r})} d\mathbf{u} \end{aligned} \quad (2.17)$$

The variables u, v represent spatial frequencies in the transverse planes where $\mathbf{u}^2 = u^2 + v^2$.

Comparison with the stringent condition in Equation 2.8, Turner [Tur04b] derived a new condition that extends the validity of the isomorphism (Equation 2.15) between the Fresnel diffraction intensity of an object illuminated with plane waves and of same object illuminated with a spherical wave. In the large magnification limit of $z_2 \gg z_1$, this condition is well approximated by [Tur04b]:

$$2a \ll \sqrt[4]{\lambda z_1^2 z_2} \quad (2.18)$$

This condition is valid even beyond the parabolic approximation due to some significant cancelation of errors in the higher order term in the expansion of a spherical wave.

Wave propagator

The propagation of the transmitted wave in free space over a propagation distance, is well described in the Fresnel approximation, using the Kirchhoff formulation by the convolution of the transmitted wave with a propagator function.

In the Kirchhoff formulation of scalar diffraction theory, a complex function representing a coherent, scalar, monochromatic optical plane wave field in a vacuum can be described as [Ban91]:

$$f_p(\mathbf{x}, t) = \exp[-i(\omega t - \mathbf{k} \cdot \mathbf{x})] \quad (2.19)$$

where \mathbf{k} is a wave vector which points in the direction of wave propagation. For a stationary field, we are concerned only with the spatial part of the equation, which satisfies the homogeneous Helmholtz equation:

$$(\nabla^2 + k^2) \exp[i\mathbf{k} \cdot \mathbf{x}] = 0 \quad (2.20)$$

where $\nabla^2 = \frac{\partial^2}{\partial x^2} + \frac{\partial^2}{\partial y^2} + \frac{\partial^2}{\partial z^2}$ is three dimensional Laplacian, and $k^2 = k_x^2 + k_y^2 + k_z^2$, so that $k_z = \pm \sqrt{k^2 - k_x^2 - k_y^2}$. The spatial part of the wave equation is then:

$$\begin{aligned} f_p(\mathbf{x}) &= \exp[i\mathbf{k} \cdot \mathbf{x}] \\ f_p(x, y, z) &= \exp i[k_x x + k_y y + k_z z] \\ f_p(x, y, z) &= \exp i[k_x x + k_y y + z \sqrt{k^2 - k_x^2 - k_y^2}] \end{aligned} \quad (2.21)$$

which is valid for a plane wave propagating in the positive z direction because we select only the positive solution to the square root for k_z . If we have a plane wave in the plane

$z = 0$ given by:

$$f_p(\mathbf{r}, 0) = \exp i[k_x x + k_y y] \quad (2.22)$$

where \mathbf{r} is in the $x - y$ plane perpendicular to the direction of propagation of the plane wave, then the plane wave in any other plane $z > 0$ is given by [Bar99]:

$$f_p(\mathbf{r}, z) = f_p(\mathbf{r}, 0) e^{iz\sqrt{k^2 - k_x^2 - k_y^2}} \quad (2.23)$$

The propagation of a plane wave shows a simple phase change relation with the transmitted beam. The knowledge of the propagation properties of a plane wave also enable us to propagate more complex fields. This is because Fourier proposed that any well-behaved disturbance may be decomposed into a continuous summation of plane wave elements of different frequencies, amplitudes and phases [Bar99]. Each of these elements will propagate according Equation 2.23. Denote the complex field in the plane $z = 0$ by $f(x, y, z = 0)$ and write its two dimensional Fourier transform as $\tilde{f}(k_x, k_y, z = 0)$. Then

$$\tilde{f}(k_x, k_y, z) = \frac{1}{2\pi} \int \int f(x, y, z) e^{i(k_x x + k_y y)} dx dy \quad (2.24)$$

The optical disturbance in any plane $z > 0$ is written as:

$$\tilde{f}(k_x, k_y, z) = e^{iz\sqrt{k^2 - k_x^2 - k_y^2}} \tilde{f}(k_x, k_y, z = 0) \quad (2.25)$$

The Fourier transform of the diffracted wave field in the plane $z > 0$ is given by multiplying the Fourier transform of the wave field in the plane $z = 0$ with the Kirchoff propagator $e^{iz\sqrt{k^2 - k_x^2 - k_y^2}}$.

Using the Fast Fourier Transform [Pre88] for a discrete data set that is sampled on a grid of $N \times N$ pixels with a pixel size of Δx , we rewrite Equation 2.25 as:

$$f(x, y, z) = \mathcal{F}^{-1} \exp \left(i2\pi z \sqrt{\frac{1}{\lambda^2} - \frac{i^2 + j^2}{N^2 \Delta x^2}} \right) \mathcal{F} f(x, y, z = 0) \quad (2.26)$$

where i, j are the pixel numbers in the k_x and k_y direction respectively in the range $[-N/2, N/2]$.

A detailed developed of the numerical implementation of Equation 2.25 can be found in the PhD thesis of Barty [Bar99]. Some applicable information is shown in Table 2.1. The Kirchoff algorithm code as describe above has been used as the basic algorithm used in the numerical simulation work in this thesis.

Kirchhoff propagation	
Input data:	Intensity $I(x, y)$ and phase $\phi(x, y)$ sampled on NxN grid with pixel size of Δx $f(x, y, 0) = \sqrt{I(x, y)}e^{i\phi(x, y)}$
Propagator:	$f(x, y, z) = \mathcal{F}^{-1} \exp\left(i2\pi z \sqrt{\frac{1}{\lambda^2} - \frac{i^2+j^2}{N^2\Delta x^2}}\right) \mathcal{F} f(x, y, z=0)$ i, j are the pixel numbers in the x and y direction respectively in the range $[-N/2, N/2]$
Output data:	Intensity: $I(x, y, z) = f(x, y, z) ^2$ Phase: $\phi(x, y, z) = \arg[f(x, y, z)]$ (Output data pixel size is the same as that of the input data)

Table 2.1: Basic method to develop the propagation algorithm. Source [Bar99].

2.2.2 Far field diffraction

In far field diffraction, the overall dimension of the object is very much smaller than the distances between the source to the sample and between the sample to the detector. In this case, the source and the detector are placed at a large distance from the sample. The wave curvature of the beam is therefore negligible. It gives the diffraction pattern that apart from size, is independent of the distance. Figure 2.7 shows the coordinate system for the description of far field diffraction. Let the coordinate of the object plane be (X, Y) and the coordinate of the projection plane (x, y) . The wave field at the detection

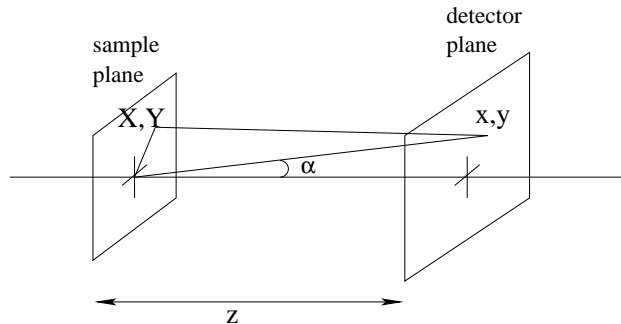


Figure 2.7: Configuration of far field diffraction.

plane can be written as [Cow95]:

$$f(x, y) = C \int \int S(X, Y) \exp\left(\frac{ik}{z}(xX + yY)\right) dX dY \quad (2.27)$$

where $S(X, Y)$ is the object transmission function, C is a constant, k is the wave number. Note that the plane waves incident upon the image plane are at an angle α to that plane, so that the angle α is related to the location of the object elements in the detector plane.

For $\frac{x}{z} \ll 1$ and $\frac{y}{z} \ll 1$ due to the large distance of the detector, the above equation can be approximated by the two dimensional Fourier transform as:

$$f(u, v) = C \int \int S(X, Y) \exp(ik(uX + vY)) dX dY \quad (2.28)$$

where $u = \frac{x}{z}$ and $v = \frac{y}{z}$ are the angular variables. This equation shows that the far field diffraction pattern at the image plane can be written as a suitably scaled Fourier transform of the object transmission function.

2.2.3 Fresnel number in phase imaging

Fresnel number is a dimensionless physical quantity in diffraction theory and is defined as [Gur03]:

$$F = \frac{a^2}{\lambda z} \quad (2.29)$$

where λ is the wavelength of a beam passing through an object with characteristic dimension a and hitting a detector at a propagation distance z .

In an imaging system, it is possible to distinguish three different regimes based on Fresnel number at a given wavelength as a function of propagation distance z [Gas99]:

- *The intermediate or Fresnel regime*, when the radius of the first Fresnel zone $r = \sqrt{\lambda z}$, can be compared to the characteristic dimension a of the sample perpendicular to the beam direction, such that $F \approx 1$. The image of the object is distorted here and varies rapidly with the propagation distance. In this regime the information of the phase can be accessed by combining the images recorded at different distances with a suitable algorithm [Clo99a].

- *The "edge detection" or near Fresnel regime* holds for small z values, such that $\frac{z}{\lambda} \gg F \gg 1$. Under these condition the object covers many Fresnel zones. The image has a close similarity with the object, and an immediate interpretation is possible. The image contrast depends linearly on the phase shift introduced by the object into the transmitted wave. A boundary contrast appears as a result of interference of strongly scattered rays at the boundary due to refraction with the reference rays. Therefore the phase gradient in the object becomes visible even for a purely transparent object [Clo97a; Arh04]. Most of the work done in this study is performed this region. Note that many authors incorrectly call this the near field region: The near field is well defined in optical theory as the region in which evanescent fields are significant, that is where $z \sim \lambda$.
- *The far field regime* holds for larger z values, such that $F \ll 1$. The image obtained is the far field diffraction pattern, with no resemblance to the sample. This corresponds precisely to the Fourier image of the object. In this region diffraction and phase dominate the imaging process [Nug03]. If we use the relation for spherical wave case as in Equation 2.12 for effective propagation distance, we define the Fraunhofer approximation, such that $\frac{a^2}{\lambda} (\frac{1}{z_1} + \frac{1}{z_2}) \ll 1$. In the limit of large sample to detector distance $z_1 \rightarrow \infty$, Fraunhofer approximation approach to the far field regime.

In this imaging system, a certain distance between the sample and the detector is required to optimize phase contrast for a certain object size as shown in the examples in Figure 2.4. In those figures the Fresnel number, $\frac{a^2}{\lambda z}$, corresponding to the propagation distances with the feature size of $a = 6\mu m$ (which is approximately the size of the bird's eye in the input phase of Figure 2.3) and using the x-ray wavelength of 1\AA , is equal to 360, 36, 3.6, 0.9 and 0.25 respectively. Therefore in this case, Figures 2.4(a), (b), and (c) are included in the near Fresnel regime. Figure 2.4(d) and (e) shows an example of intermediate regime.

2.2.4 Two beam diffraction

X rays are scattered by certain groups of parallel atomic planes within a crystal. When x-rays is allowed to impinge on a crystal, those of certain wavelengths will be oriented at a proper angle to a group of regularly arranged atomic planes so that they will combine in phase to produce diffraction pattern. In general, it is possible to work with two different geometries in two beam diffraction: the transmission (Laue) and reflection (Bragg) geometry, as shown in Figure 2.8. In this figure, k_o is the wave vector of the

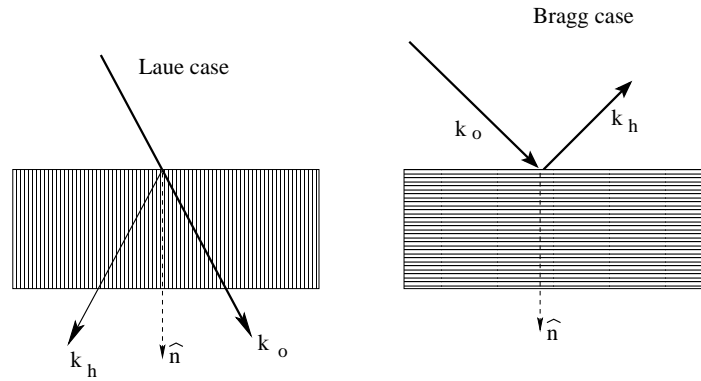


Figure 2.8: Geometric representation of x-ray diffraction in (a) transmission (Laue case) and (b) reflection (Bragg case).

incident wave, k_h is the wave vector of respectively transmitted (Laue) and reflected (Bragg) wave, \hat{n} is the normal to the crystal surface.

As the incident waves propagates down into a crystal its amplitude weakens, since a small fraction of the energy is reflected at each atomic plane. Furthermore the beam is reflected in the direction k_h , and/or can be re scattered into the direction of the incident beam, k_o . Each set of planes picks out and diffracts the particular wavelength from the radiation that satisfies the Bragg law [Cow95]:

$$2d_{hkl} \sin \theta_B = n\lambda \quad (2.30)$$

where d_{hkl} is the lattice plane spacing of the crystal, θ_B is the Bragg angle, λ is the wavelength and n is the order of reflection. In this way, a crystal can be used as a monochromator.

In the simple model just described, the Bragg diffraction occurs only at one precisely defined angle. In reality, the diffraction is not so well defined and the angular distribution over which diffraction occurs is described on the rocking curve. An example of a rocking curve of a perfect crystal is shown in Figure 2.9. In this case a perfect

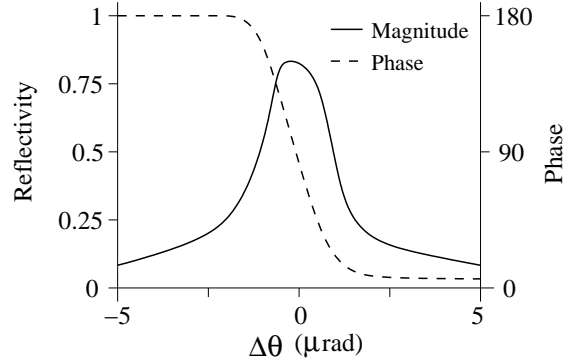


Figure 2.9: Schematic figure of rocking curve of a crystal.

crystal acts as a spatial filter. The amplitude filtering property is shown by rejecting waves with spatial frequencies outside the bandwidth frequency of the peak. There is also a 180° phase shift of the wave as it shows through the rocking curve [Dav95].

2.2.5 Partial coherence theory in phase imaging

A portion of the work undertaken in this research deals with the issue of partial coherence of the source. Accordingly, we introduce some of the relevant concept and tools here. There are two types of coherence [Bor99]:

- Longitudinal or temporal coherence.

A source is never strictly monochromatic. When the source emits over a finite wavelength bandwidth, $\Delta\lambda$, the wave has limited longitudinal coherence, which is also called temporal coherence. Each wavelength in the band would produce a different diffraction pattern. The superposition of these patterns could blur the diffraction fringes we wish to observe to the point that they are no longer visible.

We suppose two beams within a bandwidth frequency of $\Delta\nu$ and a path different $\Delta l = c\Delta t$ (c the speed of light in vacuum and Δt the time delay). The inter-

ference fringes will be formed if: $\Delta\nu\Delta t \leq 1$. Since $\Delta\nu \sim c\Delta\lambda/\bar{\lambda}^2$, the degree of coherence of a wave can be expressed by the coherence length, defined as [Man95]:

$$\Delta l \sim \frac{\lambda^2}{\Delta\lambda} \quad (2.31)$$

The longitudinal coherence can also be characterized by the relative bandwidth, $\Delta\lambda/\lambda$. Therefore, improving the beam monochromaticity enhances the temporal coherence.

- Transverse or spatial coherence.

A source is never truly a point source. An extended source size can be characterized by its lateral coherence, also known as spatial coherence. Typically for x-ray sources each portion of the extended source produces a wave that reaches the sample with a different phase and produces a different diffraction pattern. The superposition of such patterns could wash out the diffraction fringes that we wish to observe.

We assume an extended source with a size $\Delta\sigma$ is placed at a distance z_1 from the pinholes T_1 and T_2 that forms an angle $\Delta\theta$ from the source, as shown in Figure 2.10. Interference fringes will be observed if: $\Delta\theta\Delta\sigma \leq \bar{\lambda}$. Since $\Delta\theta \sim \Delta l_{\perp}/z_1$,

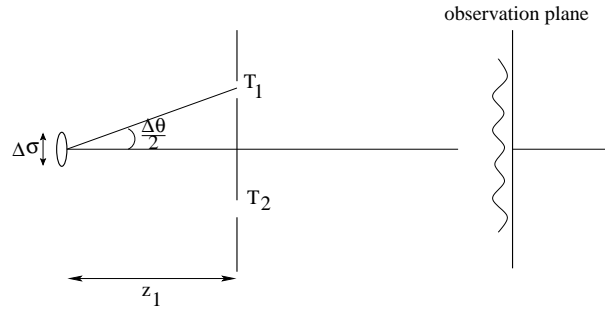


Figure 2.10: Illustration to describe spatial coherence property (Young's interference experiment).

the lateral coherence length can be expressed as [Man95]:

$$\Delta l_{\perp} = \lambda z_1 / \Delta\sigma \quad (2.32)$$

So, to enhance the spatial coherence, we must decrease the source size or increase the distance from the source to the sample.

However, now we consider a system that approaches the realistic experimental geometry of a micro focus x-ray laboratory source. Here we use the van Cittert-Zernike theorem [Bor99]. Figure 2.11 illustrates the propagation of a partially coherent radiation field originated from extended source and is observed by two points, P_1 and P_2 , located on the observation plane with the position vectors \mathbf{r}_1 and \mathbf{r}_2 perpendicular to the optic axis z . We assume that the extended source is in a plane parallel to the observation

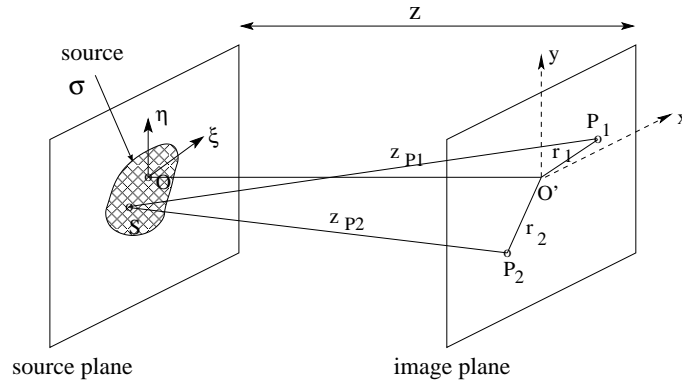


Figure 2.11: Irradiance of an extended source.

plane and can be divided into cells of statistically independent radiators. Thus, the total field at any point on the observation plane is given by summing the fields due to each of the cells as:

$$E(\mathbf{r}, t) = \sum_n E_n(\mathbf{r}, t) \quad (2.33)$$

A term known *mutual coherence function* is a basic for the theory of partial coherence. It represents the correlation function of the wave field between point P_1 and P_2 , which is described as [Bor99]:

$$\Gamma(\mathbf{r}_1, \mathbf{r}_2, \tau) = \langle E(\mathbf{r}_1, t) E^*(\mathbf{r}_2, t + \tau) \rangle \quad (2.34)$$

where τ is the time difference. The complex degree of coherence is defined as the normalized mutual coherence function as:

$$\gamma(\mathbf{r}_1, \mathbf{r}_2, \tau) = \frac{\Gamma(\mathbf{r}_1, \mathbf{r}_2, \tau)}{\sqrt{I(\mathbf{r}_1)} \sqrt{I(\mathbf{r}_2)}} \quad (2.35)$$

It represents the autocorrelation of the source disturbance. We point out that $\gamma(\mathbf{r}_1, \mathbf{r}_2, \tau) = 1$ indicates for fully coherent field and $0 \leq \gamma(\mathbf{r}_1, \mathbf{r}_2, \tau) \leq 1$ for partial coherence field. For a quasi monochromatic radiation, we may then approximate the correlation functions by the expression:

$$\Gamma(\mathbf{r}_1, \mathbf{r}_2, \tau) \cong J(\mathbf{r}_1, \mathbf{r}_2)e^{-i\omega\tau} \quad (2.36)$$

$$\gamma(\mathbf{r}_1, \mathbf{r}_2, \tau) \cong j(\mathbf{r}_1, \mathbf{r}_2)e^{-i\omega\tau} \quad (2.37)$$

When $\tau \approx 0$ ³, we define an equal time correlation functions as:

$$J(\mathbf{r}_1, \mathbf{r}_2) \equiv \Gamma(\mathbf{r}_1, \mathbf{r}_2, 0) \quad (2.38)$$

$$j(\mathbf{r}_1, \mathbf{r}_2) \equiv \gamma(\mathbf{r}_1, \mathbf{r}_2, 0) = \frac{J(\mathbf{r}_1, \mathbf{r}_2)}{\sqrt{I(\mathbf{r}_1)}\sqrt{I(\mathbf{r}_2)}} \quad (2.39)$$

The mutual optical intensity, $J(\mathbf{r}_1, \mathbf{r}_2)$, is then rewritten as [Man95]:

$$\begin{aligned} J(\mathbf{r}_1, \mathbf{r}_2) &\equiv \langle E(\mathbf{r}_1, t)E^*(\mathbf{r}_2, t) \rangle \\ &= \sum_n \langle E_n(\mathbf{r}_1, t)E_n^*(\mathbf{r}_2, t) \rangle \end{aligned} \quad (2.40)$$

The source with radiating surface σ consists of many point source elements with every elements of the source are mutually uncorrelated. Every single point produces coherent illumination so that each point emits a spherical wave. It leads to an expression for the mutual intensity as [Man95]:

$$J(\mathbf{r}_1, \mathbf{r}_2) = \left(\frac{\bar{k}}{2\pi}\right)^2 \int_{\sigma} I(\mathbf{r}') \frac{e^{i\bar{k}(z_{P1}-z_{P2})}}{z_{P1}z_{P2}} d^2\mathbf{r}' \quad (2.41)$$

where $I(\mathbf{r}')$ is a measure of intensity at \mathbf{r}' in the source.

Substituting this equation to the equal time complex degree of coherence of Equation 2.39, we have:

$$j(\mathbf{r}_1, \mathbf{r}_2) = \frac{1}{\sqrt{I(\mathbf{r}_1)}\sqrt{I(\mathbf{r}_2)}} \left(\frac{\bar{k}}{2\pi}\right)^2 \int_{\sigma} I(\mathbf{r}') \frac{e^{i\bar{k}(z_{P1}-z_{P2})}}{z_{P1}z_{P2}} d^2\mathbf{r}' \quad (2.42)$$

where

$$\begin{aligned} I(\mathbf{r}_1) &= J(\mathbf{r}_1, \mathbf{r}_1) = \left(\frac{\bar{k}}{2\pi}\right)^2 \int_{\sigma} \frac{I(\mathbf{r}')}{z_{P1}^2} d^2\mathbf{r}' \\ I(\mathbf{r}_2) &= J(\mathbf{r}_2, \mathbf{r}_2) = \left(\frac{\bar{k}}{2\pi}\right)^2 \int_{\sigma} \frac{I(\mathbf{r}')}{z_{P2}^2} d^2\mathbf{r}' \end{aligned} \quad (2.43)$$

³due to the assumption of small distance between points P_1 and P_2 in the observation plane, so that $z \approx z_{P1} \approx z_{P2}$

We refer Equation 2.42 as the van Citter-Zernike theorem which describes the correlation of the field at P_2 and P_1 . It says that the equal-time degree of coherence $j(\mathbf{r}_1, \mathbf{r}_2)$ is equal to the normalized complex amplitude of a certain diffraction pattern centered on a point P_2 at the corresponding point P_1 [Bor99].

For most problems of interest, we may take:

$$z_{Pn} = \sqrt{R^2 + (x_n - \xi)^2 + (y_n - \eta)^2} \approx R + \frac{(x_n - \xi)^2 + (y_n - \eta)^2}{2R} \quad (2.44)$$

where R is the distance OO' . We may approximate Equation 2.42 as [Bor99]:

$$j(\mathbf{r}_1, \mathbf{r}_2) = \frac{\int \int_{\sigma} I(\xi, \eta) \exp(i\bar{k} \frac{(x_1 - \xi)^2 - (x_2 - \xi)^2 + (y_1 - \eta)^2 - (y_2 - \eta)^2}{2R}) d\xi d\eta}{\int \int_{\sigma} I(\xi, \eta) d\xi d\eta} \quad (2.45)$$

We refer this equation as the far zone form of the van Cittert-Zernike theorem. In the far zone of the source, the equal-time degree of coherence $j(\mathbf{r}_1, \mathbf{r}_2)$ is expressible in terms of the Fourier transform of the intensity.

We now consider a mutual optical intensity $J(\mathbf{r} + \frac{\mathbf{x}}{2}, \mathbf{r} - \frac{\mathbf{x}}{2})$ described by Nugent [Nug91] incident on an aperture with complex amplitude transmission $A(\mathbf{r})$ at $z = 0$ with $\mathbf{r} = (\mathbf{r}_1 + \mathbf{r}_2)/2$ and $\mathbf{x} = \mathbf{r}_1 - \mathbf{r}_2$ as :

$$J(\mathbf{r}_1, \mathbf{r}_2) = \Psi(\mathbf{r}_1)\Psi^*(\mathbf{r}_2)g(\mathbf{r}_1 - \mathbf{r}_2) \quad (2.46)$$

where $\Psi(\mathbf{r})$ is the wave amplitude distribution, $g(\mathbf{r}_1 - \mathbf{r}_2)$ the coherence factor. The condition $g(\mathbf{r}_1 - \mathbf{r}_2) = 1$ will be the fully coherent limit. Under the Fresnel approximation, the intensity distribution in a plane a distance z from the aperture is written as [Nug91]:

$$I(\mathbf{r}, z) = \frac{1}{\lambda^2 z^2} \int g(\mathbf{x})K(\mathbf{x})e^{-i2\pi\mathbf{r}\cdot\mathbf{x}/\lambda z} d\mathbf{x} \quad (2.47)$$

where $K(\mathbf{x})$ is the autocorrelation of $\Psi(\mathbf{r})A(\mathbf{r}) \exp(i\pi r^2/\lambda z)$ ⁴, which is simply the coherent Fresnel diffraction pattern of the field Ψ . The above equation for intensity distribution can be written with the convolution theorem as:

$$I(\mathbf{r}, z) = g(\mathbf{x}/z) * K(\mathbf{x}, z) \quad (2.48)$$

⁴The autocorrelation function is given by:

$$K(\mathbf{r}) = \int T(\mathbf{r}')T^*(\mathbf{r}' - \mathbf{r})d\mathbf{r}'.$$

In that case we have $T(\mathbf{r}) = \Psi(\mathbf{r})A(\mathbf{r}) \exp(i\pi r^2/\lambda z)$.

where $*$ denotes convolution. The equation shows that the observed intensity distribution of a partial coherent diffraction pattern, $I(\mathbf{r}, z)$, is the convolution of the intensity of the fully coherent Fresnel diffraction pattern, $K(\mathbf{x}, z)$, with the shape of the scaled incoherent primary source, $g(\mathbf{x})$. In this case, the coherent diffraction pattern will be blurred by the convolution of the scaled source distribution.

This analytic description of partially coherent source allows us to explore the effect of varying the source size on the measured intensity and we will use it in later chapters.

2.3 Phase visualization for x-rays

As discussed, the propagation of x-rays through an object introduces shifts in the phase of the wave field. This phase shift can be visualized as a distorted wavefront which can be detected using various phase contrast techniques. Several modes of x-ray phase contrast imaging have been implemented over the years. Diffraction enhanced imaging and free space propagation phase contrast are discussed in the next subsection. Recently several groups have shown other phase contrast imaging techniques. Zernike phase contrast shows a linear dependence with the phase distribution [Zer42]. This been done by using annular phase plates in the back focal plane of an objective lens or a zone plate [Sch94]. Schlieren phase contrast has a similar setup to the Zernike phase contrast, with the only difference instead of phase plate at the back focal plane it uses a knife edge to block out half of the Fourier spectrum of the wave [Zak04].

Each different technique has its advantages and its drawbacks with respect to the accessible phase information, the complexity of the set-up, the requirements on the beam and resolution. Therefore, each technique has its own area of applicability.

2.3.1 Diffraction enhanced imaging

Diffraction-enhanced imaging is a differential method that relies on the phase difference across the wave front [Gao95]. The phase gradient can be resolved with a crystal analyzer that is placed between the sample and the detector, see Figure 2.12. The final result depends on which case of diffraction (Laue or Bragg) is used for the analyzer and

on the type of the beam (transmitted or reflected). The angular acceptance of the analyzer is described by its rocking curve. This is obtained by rocking the crystal through a specific reflection with no sample in the beam. The angular deviation introduced by a sample changes the incidence angle to the analyzer. To obtain a better contrast the

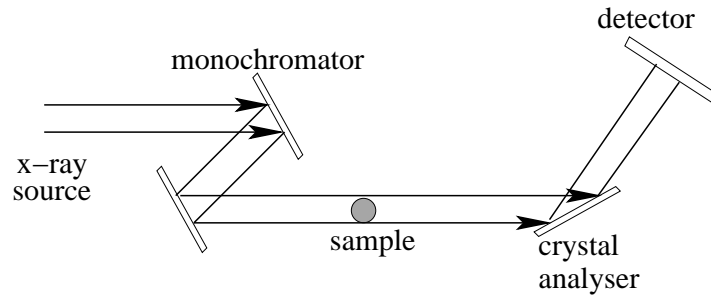


Figure 2.12: Diffraction enhanced x-ray imaging

working point of the reflection curve must be set to the point where the slope of rocking curve has maximum value. In this case, contrast is expected where phase gradients, $\nabla\phi$, are present. The resulting image will have enhancement contrast due to the scatter-rejection property of the analyzer, compared to an image when the angular setting of the analyzer was out of the Bragg position (absorption images). By changing the angle of the analyzer crystal around the Bragg position, different planar sections of the distorted wavefront can be imaged, leading to a series of images with differing contrast [Dav95]. The setup shown is simplified but in general the information that can be extracted is limited and rather qualitative. This is because the crystal analyzer does not reveal the local phase shift but instead reveals the local phase gradient. However, many groups show maps of the phase gradients [Ing95; Dav95; Gao95] and techniques do exist to produce reconstructed phase maps based on such measurement [Pag04b].

This technique is very useful in medical and biological studies particularly for detection of different kinds of biological tissues [Dav95], and a breast tissue sample from humans in phase mammography [Ing98]. In other work, Ingal and Baliaevskaya [Ing95] used the Laue case of diffraction in a crystal analyzer. This allows them to register simultaneously two kinds of detection: in the transmitted beam by using a CCD camera and in the reflected beam by using a scintillation counter. This allows the simultaneous

observation of the angular position in the rocking curve and the corresponding image contrast. One outstanding result of this method is an image of an aquarium fish [Ing95].

2.3.2 Free space propagation phase contrast

Free space propagation phase contrast imaging relies on Fresnel diffraction in free space of the wave field exiting the sample. It simply allows the wave field to propagate a sufficient distance away from the sample so that diffraction fringes can be observed. It is a unique contrast mechanism in comparison with other phase sensitive imaging techniques in that it has the advantage of a very simple experimental set-up requiring no optical element. The absence of optical elements implies that the method is intrinsically free from the usual aberrations. The free space propagation method allows refraction effects to be visualized and provides information about the distribution of the real part of complex refractive index in the sample.

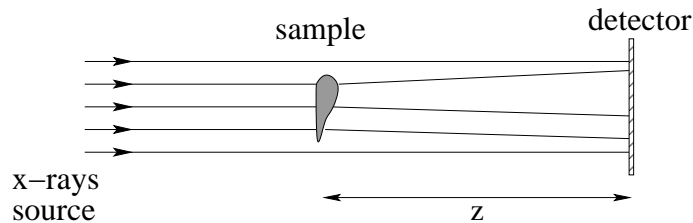


Figure 2.13: Free space propagation phase contrast imaging

In this technique, the x-rays emerging from the sample will propagate through space until they reach the detector, see Figure 2.13. The inhomogeneous phase shift produced by the sample refract the x-rays. After some propagation distance, the density of rays becomes inhomogeneous leading to observable changes in the intensity distribution.

This simple scheme of free space propagation phase contrast is routinely realized today on third generation synchrotron radiation sources. Snigirev [Sni95] first explored this technique for micro imaging of organic samples (fibers) using the ESRF source. However, this technique has also generated a considerable amount of interest in the development of more conventional laboratory-based x-ray tube sources which do not demand large distances in the experimental setup. Wilkins et al [Wil96; Gao98] de-

veloped this technique using a micro or nano focus laboratory x-ray source to get phase contrast images using spherical wave illumination of the object. McMahon et al [McM01] and Allman et al [All00] demonstrated in line phase visualization using neutron sources for crack detection in metal samples. Their propagated images of a metal sinker and a damaged aeroplane engine turbine blade show an increase in contrast. Toth and Kieffer [Tot05] showed phase contrast imaging of this technique using an ultrafast laser-based hard x-ray source. Projection x-ray radiography of this form was also discussed by Pogany [Pog97] using a contrast transfer function (CTF) formalism. The methods described there give insight into the nature of the image formation under the Fresnel approximation. Cloetens et al [Clo97a] used this technique to image a cracked silicon single crystal and metal matrix composite, both in projection and in computed tomography. Using electron microscopy methods, quantitative x-ray phase imaging has been developed [Baj00; May02], for high-brightness sources. The free space propagation technique has also been applied to a very broad range of areas [Clo96; All00; Gur01; Tot05]. It is this range of use that makes it an attractive basis for development in a study of x-ray diffraction phase contrast, as we will show in the rest of this thesis.

2.4 Phase measurement

Phase measurement is to determine quantitative information of the phase of an object. It can be done directly with interferometry and indirectly with phase retrieval algorithms.

2.4.1 X-ray interferometry

Interferometry is a quantitative phase measurement technique. This contrast is due to the interference of the beam transmitted through the sample with a reference beam often derived from the same source. The resulting interference fringes can be used to deduce the relative phases of the two waves. There are many different types of interferometry [Bor99], but all of them follow the same basic principle as shown in Figure 2.14. In this case any phase differences in the optical path for the beam transmitted through a sam-

ple are directly encoded using a monochromatic beam. The first optical element after the monochromator splits the incident beam into two. In a symmetrical experimental scheme the intensity of both beams are equal to each other. Beam splitting can be done

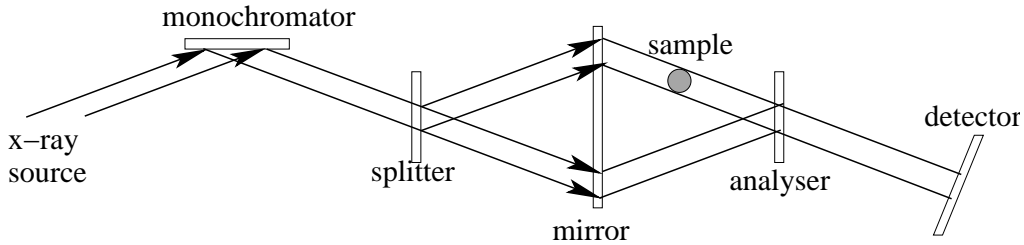


Figure 2.14: An x-ray interferometer phase imaging

in two ways: wavefront splitting and amplitude splitting [Hec97]. Young's double slits, Fresnel's bimirrors and prisms are example of x-ray wavefront splitters [Hec97]. Amplitude splitting is superior in some applications because in amplitude splitting case, high spatial coherence is not as essential as in the case of wavefront splitting [Mom03]. Crystals are used for amplitude splitting in the hard x-ray region and free standing multilayers or gratings are used for amplitude splitting in the soft x-ray region. The second element (often a mirror) in Figure 2.14 deviates the beam, so they can be recombined at the third element (such as a crystal analyzer). This is placed at the region of intersection of the two beams. A sample placed in the path of one of the beams between the mirror and analyzer, will introduce a phase shift and distort its wavefront inhomogeneously. The interference fringes are then recorded using a detector in the path of the outgoing beam.

The construction of x-ray interferometers is, in general, more complex than the construction of optical interferometers. X-ray wavelengths are three order of magnitude shorter than visible light and consequently an x-ray interferometer requires much tighter alignment and greater mechanical stability than for visible light interferometers. When the optical path difference fluctuates by more than a wavelength, the corresponding fringe pattern can be significantly changed. If the time required to record the fringes is longer than the time constant of fluctuations in the system, fringe contrast is lost [Mom03].

Intrinsically, the resolution of the system for x-rays is limited by the passage of the beam through optical elements. The beam energy of each point at its entrance of the crystal spreads out at its exit whose width will limit the resolution. The visibility of interference fringes is further limited by detector resolution.

X-ray interferometry was first demonstrated by Bonse and Hart [Bon65] and Ando et al [And72] first recorded x-ray phase images using a configuration as shown in Figure 2.14 for imaging of bone tissues and of a slice of granite. Momose et al [Bon00; Mom95; Mom03] developed this direct phase shift measurement technique into computed tomography. Each measurement allows one to obtain the map of the phase shift which is proportional to an integral over the path of x-ray beam on the decrement of the real part of the refractive index. So this map may be considered as a projection of the real part of the refractive index of the object along the path of x-ray beam. In computed tomography, one can obtain a set of such projections by rotating the object. Then the standard technique of computed tomography allows the reconstruction the distribution of the electron density, which is related to the real part of the refractive index inside the object.

There are several applications of x-ray interferometry including measurements of optical constants [Bon65], measurements of strains [Fod03] and lattice distortions in crystals [Abo00], and measurements of dispersion surfaces [Bon65]. The technique is generally limited by difficulties in ensuring the coherence of the x-rays, the coherent division of the x-ray beam, the stability of the optical path length and the limited availability of high quality optics. However, many of these applications are still pursued, and are now being applied at synchrotron radiation sources around the world [Mom95; Mom03].

2.4.2 Phase retrieval

There are several approaches that are currently used to solve the phase retrieval problem based on propagation induced contrast in the measured intensity. The method chosen often depends on the imaging regime in which the data has been acquired. In the near Fresnel region, Teague [Tea83] first derived a phase retrieval solution based on the so

called Transport of Intensity equation (TIE) with his Green's function solution. Further, a TIE based algorithm [Gur95; Nug96; Pag98] and single plane TIE based algorithm [Pag02] are used to retrieve the object phase in the small propagation limit.

A single plane contrast transfer function (CTF) based algorithm [Tur04a; Gur04; Clo99a; Zab05] can be used for larger propagation distances under condition of weakly absorbing object and slowly varying phase, as shown in Equation 2.69. A similar phase retrieval algorithm has been developed by Wu [Wu05] that can be used for x-ray energy range of 60-150 keV. This algorithm is also suitable for large propagation distances.

However, Gerchberg-Saxton [Ger72] type iterative methods are often used for more general cases including for far-field images. This algorithm is essentially an intelligent guess and check routine which searches through the space of possible solutions with the aim of converging on an acceptable solution. This method was modified by Fienup [Fie82] to create the hybrid input-output algorithm. Nugent [Nug03] also developed a phase retrieval type iterative algorithm for far field images, the so called astigmatic diffraction technique, which allows a solution without any detailed knowledge of the object shape. It allows the phase to be recovered uniquely and reliably from a measurement of the far field diffraction pattern combined with far-field diffraction patterns obtained with orthogonal cylindrically curved waves.

The choice for using phase retrieval algorithms depends upon the range of the propagation distances, the x-ray energy in the experiment and the properties of the sample. The non iterative algorithms [Nug96; Pag02; Tur04a; Wu05] are alternative approaches that find a deterministic solution, which has a direct mapping between the input data and retrieved phase. These solutions exist only under certain assumptions about the field to be measured. For example, if one is restricted to non rotational, weakly diverging fields with no intensity zeroes over some simply connected region of space, then it is possible to determine uniquely the phase using TIE methods. Time efficiency and resistance to noise perturbations tend to be the advantage of using a non iterative type solution.

Hereunder we discuss some of the phase retrieval algorithms in more detail, including: TIE based phase retrieval, single plane TIE based phase retrieval and the CTF based phase retrieval algorithms. We will not discuss far field methods as the work under-

taken here concentrates purely on the classical imaging regime of near and intermediate fields as described earlier.

TIE based phase retrieval algorithm

In this subsection, we derive the transport of intensity equation first and then discuss the TIE based phase retrieval algorithms. We will use the transport of intensity equation as a starting point for a phase retrieval technique and for the propagation equation in the model developed in Chapters 4 and 5. We consider that the beam propagates in the z direction and $\mathbf{r} = (x, y)$ is a two dimensional vector in the direction transverse to propagation direction. The transport of intensity equation can be obtained from the paraxial scalar wave equation [Tea83]:

$$\left(i \frac{\partial}{\partial z} + \frac{\nabla^2}{2k} + k\right) f_z(\mathbf{r}) = 0 \quad (2.49)$$

where $\nabla^2 = \left(\frac{\partial^2}{\partial x^2} + \frac{\partial^2}{\partial y^2}\right)$ and $k = 2\pi/\lambda$. Intensity is defined as:

$$I(\mathbf{r}) = f^*(\mathbf{r})f(\mathbf{r}) \quad (2.50)$$

The wave function $f_z(\mathbf{r})$ at a transverse plane at z , can be written explicitly in terms of its intensity I and the phase ϕ :

$$f_z(\mathbf{r}) = \sqrt{I_z(\mathbf{r})} \exp[i\phi_z(\mathbf{r})] \quad (2.51)$$

Expand the first term of Equation 2.49 and, neglecting the arguments for simplicity, after substitution of equation 2.51 we have [Pag99]:

$$i \frac{\partial f}{\partial z} = i e^{i\phi} \frac{\partial \sqrt{I}}{\partial z} - \sqrt{I} e^{i\phi} \frac{\partial \phi}{\partial z} \quad (2.52)$$

Expanding the second term of Equation 2.49 [Pag99]:

$$\frac{1}{2k} \nabla^2 f = \frac{1}{2k} e^{i\phi} \nabla^2 \sqrt{I} + i \frac{1}{k} e^{i\phi} \nabla \sqrt{I} \cdot \nabla \phi + i \frac{1}{2k} \sqrt{I} e^{i\phi} \nabla^2 \phi - \frac{1}{2k} \sqrt{I} e^{i\phi} (\nabla \phi)^2 \quad (2.53)$$

And the third term of Equation 2.49:

$$k f = k \sqrt{I} e^{i\phi} \quad (2.54)$$

Both the real and imaginary parts of the left hand side of Equation 2.49 must be equal to zero. If we add Equations 2.52, 2.53 and 2.54, and take the imaginary part of them, we obtain:

$$\frac{\partial I}{\partial z} + \frac{1}{k} \nabla \cdot (I \nabla \phi) = 0, \quad (2.55)$$

where we have used the identity $\nabla \cdot (I \nabla \phi) = \nabla I \cdot \nabla \phi + I \nabla^2 \phi$ and $\nabla \sqrt{I} = \frac{1}{2\sqrt{I}} \nabla I$. Equation 2.55 is known as the *transport of intensity equation*. It describes the relationship between the phase and intensity of a wave field over a plane to the rate of change of the measured intensities.

The real part of the summation of Equations 2.52, 2.53 and 2.54 leads to:

$$-2k\sqrt{I}\frac{\partial \phi}{\partial z} + \nabla^2 \sqrt{I} + \sqrt{I}(2k^2 - |\nabla \phi|^2) = 0 \quad (2.56)$$

This is known as the eikonal equation [Bor99]. The eikonal is the function that defines surfaces of constant phase in the wave field - that is the wavefronts.

In Equation 2.55, the intensity derivative along the propagation direction z is defined in terms of the intensity. The TIE describes how the intensity distribution of an electromagnetic field changes as it propagates through space. So, by measuring the intensity and analyzing how its distribution has changed with propagation, the phase of the field can in principle be deduced.

Methods for the solution of the TIE has in fact been developed, including an algorithm developed by Gureyev and Nugent [Gur95] and a later algorithm developed by Paganin and Nugent [Pag98]. The first algorithm inverts the TIE as a weighted sum over a series of orthogonal polynomials. A series expansion is applied to the intensity derivative and the phase. Then matrix inversion is used to recover the phase. This algorithm becomes computationally intensive in the presence of non uniform intensities, as will often be the case in practice. Therefore, it is impractical for general application to phase retrieval in the presence of object that have a non-uniform absorption distribution.

The second algorithm makes use of the rapid processing capability of the numerical Fast Fourier Transform [Pag99] to determine the phase where intensity variations in the field are present. This algorithm is discussed below since the results will be used throughout this thesis.

In order to solve equation 2.55, Paganin obtains the solution for the phase by using double Fourier transformation as [Pag99]⁵:

$$\phi = \phi_x + \phi_y, \begin{cases} \phi_x = \mathcal{F}^{-1} u_r^{-2} u_x \mathcal{F} I^{-1} \mathcal{F}^{-1} u_x u_r^{-2} \mathcal{F} (k \frac{\partial I}{\partial z}) \\ \phi_y = \mathcal{F}^{-1} u_r^{-2} u_y \mathcal{F} I^{-1} \mathcal{F}^{-1} u_y u_r^{-2} \mathcal{F} (k \frac{\partial I}{\partial z}) \end{cases} \quad (2.57)$$

where (ϕ_x, ϕ_y) are the solution for the components of the gradient operator in the equation for x and y direction respectively, \mathcal{F} denotes Fourier transformation, \mathcal{F}^{-1} denotes inverse Fourier transformation, (u_x, u_y) are the Fourier variables conjugate to (x, y) and $u_r^2 = u_x^2 + u_y^2$. It is understood that division by u_r^2 does not take place at the point where $u_r = 0$ in Fourier space ⁶. Alternatively, the division by u_r^2 can be regularized (e.g. Tikhonov ⁷) [Tik63]. This algorithm is efficient computationally and is able to take into account the intensity variations in the field.

Equation 2.57 is implemented by measuring two different intensities a small distance apart in order to measure the derivative. We require the distance to be small so that:

$$I(\mathbf{r}, z) \approx I(\mathbf{r}, 0) + z \frac{\partial I(\mathbf{r})}{\partial z} \quad (2.58)$$

Under this condition the intensity varies approximately linearly with propagating distance. The validity condition for the TIE solution is therefore when the higher order Taylor expansion terms is disregarded and Turner [Tur04b] simplify it as:

$$\lambda z u^2 \ll 1 \quad (2.59)$$

where u is the corresponding spatial frequency of the object. If the distance between measurement planes is too small, noise will be strongly amplified in the calculation of the z -derivative of intensity. With a too large distance apart it will give a poor estimate

⁵This algorithm is covered by an Australian Provisional Patent.

⁶Instead we multiply by zero at the point $k_r = 0$. This is equivalent to taking the Cauchy principal value of the integral operator ∇^{-2} [Pag99].

⁷Tikhonov's regularization is used to handle the division by zero by substituting:

$$\frac{1}{u_r} \rightarrow \frac{u_r}{u_r^2 + \alpha^2}$$

The regularization parameter α is inversely proportional to the signal-to-noise ratio. It means that without regularization α is 0. The regularization parameter can be increased for noisy data until the desired level of noise reduces.

of the derivative of intensity. The intensity data combined with the intensity derivative data allows us to retrieve the phase distribution independently.

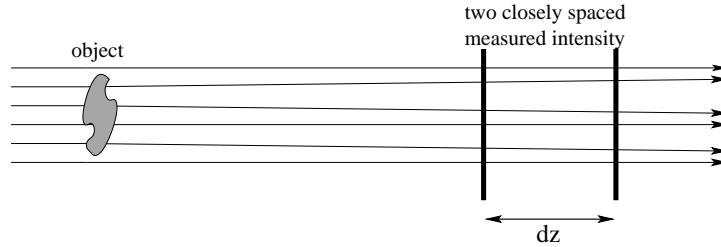


Figure 2.15: Configuration for applying TIE based phase retrieval algorithm. The measured intensities have a distance dz apart.

This algorithm is less restrictive than the single plane TIE based phase retrieval, discussed in the next subsection because the small propagation distance condition (Equation 2.59) is required between the two measurement planes, as shown in Figure 2.15, not to the distance between the sample and the two measurement planes. The performance of this algorithm has been successfully tested and shows excellent results. Using this technique, Nugent et al. [Nug96] have recovered the phase distribution of x-rays quantitatively. It was the first experimental demonstration of a non interferometric quantitative phase imaging technique using x-rays. The obtained phase shift on a model object carbon calibration grid that was in good agreement with an independent determination from the absorption. Later work of Paganin and Nugent [Pag98] extended this method to partially coherent light. A range of other radiation types were also be used to apply this algorithm, such as electrons [Pag01], neutrons [McM03c; All00] and visible light [Bar98].

Single plane TIE based phase retrieval algorithm

Paganin et al. [Pag02] have developed a single image non iterative phase retrieval algorithm applicable to near Fresnel images of homogeneous samples of known composition. This algorithm uses the TIE as its basis.

For a homogeneous sample the variation of phase and intensity in the object plane can be expressed in terms of the variations of projected thickness of the sample $T(\mathbf{r})$ in

the plane perpendicular to the propagation direction:

$$\begin{aligned} I(\mathbf{r}, 0) &= I_o e^{-\mu_o T(\mathbf{r})} = I_o e^{-2k\beta T(\mathbf{r})} \\ \phi(\mathbf{r}, 0) &= -k\delta T(\mathbf{r}) \end{aligned} \quad (2.60)$$

where $\mu_o = 2k\beta$ is the linear attenuation coefficient, β is the imaginary part of the refractive index, k is the wave number and I_o is the uniform intensity of the incident radiation. Projected thickness $T(\mathbf{r})$ is defined as the spatial distribution map of the object in the transverse direction.

For a near Fresnel image we can approximate $\partial I(\mathbf{r})/\partial z$ in the TIE by the finite difference between the object and image plane, using $I(\mathbf{r}, z) \approx I(\mathbf{r}, 0) + z \frac{\partial I(\mathbf{r})}{\partial z}$. By using this assumption and together with the expression for a single image intensity Paganin [Pag02] obtains the projection sample thickness as:

$$T(\mathbf{r}) = -\frac{1}{\mu_o} \ln \left[\mathcal{F}^{-1} \left(\frac{\mu_o}{z\delta\mathbf{u}^2 + \mu_o} \mathcal{F} \left[\frac{I(\mathbf{r}, z)}{I_o} \right] \right) \right] \quad (2.61)$$

where \mathbf{u} is the Fourier conjugate of \mathbf{r} . The intensity and phase of the object can then be obtained according Equation 2.60.



Figure 2.16: Configuration for applying single plane TIE based phase retrieval algorithm. The measured intensities have a distance dz from the object.

This single plane TIE based algorithm is restricted in that it is only valid in the near Fresnel region. Because the small propagation distance condition of Equation 2.59 has to be fulfilled for the distance between the sample and the measurement plane, as shown in Figure 2.16. However, the performance of this algorithm has been tested successfully [Pag02; May02; Gur04] in the near Fresnel region within its validity condition of small propagation distance. In [Tur04a], the validity condition for TIE was intentionally vi-

olated and it can be seen that the phase variations were inverted. As expected, the TIE retrieved thickness grossly underestimates the known correct values.

CTF based phase retrieval algorithm

Another treatment of x-ray image formation is given by Fresnel diffraction theory. In the case of a "weak" object, this expression can be formulated to give the so-called Contrast Transfer Function (CTF). Firstly, in this subsection we derive the CTF theory and then discuss the CTF based phase retrieval algorithms. We use, a monochromatic coherent plane wave source, transmitted through a sample described by the wave field at the exit surface of the sample as $S(\mathbf{r}) = S_0 \exp[i\phi(\mathbf{r}) - \frac{1}{2}\mu(\mathbf{r})]$, where $\phi(\mathbf{r})$ the phase shift and $\mu(\mathbf{r})$ the attenuation variation. In the small angle approximation, the wave function on planes $z > 0$ is given by the Fresnel diffraction integral, in Equation 2.4. The Fourier Transform of this wave function is then [Pog97]:

$$F_z(\mathbf{u}) = e^{ikz} \tilde{S}(\mathbf{u}) e^{-i\pi\lambda z u^2} \quad (2.62)$$

where $\tilde{S}(\mathbf{u})$ is the Fourier Transform of the wave field at the exit surface of the sample, $S(\mathbf{r})$. Then the Born type approximation of $\phi(\mathbf{r}) \ll 1$ and $\mu(\mathbf{r}) \ll 1$ is made so that:

$$S(\mathbf{r}) = S_0 [1 + i\phi(\mathbf{r}) - \frac{1}{2}\mu(\mathbf{r})] \quad (2.63)$$

and consequently:

$$\tilde{S}(\mathbf{u}) = S_0 [\delta(\mathbf{u}) + i\tilde{\phi}(\mathbf{u}) - \frac{1}{2}\tilde{\mu}(\mathbf{u})] \quad (2.64)$$

in which $\delta(\mathbf{u})$ denotes the Dirac delta function, $\tilde{\mu}(\mathbf{u})$ is the Fourier Transform of $\mu(\mathbf{r})$ and $\tilde{\phi}(\mathbf{u})$ is the Fourier Transform of $\phi(\mathbf{r})$. Substitute this into Equation 2.62, to get:

$$\begin{aligned} F_z(\mathbf{u}) &= S_0 \left[\delta(\mathbf{u}) + i\tilde{\phi}(\mathbf{u}) - \frac{1}{2}\tilde{\mu}(\mathbf{u}) \right] [\cos(\pi\lambda z \mathbf{u}^2) - i \sin(\pi\lambda z \mathbf{u}^2)] \\ &= S_0 \left[\delta(\mathbf{u}) - \frac{1}{2}\tilde{\mu}(\mathbf{u}) \cos(\pi\lambda z \mathbf{u}^2) + \tilde{\phi}(\mathbf{u}) \sin(\pi\lambda z \mathbf{u}^2) \right. \\ &\quad \left. + i\{-\delta(\mathbf{u}) + \tilde{\phi}(\mathbf{u}) \cos(\pi\lambda z \mathbf{u}^2) + \frac{1}{2}\tilde{\mu}(\mathbf{u}) \sin(\pi\lambda z \mathbf{u}^2)\} \right] \end{aligned} \quad (2.65)$$

The measured intensity at a distance z is proportional to the square modulus of the complex amplitude, $I_z(\mathbf{r}) = |f_z(\mathbf{r})|^2$. So, the Fourier Transform of the intensity [Pog97]

is:

$$\tilde{I}_z(\mathbf{u}) = I_0 \left[\delta(\mathbf{u}) - \underbrace{\tilde{\mu}(\mathbf{u}) \cos(\pi\lambda z \mathbf{u}^2)}_{\text{abs.term}} + \underbrace{2\tilde{\phi}(\mathbf{u}) \sin(\pi\lambda z \mathbf{u}^2)}_{\text{phaseterm}} \right] \quad (2.66)$$

This alternatively Born-type approximation for intensity will be referred further in this thesis as Contrast Transfer Function formalism. The term $\cos(\pi\lambda z u^2)$ and $\sin(\pi\lambda z u^2)$ can be conveniently plotted against the variable $\sqrt{\lambda z} u$, as shown in Figure 2.17.

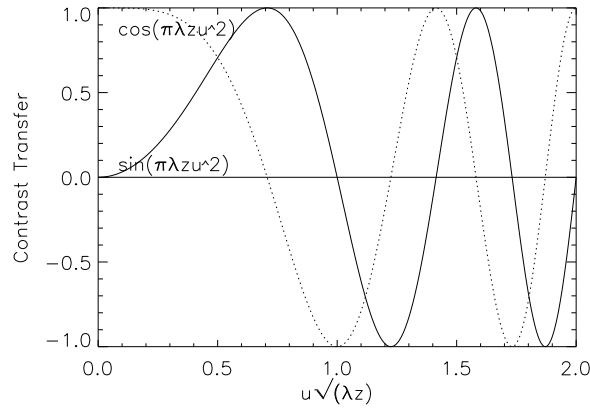


Figure 2.17: Absorption component, $\cos(\pi\lambda z u^2)$ and phase component, $\sin(\pi\lambda z u^2)$, of Contrast Transfer Function.

Various approximations have been identified which result in the same expression for the Fourier transform of the intensity, $\tilde{I}_z(\mathbf{u})$. These are the "weak object" or Born-type approximation that we have shown above:

$$\mu(\mathbf{r}) \ll 1, \quad \phi(\mathbf{r}) \ll 1 \quad (2.67)$$

the pure phase and slowly varying phase approximation of Guigay [Gui77]:

$$\mu(\mathbf{r}) = 0, \quad |\phi(\mathbf{r} + \lambda z \mathbf{u}/2) - \phi(\mathbf{r} - \lambda z \mathbf{u}/2)| \ll 1 \quad (2.68)$$

and the extension to weakly absorbing objects demonstrated by Turner [Tur04a]:

$$\mu(\mathbf{r}) \ll 1, \quad |\phi(\mathbf{r} + \lambda z \mathbf{u}/2) - \phi(\mathbf{r} - \lambda z \mathbf{u}/2)| \ll 1 \quad (2.69)$$

Many different approaches have been made for phase retrieval based on CTF method. Turner [Tur04b] developed the solution of Equation 2.66 for the projected thickness

$T(\mathbf{r})$ for homogeneous objects, as:

$$T(\mathbf{r}) = \mathcal{F}^{-1} \left[\frac{1}{-2k[\delta \sin(\pi\lambda z \mathbf{u}^2) + 2\beta \cos(\pi\lambda z \mathbf{u}^2)]} \mathcal{F} \left(\frac{I(\mathbf{r}, z)}{I_o} - 1 \right) \right] \quad (2.70)$$

Its relation with absorption $\mu(\mathbf{r})$ and phase $\phi(\mathbf{r})$ components are shown in Equation 2.60. In this algorithm, we need only a single diffracted intensity, $I(\mathbf{r}, z)$. Turner argued that this algorithm is fast and remains numerically stable. The validity condition of this solution is the weakly absorbing object and slowly varying phase condition as in Equation 2.69. This CTF expression represents an extension of the validity range of the propagation distance of the TIE algorithm. However, the validity condition for the CTF algorithm is more restrictive in terms of the object phase variation and maximum absorption.

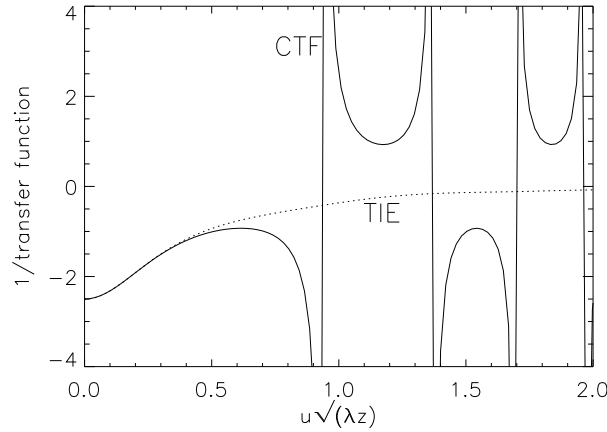


Figure 2.18: Inverse CTFs for weak absorption limit and slowly varying phase condition, is shown for TIE solution (dot line) and CTF solution (solid line). Source: [Tur04b].

Unfortunately, this CTF method shows some zeros for certain values of $u\sqrt{\lambda z}$. A conventional Tikhonov's regularization [Tik63] can be used to handle these singularities. The regularization stabilizes the retrieval at zeros, nevertheless the retrieval will be less accurate for spatial frequencies in narrow regions around the zeros. Conversely, the limited propagation requirement for the TIE method means that it should only be applied in the region before the first zero, as shown in Figure 2.18. The figure shows that the TIE solution has agreement with CTF solution for a small region of $u\sqrt{\lambda z}$ and it

begins to diverge at spatial frequencies just below the first contrast peak. Both solutions have low-frequency stability as a result, but at high frequencies TIE retrieval strongly suppresses information. In this case, Turner [Tur04b] argued that for TIE solution, the propagation distance, z , must be small enough that all structure of interest in the object has spatial frequencies, u , satisfying $\lambda z u^2 \ll 1$. The performance of this single plane CTF based algorithm has been tested successfully through experiment [Tur04a] within its validity condition.

Based on the CTF method, Zabler and Cloetens [Clo99a; Zab05] used through focal series of images to develop a 'holographic' reconstruction by combining phase retrieval procedure for a set of intensity images at different sample to detector distances. This method is valid for large propagation distances. The retrieved phase is obtained by performing a least square minimization of the difference between the measured intensity and the result of the intensity approximation which is calculated from Equation 2.66. Then, a minimum value is calculated. As a result, the retrieved phase for pure phase sample is calculated based on:

$$\tilde{\phi}(u) = \frac{\sum_m \tilde{I}_{z_m}^{(exp)} \sin(\pi \lambda z_m u^2)}{\sum_m 2 \sin^2(\pi \lambda z_m u^2)} \quad (2.71)$$

where the summation over $m = 1 \dots N$ needs to be applied when N images of measured intensities, $I_{z_m}^{(exp)}$, have been taken at N propagation distances $z = z_1 \dots z_N$. By including a weak absorption the retrieved phase and absorption becomes:

$$\begin{aligned} \tilde{\phi}(u) &= \frac{1}{2\Delta} \left(\mathcal{C} \cdot \sum_m \tilde{I}_{z_m}^{(exp)} \sin(\pi \lambda z_m u^2) - \mathcal{A} \cdot \sum_m \tilde{I}_{z_m}^{(exp)} \cos(\pi \lambda z_m u^2) \right) \\ \tilde{\mu}(u) &= \frac{1}{\Delta} \left(\mathcal{A} \cdot \sum_m \tilde{I}_{z_m}^{(exp)} \sin(\pi \lambda z_m u^2) - \mathcal{B} \cdot \sum_m \tilde{I}_{z_m}^{(exp)} \cos(\pi \lambda z_m u^2) \right) \end{aligned} \quad (2.72)$$

with following coefficients:

$$\begin{aligned} \mathcal{A} &= \sum_m \sin(\pi \lambda z_m u^2) \cos(\pi \lambda z_m u^2) \\ \mathcal{B} &= \sum_m \sin^2(\pi \lambda z_m u^2) \\ \mathcal{C} &= \sum_m \cos^2(\pi \lambda z_m u^2) \\ \Delta &= \mathcal{B}\mathcal{C} - \mathcal{A}^2 \end{aligned} \quad (2.73)$$

Note that this method also avoids the zero problem by filling them with information from the other planes. This process results in a quantitative phase map. They concluded that the quality of phase retrieval resulted from this algorithm seems sufficient by using four propagation distances [Zab05]. Through association with three dimensional reconstruction techniques (holotomography) Cloetens [Clo99a] then reconstructed the complete three dimensional mapping of the density in the sample. In field emission of transmission electron microscopy, the same idea of phase retrieval through focus variation has been used by Coene [Coe92] to retrieve phase of high- T_c superconductors and ferroelectric oxides.

A composite method for phase retrieval is developed by Gureyev [Gur03] which is also valid for large propagation distances. In this case, a TIE retrieved phase is used as the initial guess for a Gerchberg-Saxton-Fienup iteration. The method is applied for a pure phase object and it needs only a single image. This method indeed accelerates convergence of the iterative process.

In other work, Gureyev [Gur04] developed a combination TIE-CTF based method for phase retrieval for large propagation distances and this can be applied for a single image of small absorption objects. This method extends the validity range of the linearizations while preserving the deterministic nature and numerical efficiency of phase retrieval. In this method, the TIE is used to recover accurately the low-frequency components of the phase. Then, the predominantly high frequency components which are often small in magnitude are recovered iteratively by the CTF method. The performance of this combination TIE-CTF based algorithm has been tested successfully through simulation [Gur04].

Wu [Wu05] derived a different phase retrieval formula based on a single plane non iterative algorithm. For a sample away from its absorption edge, with an x-ray amplitude, $A(\mathbf{r})$, and phase, $\phi(\mathbf{r})$, can be written as a function of projected electron density, $\rho_{e,p}(\mathbf{r})$, as:

$$\begin{aligned} A(\mathbf{r}) &\approx \exp \left[-\frac{\sigma_{KN}}{2} \rho_{e,p}(\mathbf{r}) \right] \\ \phi(\mathbf{r}) &= -\lambda r_e \rho_{e,p}(\mathbf{r}) \end{aligned} \quad (2.74)$$

where r_e is the classic electron radius and σ_{KN} is the total cross section for x-ray photon

Compton scattering from a single free electron derived from the Klein-Nishina formula. For soft tissues this formula is valid in the photon energy ranging from about 60 keV to 150 keV. Starting from the Fresnel-Kirchhoff diffraction theory and the phase-space evolution of the Wigner distribution for x-ray wave fields, the projected electron density can be calculated using [Wu05]:

$$\rho_{e,p}(\mathbf{r}) = -\frac{1}{\sigma_{KN}} \log_e \left(\mathcal{F}^{-1} \left[\frac{\mathcal{F}[M^2 I(M\mathbf{r}; z_1 + z_2)]}{I_{in} [1 + 2\pi (\frac{\lambda^2 r_e z_2}{M\sigma_{KN}}) \mathbf{u}^2]} \right] \right) \quad (2.75)$$

where $I(M\mathbf{r}; z_1 + z_2)$ is the image intensity, I_{in} intensity at the entrance, M the magnification factor and \mathbf{u} the Fourier conjugate of \mathbf{r} . The validity condition of this solution is when $\lambda r_e / \sigma_{KN} \gg 1$. In practice, this condition is valid for photon energy range of 60 - 150 keV, away from its absorption edge.

Chapter 3

Experimental facilities

This chapter will describe the instrumentation employed to realize the phase contrast images used in this work. The experiments were mainly performed using a conventional x-ray laboratory source, as will be described in Section 3.1. Measurement of the x-ray spectrum, focusing the x-ray beam and measuring the source size will all be discussed in this section. These results will become the basis for the developments described in Chapters 4 and 5. Section 3.2 describes the image detection instruments; here mainly represented by the CCD camera. Resolution and contrast, which control the image quality, will be discussed in Section 3.3. Finally, the APS synchrotron facility will be described briefly in Section 3.4 since experimental tomography data in Chapter 6 was obtained using this source.

3.1 X-ray source

It is critical that the characteristics of the source used in x-ray imaging work are well known. The experimental work in this thesis was performed using a conventional polychromatic micro focus x-ray tube source (Fein Focus model FXE-160.50 fitted with x-ray tube FXT-160.20) containing a Cu or W target [fei93a]. In this section, we describe the salient characteristics of our source and the effects they have on imaging.

The geometry and setup of the micro focus x-ray tube is shown in Figure 3.1. Accelerated electrons are produced across an applied voltage (in the range of kilo Volts)

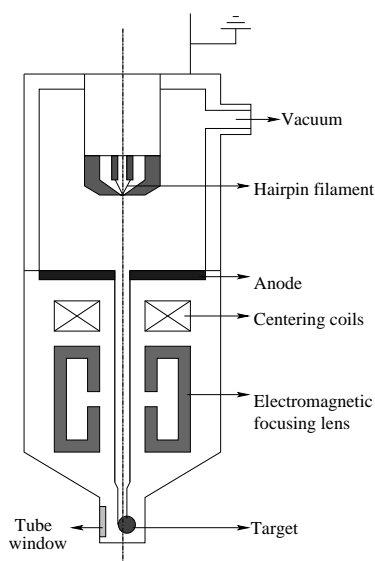


Figure 3.1: A micro focus tube that applied voltage accelerates electron beam onto a target, which in turn, emits the x-rays. Source:[fei93b].

between the cathode (e.g. filament) and the anode (in a Fein Focus tube the anode is located in front of the target [fei93a]; in other tubes the anode may be the target). Then, the electrons bombard a metal target. In each collision, the electrons slow down and some of the kinetic energy translates into radiation. Around 1% of the energy appears as x-rays, the remainder is mostly heat. For this reason, durable materials with high heat conductivity (such as tungsten, copper or molybdenum) are chosen for target materials.

3.1.1 X-ray spectrum

In the conventional x-ray laboratory source, the interaction of the accelerated electrons with the electrons in the metal target results in a continuous energy spectrum (Bremsstrahlung) with some narrow peaks corresponding to the characteristic x-ray energies of the elements of the metal target.

A higher tube voltage generates higher energy x-ray radiation with a greater penetrating power. A lower voltage generates a lower energy radiation which is better absorbed by the sample. On the other hand, increasing the tube current improves the signal to noise ratio by increasing the number of x-rays produced. This determines the exposure time needed for taking an image.

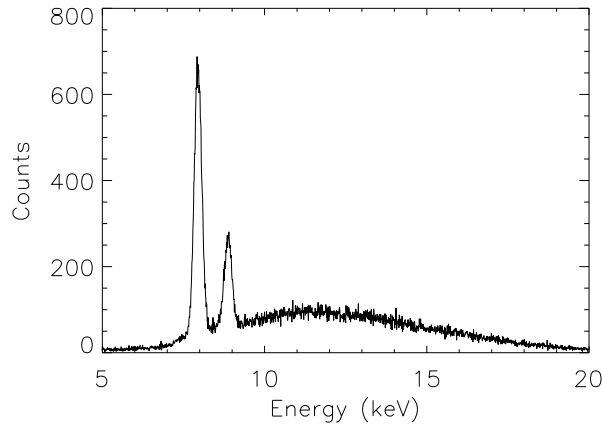


Figure 3.2: Combined detector response function and spectrum of the beam for a copper target at 20 kV tube voltage.

The histogram of the acquired events that corresponds to the combination of the detected x-ray spectrum and the detector response function acquired using the detector described in Section 3.2, is shown in Figure 3.2 for a copper target at 20kV and Figure 3.3 for a tungsten target at 60kV. The detector response function alone is shown in Figure 3.13. The acquired histogram is calibrated using known characteristic lines of an x-ray source, in this case using ^{241}Am . The spectrum in Figure 3.2 is dominated by

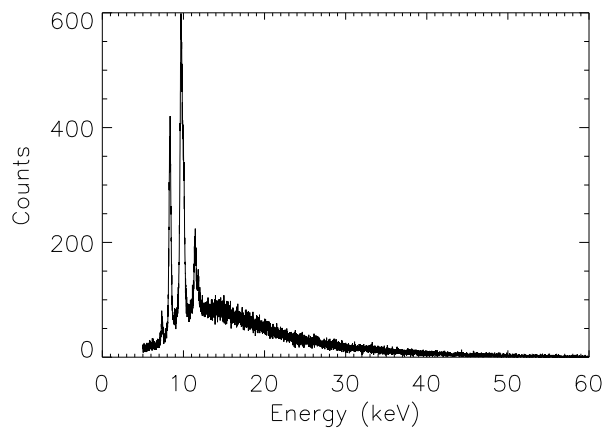


Figure 3.3: Combined detector response function and spectrum of the beam for a tungsten target at 60 kV tube voltage.

the characteristic lines of copper with energies of 8.0 keV ($K\alpha_1$ and $K\alpha_2$) and 8.9 keV ($K\beta_1$). There is also a significant amount of bremsstrahlung, and a cut off energy of 20 keV. The detector resolution is around 0.2 keV, as shown in Section 3.2, so we can not resolve the $K\alpha_1$ and $K\alpha_2$ lines which have a difference in energy of around 0.02 keV. Similarly, for tungsten, the spectrum in Figure 3.3 is dominated by the characteristic lines of tungsten with energies of 8.35 keV ($L\alpha_1$ and $L\alpha_2$), 9.8 keV ($L\beta_1$ and $L\beta_2$) and 11.3 keV ($L\gamma_1$) with a significant amount of bremsstrahlung. There is an apparent cut off energy of 30 keV in this case, because the detector response has very low efficiency for energies above 30 keV, as will be seen in Section 3.2.4.

3.1.2 Focusing the x-ray source

Early x-ray tubes used solid targets to emit x-rays while micro focus tubes used transmission targets [fei93a]. A transmission target usually consists of a thin high density layer (for example $5\mu\text{m}$ of tungsten) which sits on a lower density backing material (for example a thick sheet of aluminium or beryllium), as shown in Figure 3.4. Although the tube can focus the electron gun to an almost zero diameter, once inside the target, the electrons scatter, producing a volume of electrons that determines the general diameter of the focal spot for x-ray emission. Due to the fact that the electron spot is focused at the few microns thick high density layer on the target, the electron volume spread is limited and so limits the size of the x-ray source. High energy x-rays are produced from collisions in the high density material. The electrons that pass into the softer backing material generate mainly low energy x-rays that fail to escape.

Micro focus tubes rely on a electromagnetic objective lens to focus the electron beam on to the target, as shown in Figure 3.1, while the alignment of the beam uses electromagnetic centering coils which allow the adjustment of the direction components of the electron beam with respect to the axis of the tube. We optimize the source size in our instrument by iteratively adjusting the electron beam focus and the centering until the smallest features possible may be observed in a test mask. This procedure is performed whenever a filament is replaced and periodically under normal operating conditions.

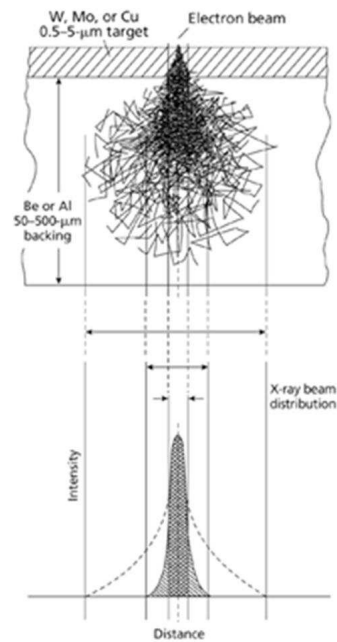


Figure 3.4: A laminated transmission target controls the size for the focal spot of x-ray emission. Source <http://www.reed-electronics.com/tmworld/index.asp?layout=article&articleid=CA218790&ri...>

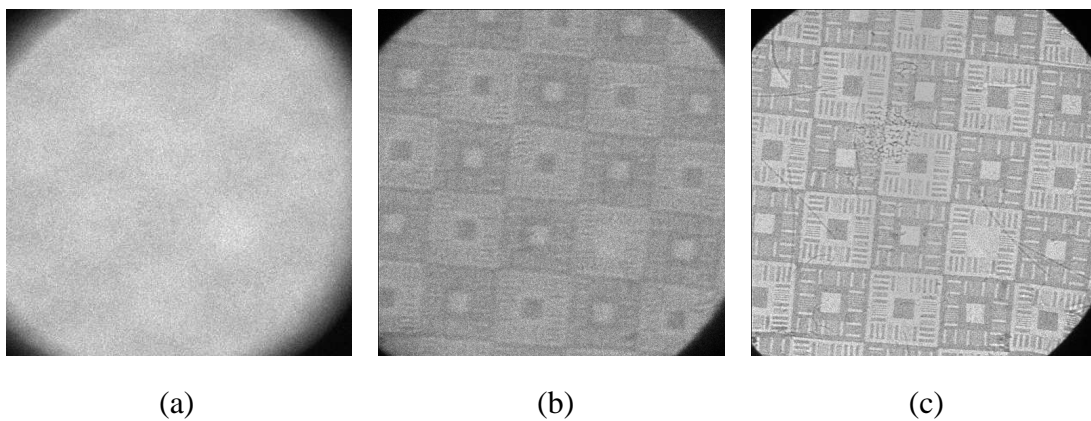


Figure 3.5: Image of a gold lithographic mask under different focusing conditions (a) unfocused, (b) improved focus and (c) optimal centering and focusing as judged by the sharpness of the image.

Focusing and centering of the beam influences the quality of the image sharpness. This is similar in effect to focusing in optical microscopy or in an ordinary camera; better focusing leads to a sharper image, as shown in Figure 3.5¹. In Figure 3.5(c) with the best focusing and centering, damage on the mask lamination and object sizes of around $20\mu m$ and larger are clearly visible. For poorer focusing and centering as in Figure 3.5(a) and (b) the ability to resolve fine features is lost.

3.1.3 Finite source size

X-rays are produced from individual electron collisions within the volume of the electron interaction region. The source thus consists of very many incoherent point sources which we model as transversely distributed according to the Gaussian Law. Accordingly, the x-rays from the source can be modeled as individual spherical waves emitted by each point of the source and which are statistically independent. The intensity contribution from different points of the finite source is assumed to have a weighting factor of $\sigma(\mathbf{r})$. In the small angle approximation each point of the source produces the same

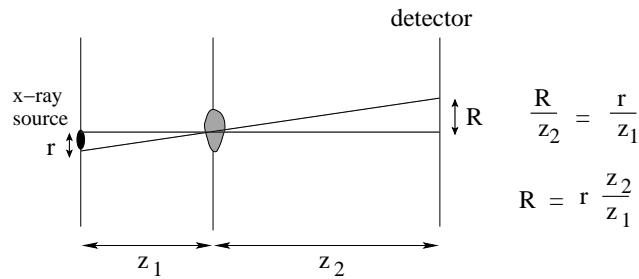


Figure 3.6: Different points from the source produces shifted on the image.

image of an object which becomes shifted by a definite distance, as shown in Figure 3.6. Points from the source at a given distance r produces a shift R on the image with $R = r(z_2/z_1) = r(M - 1)$, where M is the geometric magnification, as shown in Figure 3.7. An object with a size of h is imaged to a size of $H = Mh$ because of the magnification with $M = (z_1 + z_2)/z_1$. The resulting image intensity is then given by the convolution of the image with the geometric distribution of the source which is given

¹I would like to acknowledge Andrew Stevenson (CSIRO) for lending me the gold lithographic mask.

by the weighting of the source intensity $\sigma(\mathbf{r})$ [Nug91]. So in a projection image of the source we expect blurring due to diffraction and geometric blurring due to the source distribution. The later will have a size that is characteristic of the size of the source distribution σ_s .

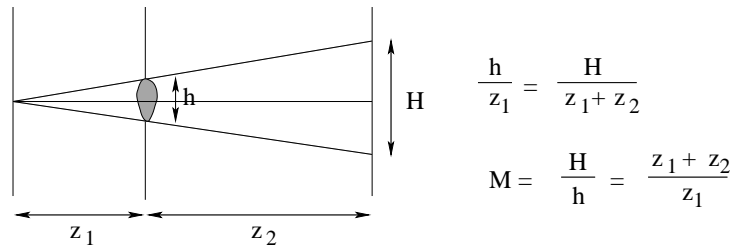


Figure 3.7: Geometric magnification, M

It is obvious that an object with size around the characteristic width of the source distribution, σ_s , or less, will disappear or become much less visible. On the other hand, an object with size much bigger than σ_s will be practically undisturbed by the source size. Therefore, in the free space propagation method, the achievable resolution depends largely on the size of the source [Pog97]. For small enough propagation distances the resolution that can be achieved in principle, is much smaller than the source size. However, in the typical imaging experiment it is firstly difficult to place the detector sufficiently close to the object and secondly this loses the benefit of magnification.

Given the importance of source size, it is important to be able to measure it for a given source. We describe this measurement in the remainder of this sub-section. Here are some methods presented by Madsen [Mad89] which have been applied to measure micro focus focal spot sizes:

- Using wire-type images as quality indicators. The actual focal spot size is found after taking radiographs using a range of wire diameters both below and above the expected focal spot size.
- Using the shadow of a straight edge or a round wire. The focal spot size is measured in the direction normal to the wire using the width of the penumbra after taking into account scaling due to image magnification. It is normally applied in two orientations (horizontal and vertical) for a two dimensional measurement.

- Using the shadow of a metal ball. This method can recover penumbra from any side of the ball. It means that all orientations of the focal spot are explored in one image.
- Using a special micro lithographic test mask and evaluating the radiograph.

Another method is to use a Fourier method by deconvolving the image with that which would have been produced by a coherent source [Maj96]. Using a known size pinhole is also a method for finding the source size of the system [Rob75], but it allows very little radiation to pass. So for the case of an x-ray laboratory source this is sometimes not practical as it needs long exposure times. Notwithstanding the number of methods available, it is quite difficult to measure focal spot size accurately [Mad89].

As previously described, the beam produced by a laboratory micro focus x-ray instrument has a variety of energies up to the energy of the incoming electrons. Therefore the effective distribution of the focal spot also depends on the energy of the electrons, determined by the tube voltage. The focal spot is smaller for low tube voltage than high tube voltage. This is simply because low tube voltage produces a smaller collision region in the target [fei93b].

Round edges like wires and balls have advantages in alignment with the x-ray beam direction but the partial transmission from the thinnest parts will increase the apparent focal spot size. Conversely, a straight edge has to be aligned very carefully to the direction of the x-ray beam but it can produce a more accurate size measurement. To eliminate these problems, the source size of our instrument has been measured using a shadow of a thin sharp edge. The experimental setup as shown in Figure 3.8 was used to measure the source size of our instrument. The figure shows that the edge produces a black to white transition in intensity i.e. a diffuse edge due to a presence of a penumbra. The relation between the blurring size and the source size is follows:

$$\sigma_i = \frac{z_2}{z_1} \sigma_s = (M - 1) \sigma_s \quad (3.1)$$

where σ_s is the characteristic size of the source and σ_i is the characteristic size of the image blurring. In a noise free environment, the source blurring will be negligible when $z_2 \rightarrow 0$ or when the detector is placed directly behind the sample. The same effect will

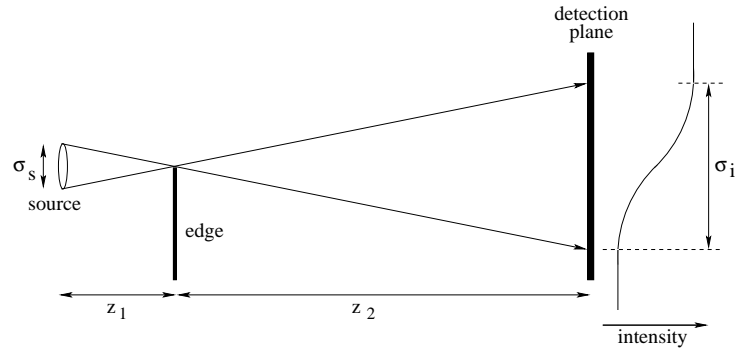


Figure 3.8: Focal spot size of an x-ray source determines the blurring in the image.

happen when $z_1 \rightarrow \infty$. A greater distance between the source and the sample will reduce the blurring effect.

The experimental setup for our source size measurement was $z_1 = 0.1m$, $z_2 = 1.7m$ and $M = 18$. The tube voltage was 20 kV and current $400 \mu A$. The imaging detector is a direct detection CCD camera (liquid nitrogen cooled Photometrics CH260), with 512×512 pixels and $27 \mu m$ pixel size. Figure 3.9 shows an image of a sharp thin edge of a $50 \mu m$ thick gold sample used to measure the vertical and horizontal source size directly. Note that the dark region represents the gold metal and the bright area represents the hole. The intensity image was corrected for the dark current and for non uniform illumination in the imaging system, according to Equation 3.3. In the plot, the image is averaged in the direction orthogonal to the edge to increase the photon statistics. Note that the intensity in the detector area corresponding to the gold metal is significantly decreased by absorption. The left and right penumbra should be identical for an ideal source, but it is slightly different in this measurement due to asymmetry in the source distribution. A zoomed in view of the right side of the edge is shown in Figure 3.10. The source FWHM consists of around 13 pixels, which corresponds to $19 \pm 5 \mu m$. We note that there is no need to include other blurring effects due to the detector in our case, as will be shown in Section 3.2. Similarly, it can be shown that diffraction broadening is also negligible. The first Fresnel zone has a radius of about $3 \mu m$ which is well below the detector resolution of $27 \mu m$. In order for diffraction broadening to be observed in our geometry the propagation distance would have to be

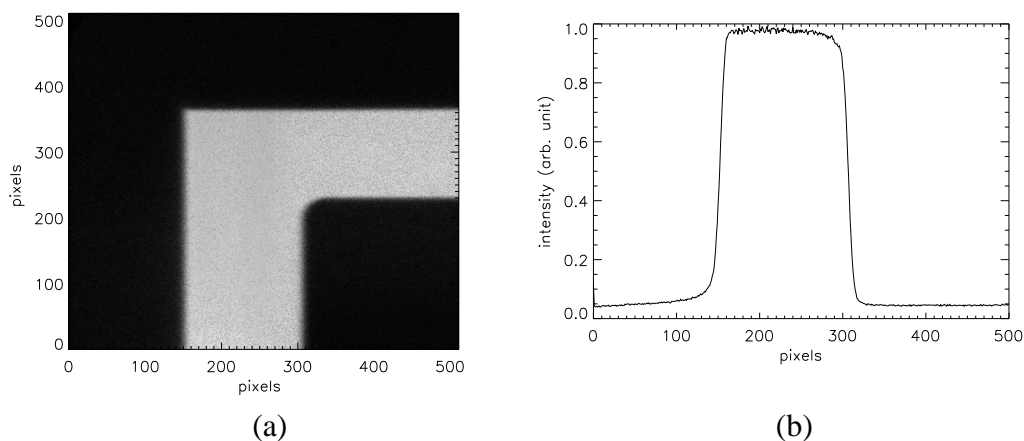


Figure 3.9: (a) Image of a sharp thin edge with (b) the corresponding plot for a vertically orientated edge.

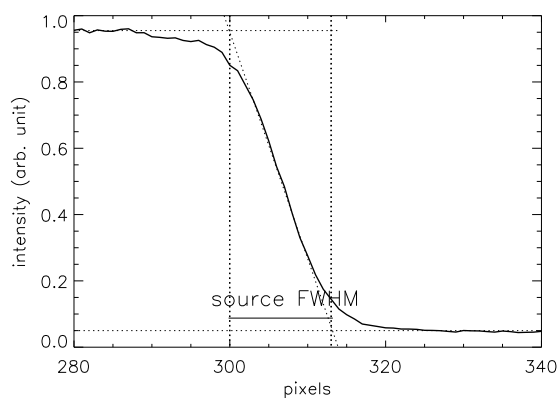


Figure 3.10: Zoomed in region of the right side from Figure 3.9(b).

more than $7m$.

The other side of the edge was also measured as a part of the uncertainty calculation from the measurement. The same procedure was also done for the horizontally orientated edge. This time we found the source FWHM to be $14 \pm 5\mu m$. Source size measurements must be done regularly for our source as the operating condition change, particularly after changing a filament.

3.2 X-ray detectors

The selection of the detector will also determine the quality of the image. Our experiments were mainly performed using a direct detection CCD camera (Photometrics CH260, liquid nitrogen cooled to $-105^{\circ}C$, with 512 x 512 pixels and $27\mu m$ pixel size). One image in our experiments was taken with a photographic film. The film used was Agfa Scopix IC3B film. The spectral measurements of the source were performed using a Si-PIN Photodiode x-ray detector (XR-100CR) [Amp98] with 196 eV resolution, which has a similar response function to the imaging detector.

The advantages of photographic film are that it usually has a larger field of view than is possible with a CCD chip, its ease of positioning, good spatial resolution of $< 10\mu m$ and relatively low material costs. The disadvantages are its non-linearity and the chemical processing required to obtain results. These make film inappropriate for advanced imaging such as tomography.

The most obvious advantage of the CCD camera is the convenience of detection: the image can be displayed and recorded digitally within a matter of seconds. These detectors have finite resolution, defined by the pixel dimensions. Interesting properties of the CCD camera are linearity of photometric response, signal to noise ratio (S/N ratio), sensitivity, dark current and spatial frequency response. We present a limited discussion of the CCD camera characteristics hereunder.

3.2.1 Linearity and uniformity

Linearity of detector response with the incident intensity is a useful prerequisite for quantitative imaging. An x-ray photon that is absorbed in the depletion layer of a CCD chip, generates a charge signal that, to a very good approximation, has a linear relationship to the photon energy, E , [Fie72]:

$$signal = \frac{E(eV)}{3.65eV} electrons \quad (3.2)$$

where the assumption is that the generation of one signal electron in silicon requires 3.65 eV of incident x-ray photon energy. This number varies slightly depending on the characteristics of the silicon used, for example Lumb [Lum90] obtains a value of 3.68

eV. The charge which has accumulated in each pixel is converted into a number. This number is in arbitrary 'units' and is called analogue data units (ADUs) which is not yet calibrated into physical units. The gain used is thus a constant of proportionality which converts ADUs into the amount of charge stored in each pixel.

Correction for non-linearities and non uniformity are made by means of a dark current and flat field correction. Correction was performed by:

$$I_{corr} = \frac{I_{sample} - I_{dark}}{I_{flatfield} - I_{dark}} \quad (3.3)$$

Dark current images is a background intensity, acquired without x-ray beam illumination. Flat field images is acquired with illumination. Both images were recorded without a sample to perform corrections on a pixel by pixel division on the projection image. This correction also minimizes systematic errors such as thermal noise (dark

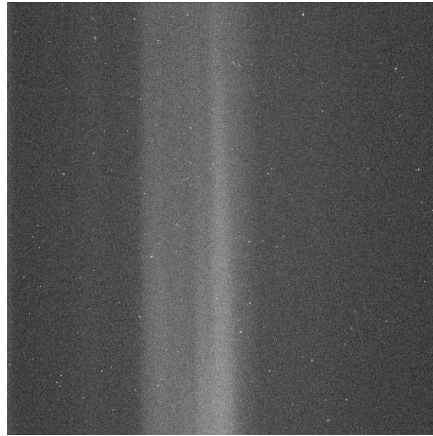


Figure 3.11: Dark current image, averaged from 20 images of 120 seconds each.

current), surface imperfections in the detector window, and the influence of beam imperfections. To get as close as possible to the "true" signal, the systematic errors should be characterized, measured and removed from the signal.

In our detector, there is some damage in some pixels which will influence the dark current image for a long exposure measurement. Figure 3.11 shows a dark current image which is an average of 20 images of 120 seconds for each image. A cooled Photometrics CH260 at $-105^{\circ}C$ produces dark current of $9 \text{ counts } s^{-1} \text{ pixel}^{-1}$. The damage in the pixels gives counts of 0.3% of dark current level signal. This indicates that physical damage of the chip is negligible when the detector is used at $-105^{\circ}C$.

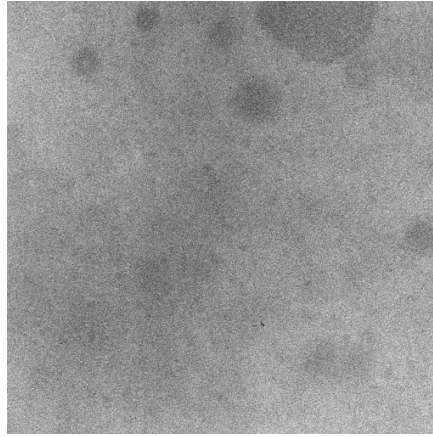


Figure 3.12: Flat field image, averaged from 20 images of 120 seconds each.

Other noise, such as the impurity on the surface of the beryllium exit window for the x-ray source will be corrected from the flat field image. Figure 3.12 shows the imperfection in the beam uniformity because of the beryllium window. This imperfection is around 3% of mean intensity.

3.2.2 Dark current

Electrons are not only produced by photons, but also by thermal energy. The electrons produced by this mechanism are termed 'dark current'. The electron charge accumulated in a CCD pixel due to dark current increases linearly with time. Cooling the camera reduces this unwanted electron source by minimizing the thermal energy. The dark current is incorporated into the corrected signal as shown in Equation 3.3.

3.2.3 Signal to noise ratio

The effect of noise sources on the CCD performance is described by the signal to noise ratio. The three primary sources of noise in a CCD camera are:

- Photon noise, also known as photonic or photon shot noise, is a fundamental property of the quantum nature of light. This noise is equal to the square root of the number of photons detected (according Poisson statistics). When the flux is high enough, photon noise is the dominant source of noise.

- Preamplifier noise, also called readout noise, is generated by the on-chip output amplifier by the camera electronics. Under low flux levels, readout noise is the dominant source of noise. The readout noise typically has an value of a few tens of electrons.
- Dark current noise, or thermally generated charge, can be measured and subtracted from data. Dark current noise is a particular concern in low-flux applications and long integration time (long exposures).

From that, the S/N ratio for a CCD camera can be calculated from the following equation:

$$\frac{S}{N} = \frac{S_{obj}}{\sqrt{S_{obj} + (N_{dark}^2 + N_{readout}^2)}} \quad (3.4)$$

where S_{obj} is the signal from the object, N_{dark} dark current noise, $N_{readout}$ readout noise. The available signal level from the object determines the integration time required to arrive at an acceptable S/N ratio. Acceptable S/N ratios vary with each applications.

3.2.4 Quantum efficiency

The quantum efficiency is defined as the efficiency ratio of the detected energy to the energy incident on the surface of the CCD, as shown in Figure 3.13. It is a function of incident photon energy. The back illuminated device offers superior quantum efficiency across a broader energy range. In the back illuminated CCD, photons enter into the depletion region from the backside without first passing through electrode structure which lies on top of the pixel structure on the front side, as shown on Figure 3.14. These electrodes reduce the detection efficiency for low energy x-rays (and blue optical light). The discontinuities in Figure 3.13 are the result of intrinsic properties of silicon, namely the absorption edge (L-edge at 0.1 keV and K-edge at 1.8 keV). As the x-ray photon energy increases up towards 10 keV, the transmission of photons through the depletion region creates less signal resulting in a decrease in quantum efficiency. A thicker depletion region (deep depletion device) overcomes this problem towards 20 keV. The improvement of the back illuminated device and the deep depletion device is

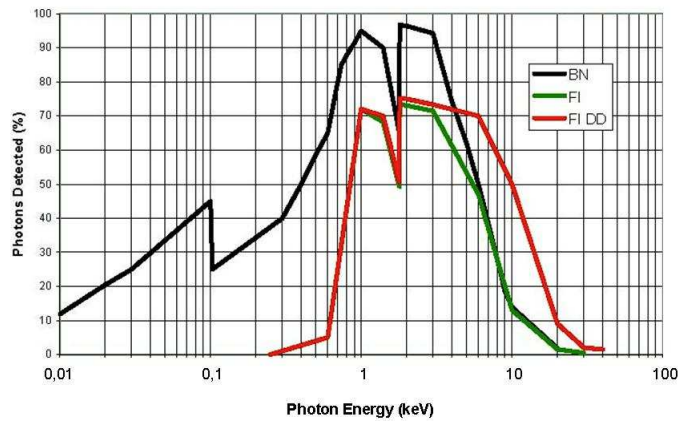


Figure 3.13: QE curves for Back illuminated (BN), Front illuminated (FI) and Front illuminated deep depletion (FI DD) Devices. Source http://www.lot-oriel.com/site/site_down/cc_workshopxray_deen.pdf.

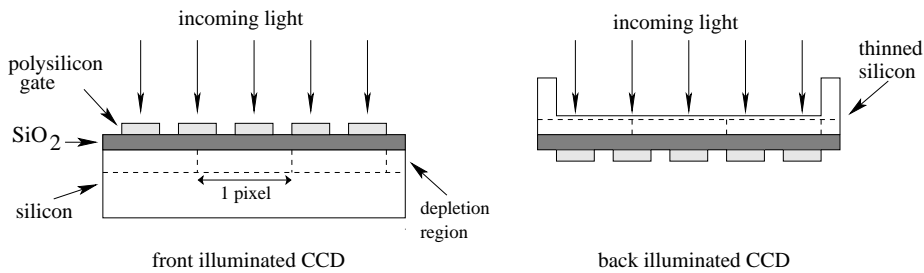


Figure 3.14: Structures of front illuminated and back illuminated devices.

confirmed by the experimental results of Lumb [Lum90]. However, a direct detection camera still is not optimal for the hard x-ray region above 20 keV.

3.2.5 Spread function

We will show now that our CCD camera has negligible detector spread function for our experiments. We hypothesize that this is because it is a direct detector camera operating at x-ray energies that are sufficiently low that pixel splitting events extend at most to neighbouring pixels. By contrast, in an indirect detector, a material is used to convert the x-ray photons to visible wavelengths which are subsequently detected by the CCD in the usual manner. These converter materials, or scintillators, will introduce blurring

effect in the detected signal [Ric98] which is dependent on energy.

To prove that our CCD camera has negligible detector spread function, we place an edge directly at the CCD detector where there is no blurring effect from the finite source size. This could not be achieved in reality because there is a vacuum chamber between the CCD chip and the beryllium window on the camera head. So we placed

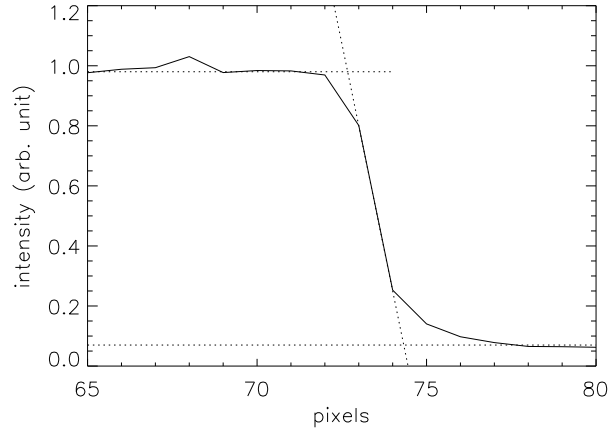


Figure 3.15: Plot of an edge placed directly to the camera head.

the sample as close as possible to the beryllium window, that is around 24 cm in front the CCD chip. The source is placed at 1.8 m from the CCD chip. A zoomed region of the plot of the edge is shown in Figure 3.15. The plot shows that the change from full shadow to full illumination occurs inside 1.5 pixels. This is compatible with the effective CCD blurring being one pixel or less. Accordingly, we neglect CCD blurring in our calculations. In this case, this will have the effect that the values we calculate for source sizes are an upper limit.

3.2.6 Dynamic range

The dynamic range of a detector is the ratio of the largest detectable signal to the smallest. In the x-ray region, the dynamic range is dependent upon the energy, $E(eV)$, of the incident photons. On a 16-bit device, as in our detector, the dynamic range is calculated according the formula:

$$DR = 2^{16} \cdot \left(\frac{g \cdot 3.65}{E} \right) \quad (3.5)$$

where g is the gain of the system in photoelectrons per count. Typical x-ray photographic films have a dynamic range of ≤ 100 for photon energies around 1 keV, while our CCD detector has 1680 (assuming a gain of 7 photoelectrons per count). Note that in this 16-bit device: the corresponding maximum ADU values are $2^{16} = 65536$.

3.3 Resolution and contrast

Resolution and contrast are two factors for quantifying image quality. They are related terms. Resolution is defined as the minimum distance between two points at which a certain contrast is achieved. The closer two objects that can be resolved by the system, the greater the resolution of the system. Contrast is also sometimes called visibility. It is defined for fringes as the ratio of the difference in the maximum and minimum intensity (signal) divided by their sum, as first formulated by Michelson [Bor99], and is measured using:

$$V_{image} = \frac{I_{max} - I_{min}}{I_{max} + I_{min}} \quad (3.6)$$

where I_{max} and I_{min} are the maximum and minimum intensities.

In the free space propagation technique, which is free from optical system aberrations, the resolution and contrast of the image are determined by the properties of the source size and the quality of the detection system (pixel size, p). In the case of spherical wave illumination, the geometric magnification factor (M), will help to achieve a better resolution as:

$$resolution \geq \frac{2p}{M} \quad (3.7)$$

The factor 2 is used because of the Nyquist sampling theorem which is equivalent to requiring that the closest distance for which two objects can be resolved is across 2 pixels.

In conclusion, the coherence of the illumination, finite source size, magnification and pixel size of the imaging detector will all influence both the resolution and the contrast of the system. In the following chapter, we quantify and model some of these effects.

3.4 Synchrotron facility

Synchrotron radiation is produced by a relativistic accelerated charged particle. It was used from the early seventies in a parasitic mode on particle accelerators for high energy physics (first generation) [Win95]. Afterwards, as dedicated light sources, second generation machines appeared. Then, a tremendous improvement in the stability and control of the trajectory of the charged particle beam, together with the appearance of multi pole insertion devices to produce synchrotron radiation in a more efficient way, become the fundamental characteristics of third generation synchrotron radiation sources.

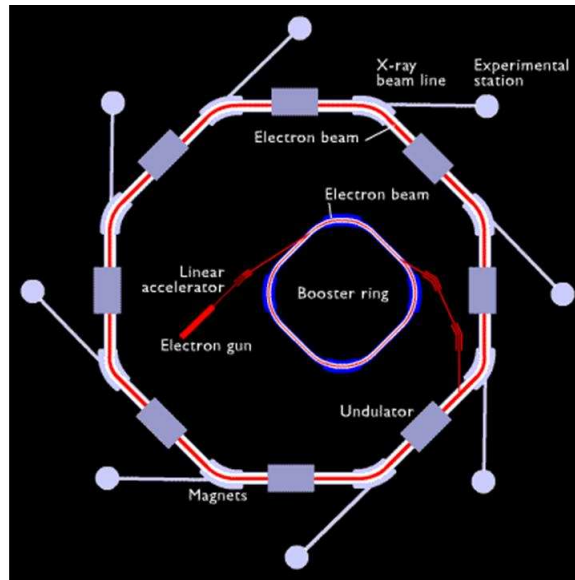


Figure 3.16: A synchrotron setup facility. Source <http://www-project.slac.stanford.edu/ssrltxrf/spear.htm>.

A schematic setup of a typical third generation synchrotron facility can be seen in Figure 3.16. The charged particles used at a synchrotron are usually electrons. An electron gun supplies energetic electrons to the linear accelerator. The electrons are accelerated to relativistic velocities and produce a radiation in a narrow cone as seen by a stationary observer. Multi pole insertion devices and bending magnets are placed in succession in a storage ring. The bending magnet causes electrons to follow a circular trajectory along its length [Win95]. The flux and brightness of the emitted x-ray beam can be improved significantly by the insertion devices (wigglers and undulators). This

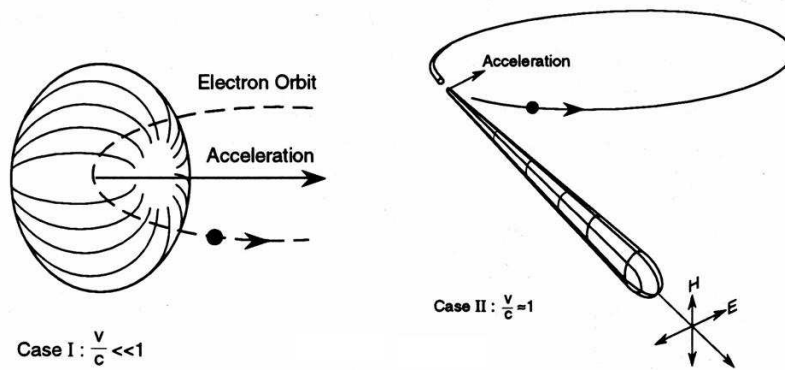


Figure 3.17: Emission patterns of radiation from electrons in circular motion. Case I: at a low velocity compared to the light velocity. Case II: approaching the light velocity (ie. a relativistic particle). Source [Win95].

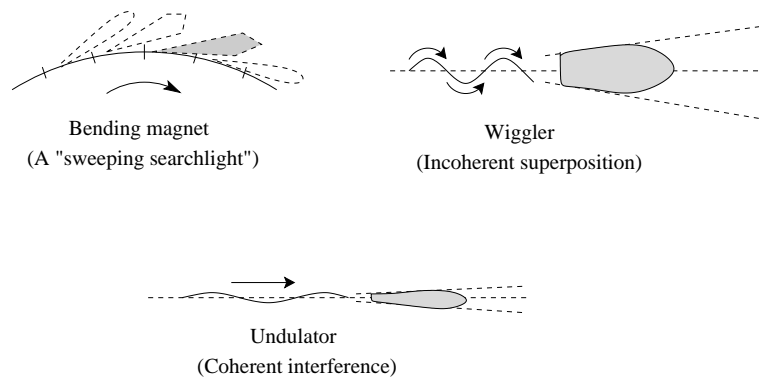


Figure 3.18: Radiation from bending-, wiggler- and undulator magnets. Source [Win95].

is achieved with a spatially periodic magnetic field from permanent magnets. When the charged particles oscillate radiation is emitted at each pole reversal and the combined effect increases the flux in a given spectral distribution.

From the storage ring, a highly directional and polarized beam of x-rays is emitted in the plane of the synchrotron, as shown in Case II of Figure 3.17. The emitted flux is in the direction perpendicular to the acceleration of the electrons. These x-rays cover a broad range of energies allowing for energy tuning using monochromators. These facilities led to the development of beam lines where x-rays are used for numerous experiments simultaneously in many experimental stations. The high flux and energy tunability allow us to achieve extremely short detection times in an experiment.

The main advantage of using an insertion device source (wiggler or undulator) instead of a bending magnet source is that more flux will be produced in a given bandpass for the same source size. Wigglers work by using an array of magnets with alternating field directions to force electrons into a sinusoidal trajectory through the straight sections of a synchrotron. Wigglers provide a broad spectrum and high photon flux (yet less bright than undulator) radiation. An undulator is similar to wiggler in that it uses an array of magnets. However, in an undulator the bending angle in each pole is

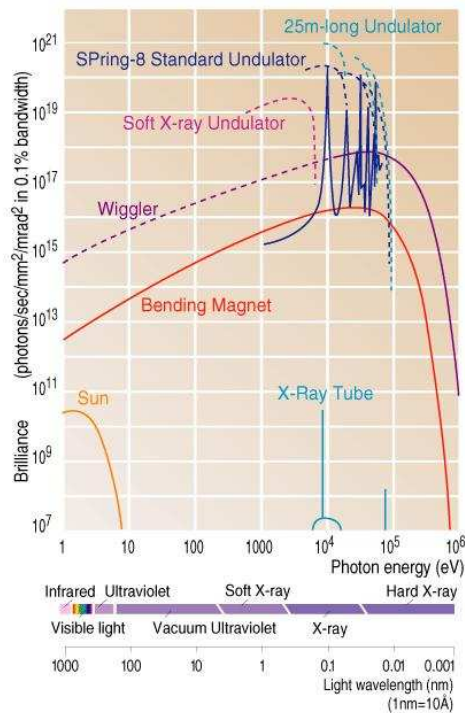


Figure 3.19: Spectral brightness for several radiation sources. Source http://www.spring8.or.jp/e/general_info/overview/sr.html.

much smaller, so it does not increase the small angular divergence of the radiation, as shown in Figure 3.18. In this case, the intrinsic brightness of synchrotron radiation is preserved. Furthermore, interference effects in the emission by the array of magnets that forms essentially collinear source points produces a discontinue spectrum that is enhanced at certain wavelength, as shown in Figure 3.19. This insertion device leads to a higher emitted intensity in a given energy bandpass when compared to bending mag-

nets. However, when monochromaticity is not a requirement then sufficiently broadening the bandpass of a bending magnet source can provide a similar net flux as for an insertion device and have similar source limitations on the resolution [Pee05]. A facility establishment at a bending magnet source is a useful tool for materials, biological and medical science and it can compete in terms of exposure times with insertion device lines using a broad bandpass where energy purity is not an issue.

Our tomography data was acquired at the 2-BM (bending magnet) beam line at the Advanced Photon Source (APS) at Argonne National Laboratory with the experiment setup as shown in Figure 3.20. A beam size of $4 \times 100\text{mm}^2$ (vertical \times horizontal) is delivered from the bending magnet source. The energy range is tunable between 5 and 20 keV with a bandwidth of $dE/E < 10^{-3}$ by the use of a Kohzu double crystal monochromator [Wan01]. The small lateral extent of the source (one-sigma source size of $102\mu\text{m}$ horizontally and $35.1\mu\text{m}$ vertically) and the long source sample distance of 50 m, results in a small incident divergence as seen from a point on the sample. The beam divergence is $2.04\mu\text{rad} \times 0.7\mu\text{rad}$ (horizontal \times vertical) and is therefore

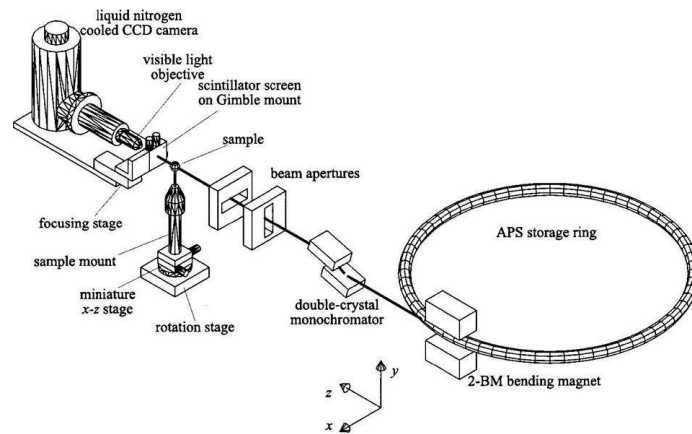


Figure 3.20: Tomography experiment setup at the 2-BM facility. Source [Wan01].

excellent for coherent imaging applications. The rotation for tomographic acquisition is performed by a precision rotation stage. The transmitted x-rays through the sample illuminate a $300\mu\text{m}$ thick CdWO_4 single crystal scintillator. The visible light emitted by

the scintillator is relayed to a CCD detector by a microscope objective. A 10x objective lens is used in our experiment. With the effectively grainless scintillator, the resolution of the system is primarily determined by the effective pixel size which is calculated based on the $4.65\mu m$ actual pixel size coupled by a 1x Tube lens and connecting tube into the CCD camera. The resulting effective CCD pixel size is $0.735\mu m$. The CCD camera has 2048 X 2048 pixels. The CCD detector is mounted on a translation stage aligned with the x-ray beam in order to vary the sample to detector distance.

Tomography experiments generate large amounts of data and demand a lot of computing power for data acquisition, image processing and reconstruction calculations. The 2-BM facility has constructed a pipelined data acquisition and reconstruction system that integrates a fast detector system, high speed data networks and a cluster of parallel computers [Wan01]. It allows us to obtain a data set and perform a complete tomographic reconstruction on the timescale of minutes. The data acquisition is controlled by a graphical user interface program running on a Sun workstation.

Each data set contains 720 projections, with 2048x2048 pixels for each projection. Several dark current and flat field images are also acquired along with the projection data. These images are essential for correction and normalizing the projection images. The flat field images were taken once every 101 projections to minimize the effects of any beam instability. Dark current images were collected at the end of each data set.

Chapter 4

Image modelling for transparent samples

An image formation model is developed analytically for the phase-contrast radiography technique using an extended and spatially incoherent source. Some parts of this chapter have been published [Arh04]. In Section 4.1 we begin by developing an image formation model suitable for transparent samples in the short wavelength region for which the transport of intensity equation is valid. We then use it to predict the sensitivity of the imaging process as a function of spatial frequency. It is tested numerically in Section 4.2. In Section 4.3, the imaging model is experimentally demonstrated using an x-ray radiography set-up, and a laboratory micro focus x-ray source. We find that the results are in excellent agreement. This model is then used to define an objective filtering criterion, in Section 4.4, that can be applied to improve the image quality from phase images obtained at different propagation distances.

4.1 Image formation model for a periodic object

In this section we investigate the transport of a radiation from a source of finite dimensions through an object with only one dimensional phase variation. The basic arrangement of the image formation model is shown in Figure 4.1.

We assume here that the sample influences only the phase of the beam that it is a

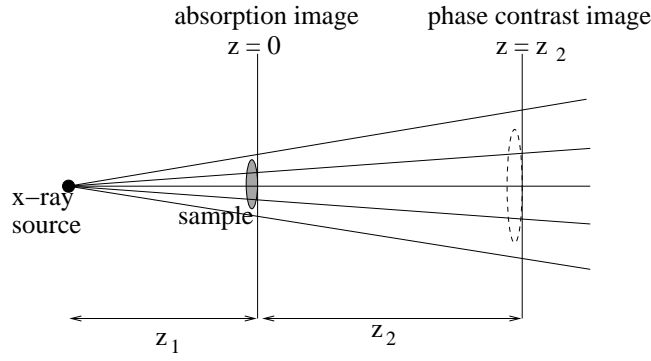


Figure 4.1: Free space propagation phase contrast imaging using x-ray source. z_1 is the source sample distance and z_2 is sample detector distance

transparent but refractive sample. We suppose that the source has a spatial distribution $\sigma(\mathbf{r})$, and is spatially incoherent. Accordingly, the sample is illuminated by spherical wave fronts, originating from points within the extended x-ray source. The sample is placed at a distance z_1 from the source. The wavefront is distorted by its passage through the sample. The transmitted wave function is observed at the measurement plane placed at a distance z_2 from the sample. The object plane and the measurement plane are assumed to be a planar surface orthogonal to the optic axis of the system. We denote the coherent intensity due to the illumination of a single point in the source at the measurement plane as $I_{coh}(\mathbf{r}, z_2)$. The measured intensity distribution can be treated as a simple convolution of the coherent image with the source intensity distribution after appropriate scaling. A simple transformation of the Fresnel diffraction integral allows us to write the resulting partially coherent image intensity as [Nug91]:

$$I(\mathbf{r}, z_2) = \frac{1}{M^2} \int I_{coh}\left(\frac{1}{M}\mathbf{r}', \frac{1}{M}z_2\right) \sigma\left(\frac{1}{M-1}[\mathbf{r} - \mathbf{r}']\right) d\mathbf{r}' \quad (4.1)$$

In order to be explicit, a Gaussian distribution is used as a model for the finite source in this work:

$$\sigma(\mathbf{r}) = \frac{1}{\sigma_s \sqrt{2\pi}} \exp\left(-\frac{\mathbf{r}^2}{2\sigma_s^2}\right) \quad (4.2)$$

Here, σ_s is the characteristic width of the source distribution, and its value is calculated according to:

$$\sigma_s = \frac{FWHM}{2\sqrt{2\ln 2}} \quad (4.3)$$

where FWHM is the full width at half maximum.

Consider an object with a one dimensional phase variation:

$$\phi(\mathbf{r}) = \phi_0 \cos(\mathbf{k}_s \cdot \mathbf{r}) \quad (4.4)$$

with a sample period of $2\pi/\mathbf{k}_s$. The phase shift $\phi(\mathbf{r})$, introduced by the sample, is proportional to the real part of the refractive index, δ , integrated along the propagation direction z .

$$\begin{aligned} \phi_0 \cos(\mathbf{k}_s \cdot \mathbf{r}) &= -\frac{2\pi}{\lambda} \delta \int \cos(\mathbf{k}_s \cdot \mathbf{r}) dz \\ &= -\frac{2\pi}{\lambda} \delta t \cos(\mathbf{k}_s \cdot \mathbf{r}) \end{aligned} \quad (4.5)$$

From Figure 4.2, we see that for a given periodic modulation, ϕ_0 depends on the am-

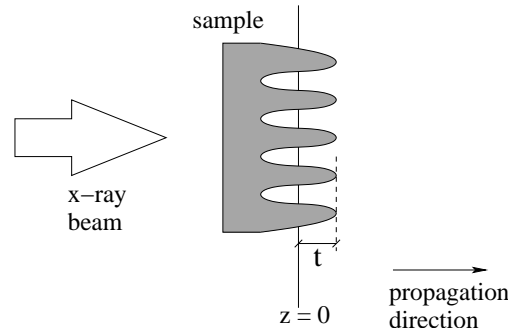


Figure 4.2: Sample with a one dimensional phase variation, t is the amplitude of the sinusoidal profile of the sample.

plitude, t , of the modulation on the sample. The transmitted wave function for uniform intensity plane wave illumination incident on the phase object is:

$$S(\mathbf{r}, 0) = S_0 \exp[i\phi(\mathbf{r})] \quad (4.6)$$

where S_0 is the amplitude of the incident wave, giving an intensity after the sample of $I_{coh}(\mathbf{r}, 0) = |S(\mathbf{r}, 0)|^2 = S_0^2$.

The transport of intensity equation, in Equation 2.55, can then be used to describe the propagation of the transmitted wave function :

$$\frac{\partial I_{coh}(\mathbf{r}, 0)}{\partial z} = -\frac{1}{k} \nabla \cdot (I_{coh}(\mathbf{r}, 0) \nabla \phi(\mathbf{r})) \quad (4.7)$$

where z is the effective propagation distance, as described in Equation 2.12.

Using Equation 4.4 and 4.6, the transport of intensity equation becomes:

$$\frac{\partial I_{coh}(\mathbf{r}, 0)}{\partial z} = -\frac{S_0^2}{k} |\phi_0| k_s^2 \cos(\mathbf{k}_s \cdot \mathbf{r}) \quad (4.8)$$

We then assume that there is a small propagation distance, such that:

$$I_{coh}(\mathbf{r}, z) \approx I_{coh}(\mathbf{r}, 0) + z \frac{\partial I_{coh}(\mathbf{r}, 0)}{\partial z} \quad (4.9)$$

Using Equation 4.8, this becomes:

$$I_{coh}(\mathbf{r}, z) = S_0^2 \left[1 - \frac{z |\phi_0| k_s^2}{k} \cos(\mathbf{k}_s \cdot \mathbf{r}) \right] \quad (4.10)$$

In our case, 'small' means that:

$$z |\phi_0| \frac{k_s^2}{k} \ll 1 \quad (4.11)$$

The partially coherent image intensity, from Equation 4.1, becomes:

$$I(\mathbf{r}, z_2) = \frac{1}{M^2} \int S_0^2 \left[1 - \frac{z_2 |\phi_0| k_s^2}{Mk} \cos(\mathbf{k}_s \cdot \frac{\mathbf{r}}{M}) \right] \sigma \left(\frac{1}{M-1} [\mathbf{r} - \mathbf{r}'] \right) d\mathbf{r}' \quad (4.12)$$

Taking into account the source distribution, as given by Equation 4.2, the measured image intensity is:

$$I(\mathbf{r}, z_2) = \frac{S_0^2}{M^2} \left[1 - \frac{z_2}{Mk} |\phi_0| k_s^2 \exp \left(-\left[\frac{M-1}{M} \right]^2 \frac{k_s^2 \sigma_s^2}{2} \right) \cos(\mathbf{k}_s \cdot \frac{\mathbf{r}}{M}) \right] \quad (4.13)$$

We introduce some dimensionless variables :

$$N_F = \frac{k \sigma_s^2}{z_1}, \quad (4.14)$$

which is the Fresnel number of the source at the sample (similar case as in Equation 2.29 which is for the Fresnel number of the sample and has a factor 2π smaller than the new defined Fresnel number), and:

$$\xi = \sigma_s \cdot k_s \quad (4.15)$$

which describes the extent of the source in units of the characteristic length scale of the sample. We can now rewrite Equation 4.13 as:

$$I(\mathbf{r}, z_2) = \frac{S_0^2}{M^2} \left[1 - \frac{M-1}{M} \frac{|\phi_0|}{N_F} \xi^2 \exp \left(-\frac{1}{2} \left[\frac{M-1}{M} \right]^2 \xi^2 \right) \cos(\mathbf{k}_s \cdot \frac{\mathbf{r}}{M}) \right] \quad (4.16)$$

We also use the dimensionless distance $X = \mathbf{r}/\sigma_s$, so the equation can be expressed in terms of ξ and M :

$$I(\xi, M) = \frac{S_0^2}{M^2} \left[1 - \frac{M-1}{M} \frac{|\phi_0|}{N_F} \xi^2 \exp\left(-\frac{1}{2} \left[\frac{M-1}{M}\right]^2 \xi^2\right) \cos\left(\xi \cdot \frac{X}{M}\right) \right] \quad (4.17)$$

It can be seen that the propagated intensity can be described as a constant term that is modulated at a frequency characteristic of the sample frequency. Accordingly, we can define a general visibility function which takes into account the finite source size and the propagation contrast mechanism for a transparent sample with a one dimensional harmonic phase variation, in the region of validity for the transport of intensity equation:

$$I(\xi, M) = \frac{S_0^2}{M^2} \left[1 - V_{trnsp}(\xi, M) \cos\left(\xi \cdot \frac{X}{M}\right) \right] \quad (4.18)$$

The general phase visibility function is then:

$$V_{trnsp}(\xi, M) = \frac{M-1}{M} \frac{|\phi_0|}{N_F} \xi^2 \exp\left[-\frac{1}{2} \left(\frac{M-1}{M}\right)^2 \xi^2\right] \quad (4.19)$$

The visibility is a measure of how well a given spatial frequency is preserved in the imaging process. Ideal visibility would then have a value of 1, according to the definition in Equation 3.6 while a visibility of zero would mean no visible contrast. The

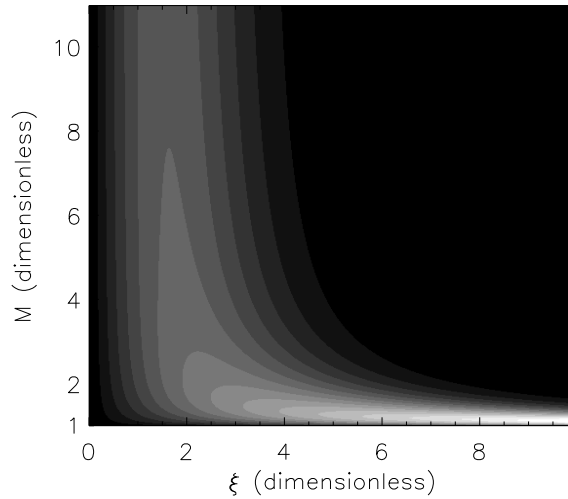


Figure 4.3: Phase visibility function as a function of spatial frequency, ξ , and magnification, M , for a transparent sample with $\phi_0 = 1$ and $N_F = 10$. Black colour represents 0 value and white colour represents the highest value of 0.56.

visibility function used here is analogous to the modulation transfer function often used

in image characterization. It is a useful guide to the quality of the image, as we will be the case in this thesis, but must be used cautiously if quantitative information is sought. Figure 4.3 shows the visibility function that describes the phase contrast in the image as a function of spatial frequency and magnification for a transparent sample with $\phi_0 = 1$ and $N_F = 10$. The visibility function will be maximum when $\frac{\partial V_{trns}}{\partial \xi} = 0$. This happens at:

$$\xi = \sqrt{2} \frac{M}{M-1} \quad (4.20)$$

It is clear that for $M \rightarrow \infty$, then $\xi \rightarrow \sqrt{2}$. This means that for high magnification the peak sensitivity of the visibility function will occur when $\xi \approx \sqrt{2}$. For large magnifications the maximum in the visibility function is also largely independent of the magnification. This is due to the exponential term of Equation 4.19, which describes the effect of source blurring and which acts to reduce the visibility of higher spatial frequencies. In such cases, the visibility will be limited by the source size. However, when magnification is only slightly bigger than unity, the peak sensitivity of the function moves to higher spatial frequencies. Significant visibility can then be observed for structures that are smaller than the source size. Of course in such cases finite detector resolution may well prevent such features from being observed. As an example of these phenomena, the experimental results of Cloetens et al [Clo96] show the visibility of high spatial frequencies decreasing with increasing propagation distance (or increasing magnification).

4.2 Numerical model

A confirmation of our developed model is given by a numerical simulation. The complex index of refraction will be used to express the distribution of intensity and phase of the sample. The algorithms that are used here for the numerical propagation of coherent, monochromatic optical waves through space have been developed by Barty [Bar99]. As shown in Section 2.2.1, the Kirchhoff formulation of scalar diffraction theory has been used for plane waves with some appropriate modification for spherical waves.

In this numerical simulation, we model sinusoidal samples with various spatial fre-

quencies. Figure 4.4 shows a sample with one spatial frequency, in this case corresponding to the period of $40\mu m$. The length of the sample is $250\mu m$. The sample thickness of $15\mu m$ will give the value $\phi_0 = 1$, for calculating the visibility in Equation 4.19. We used the refractive index data for Kapton ($C_{22}H_{10}N_2O_4$) at an x-ray energy of

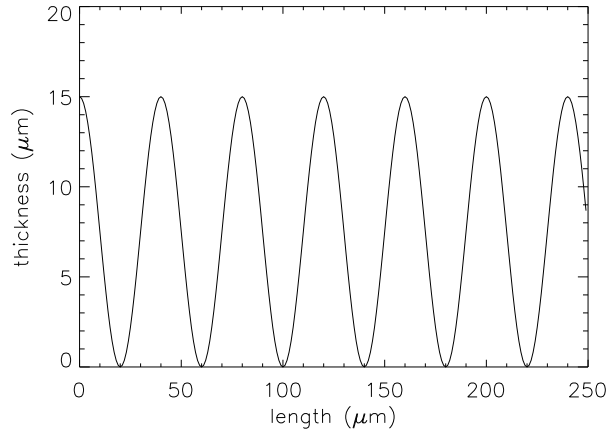


Figure 4.4: One dimensional model of the sample for numerical simulation

11 keV. At that energy Kapton has $\delta_\lambda = 2.558 \times 10^{-6}$ and $\beta_\lambda = 2.783 \times 10^{-9}$ [cxr95]. With these data we calculated intensity and phase directly after the sample (at $z = 0$) which becomes the input for the Fresnel diffraction algorithm. The propagated image with the parameters $z_1 = 0.1m$ and $z_2 = 1.7m$, (Magnification factor = 18), was then

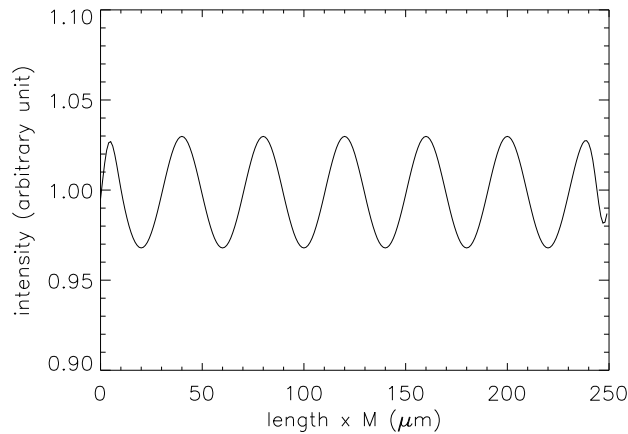


Figure 4.5: The measured intensity image at the detector plane, with $M=18x$

calculated by that algorithm. The intensity at the detector plane for a finite source can be calculated by the convolution of the propagated point source image with the magnified Gaussian source distribution with $\text{FWHM} = 10 \mu\text{m}$. The intensity at the detector plane can be seen in Figure 4.5. The parameters above were chosen to imitate some typical experimental conditions in our laboratory. The quality of the image can be described quantitatively using the measured visibility. This is defined as the ratio of the difference in the maximum and minimum intensity divided by their sum. The visibility at a particular frequency is given by Equation 3.6.

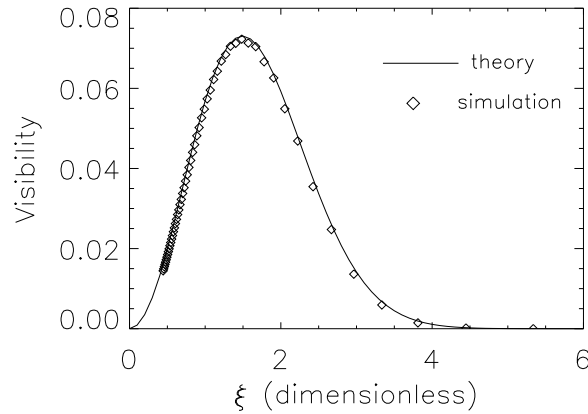


Figure 4.6: Theoretical curve of visibility plotted against the simulation results for $15\mu\text{m}$ thick polyimide film.

Figure 4.6 shows a simulation showing the image visibility as a function of spatial frequency compared with the theory (Equation 4.19). The numerical simulation results show excellent agreement with the theoretical line for the visibility function. If we rewrite the validity condition given by Equation 4.11 in terms of the Fresnel number, N_F , and spatial frequency, ξ , we get:

$$\xi^2 \ll \frac{N_F}{\phi_0} \frac{M}{M-1} \quad (4.21)$$

in the case of our simulation $\phi_0 = 1$, $N_F = 10$ and $M = 18$. The spatial frequency that satisfies this condition is $\xi \ll 3.3$. This is consistent with Figure 4.6, where we see that some deviations start to occur for $\xi > 3.3$. The agreement actually appears to be

very good even when $\xi \approx 3.3$. This is probably because a $\cos(\mathbf{k}_s \cdot \mathbf{r})$ term has been neglected from Equation 4.11 as it is always ≤ 1 , when it is included the restriction on the remaining terms in Equation 4.11 is relaxed somewhat.

4.3 Experimental test of the model

In this section we test experimentally the validity of the x-ray phase image model. The sample is made from a polyimide film (Kapton) with composition $C_{22}H_{10}N_2O_4$ and density $1.45g/cm^3$. This is the same material that we used in the numerical simulation. Laser ablation by a mask projection micromachining system, which used a Lambda Physik LPX210i krypton fluoride excimer laser operating at 248 nm, was used to etch a grid of lines on the film ¹. The sample produced had a phase modulation designed to have a square wave profile. However, the beam profile and other effects in the ablation process result in a tapered wall with rounded edges so that the resulting profile is a reasonable approximation to that described in Equation 4.6. Three grid size periods were used: $43\mu m$, $20\mu m$ and $10\mu m$, see Figure 4.7. The depths of the grids were measured using optical microscopy and the amplitudes of the modulations were found to be $40 \pm 5\mu m$, $30 \pm 5\mu m$ and $20 \pm 5\mu m$ respectively.

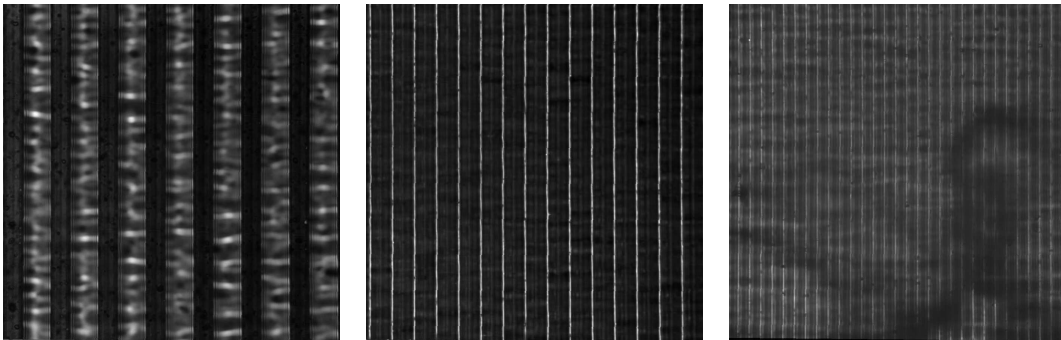


Figure 4.7: Micrograph of the three grids with periods of $43\mu m$, $20\mu m$ and $10\mu m$ as used in the experimental work. The images are focused on the top layer of the sample.

The experiments were performed with a conventional micro focus x-ray tube source

¹We would like to acknowledge J.P. Hayes (Industrial Research Institute Swinburne) for providing the Kapton sample.

[fei93a] using Cu as a target. The tube voltage was 20 kV and current $400 \mu A$. The spectrum of the source was measured (see Figure 3.2) in order to quantify the experimental x-ray data sets. The non-monochromaticity of the radiation can be dealt with

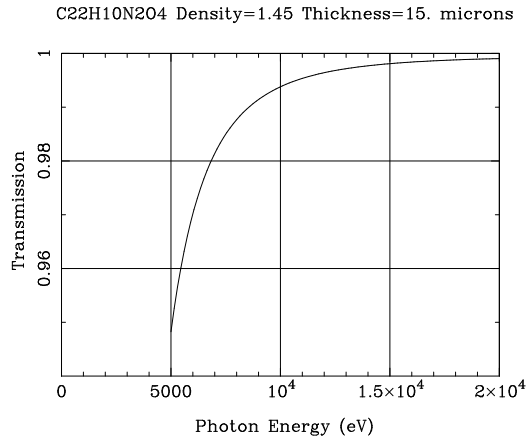


Figure 4.8: The transmission of $15 \mu m$ polyimide sample in the interested energy range.

by making a weighted sum of the energy spectrum and using it to calculate an effective wavelength for the analysis. When an object has an absorption edge in the energy spectrum, the effective wavelength will be different. An effective wavelength can still be identified but it no longer has a simple relationship to the spectrally weighted sum wavelength, as is done later in Subsection 5.1.2. The polyimide sample used here does not show an absorption edge in the relevant energy range, see Figure 4.8². We cal-

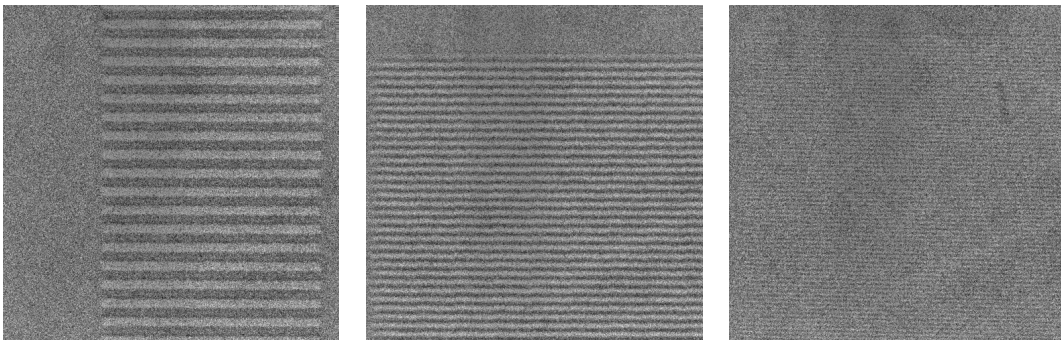


Figure 4.9: X-ray images of the sample shown in Figure 4.7 at the detector plane for an exposure time of 60 seconds. The samples are placed horizontally and the source had a FWHM of $14 \mu m$.

²This plot is retrieved from The center for x-ray optics (CXRO) at Lawrence Berkeley National Lab-

culated the effective x-ray energy of our spectrum to be 11 keV. At this energy, the transmission through the thickest part of the polyimide sample ($40\mu m$) is 98.6% thus making the sample essentially a phase object.

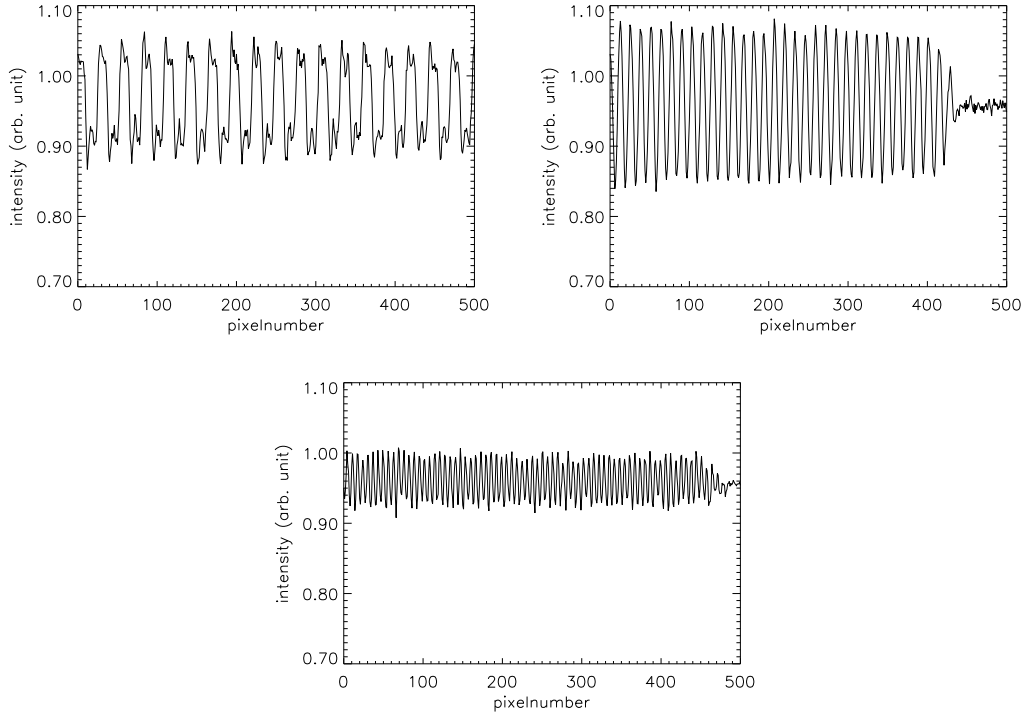


Figure 4.10: Average intensity in the row direction for the periods of $43\mu m$, $20\mu m$ and $10\mu m$.

As reported in Chapter 3, the actual source size was measured and was found to have a vertical FWHM of $14 \pm 5\mu m$ and a horizontal FWHM of $19 \pm 5\mu m$. Thus our theory can be tested for two different source sizes by placing the sample either horizontally or vertically. The sample was placed at a distance of $z_1 = 10 \pm 0.5cm$ from the source and the detector was placed at $z_2 = 170 \pm 2cm$ from the sample. The images were recorded through a direct-detection CCD camera (liquid nitrogen cooled Photometrics CH260), with 512×512 and $27\mu m \times 27\mu m$ pixels. The recorded intensities are shown in Figure 4.9 for horizontally placed samples. The detector resolution will not limit the image resolution of the smallest sample period of $10\mu m$ because the image magnification in this system is 18x. The object period of $10\mu m$ is represented by about 7 pixels in the

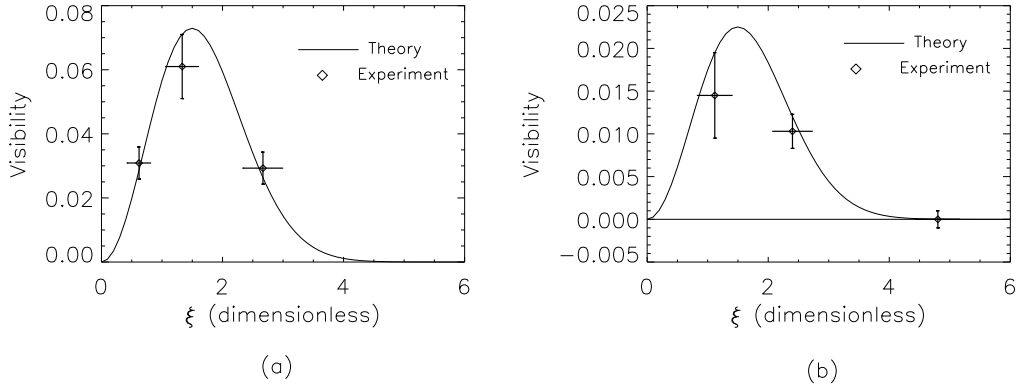


Figure 4.11: A comparison of the experiment results with the predictions of our imaging model. (a) Horizontally orientated sample with a source FWHM of $10\mu m$, and (b) Vertically orientated sample with a source FWHM of $18\mu m$.

detector. The intensity images were corrected for the dark current image and for non-uniform illumination in the imaging system, according to Equation 3.3. Figure 4.10 shows the intensity averaged in the row direction for the sample periods of $43\mu m$, $20\mu m$ and $10\mu m$. This averaging process was done to increase the photon statistics.

The visibility is then obtained for each of the images, according to Equation 3.6, and compared to the prediction of Equation 4.19. We can therefore scale the results for the different sample thicknesses to a common arbitrary thickness, here we choose $15\mu m$. The results are shown in Figure 4.11 for the two sample orientations for the three sample periods for a thickness of $15\mu m$. This figure shows that the prediction of Equation 4.19 using the test fit values of a vertical FWHM of $10\mu m$ and a horizontal FWHM of $18\mu m$ are consistent with our independent source size measurement. Our experimental results indicate that there is a good agreement between theoretical and experimental results for the visibility.

4.4 Objective image filtering

The visibility curve given in Equation 4.19 dictates that an object with a certain spatial frequency should be acquired at a particular optimal magnification. Different spatial frequencies have different optimal magnifications. So for a real object with multiple

spatial frequencies, we want to define a strategy that allows us to objectively combine multiple images which are each optimal for a particular spatial frequency. Our strategy is to weight the contribution of each image according to the magnitude of the visibility function for the optimal spatial frequency of each image.

We suppose that N images have been acquired at a number of different magnification factors, by placing the detector at a number of different distances and keeping constant the sample to source distance. The combined image is then obtained by weighting the spectral images as follows:

$$\tilde{I}(\mathbf{u}) = \sum_{i=1}^N \frac{\bar{V}(\boldsymbol{\xi}, M_i)}{V_T(\boldsymbol{\xi})} \tilde{I}_i(\mathbf{u}) \quad (4.22)$$

where

$$V_T(\boldsymbol{\xi}) = \sum_{j=1}^N \bar{V}(\boldsymbol{\xi}, M_j) \quad (4.23)$$

\bar{V} is the visibility function from Equation 4.19 normalized to have unity as the maximum value. It may be noted that in this case we do not need to know the values of $|\phi_0|$ (or N_F) a priori. The characteristic spatial frequency $\boldsymbol{\xi} = (\xi_x, \xi_y)$ is a two dimensional vector in the transverse direction. Denote $\tilde{I}(\mathbf{u})$ as the Fourier transform of the function $I(\mathbf{r})$. Then $\tilde{I}_i(\mathbf{u})$ is the Fourier transform of the i^{th} image and $\tilde{I}(\mathbf{u})$ is the Fourier transform of the combined image.



(a)



(b)

Figure 4.12: (a). The input intensity in the plane $z_2 = 0$ varies from 0.996 (black) to 1 (white) in arbitrary units. (b) The input phase shift varies from 0 (black) to 2 (white) in radian.

Through a numerical model, we will show how this strategy of objective filtering leads to a marked increase in image quality across the spatial frequency spectrum. A transparent sample was taken to have the properties of polyimide film with density $1.45\text{g}/\text{cm}^3$. The dimensions of the sample are $500 \times 500\mu\text{m}$ square with a thickness varying from 0 to $15\mu\text{m}$. The simulation is made at an x-ray energy 11 keV ($\lambda = 1.1\text{\AA}$). For these parameters, the thickest part of the sample has 99.6 % transmission. Figure 4.12³ shows the radiation exit wave function after the sample, in terms of intensity and phase shifts at the plane $z = 0$. The input intensity in the plane $z = 0$ varies from 0.996 (black) to 1 (white) in arbitrary units. The input phase shift varies from 0 (black) to 2 (white) in radian. This field is then propagated numerically through free space, in order to simulate the coherent intensity at some distance downstream of the sample, using the Fresnel diffraction formalism. Two different propagation distances have been chosen: $z_1 = 0.3\text{m}$ and $z_2 = 0.06\text{m}$ to represent a small magnification ($M = 1.2\text{x}$); and $z_1 = 0.3\text{m}$ and $z_2 = 1.2\text{m}$ to represent large magnification ($M = 5\text{x}$). The coherent intensity is then convolved with an appropriately magnified Gaussian

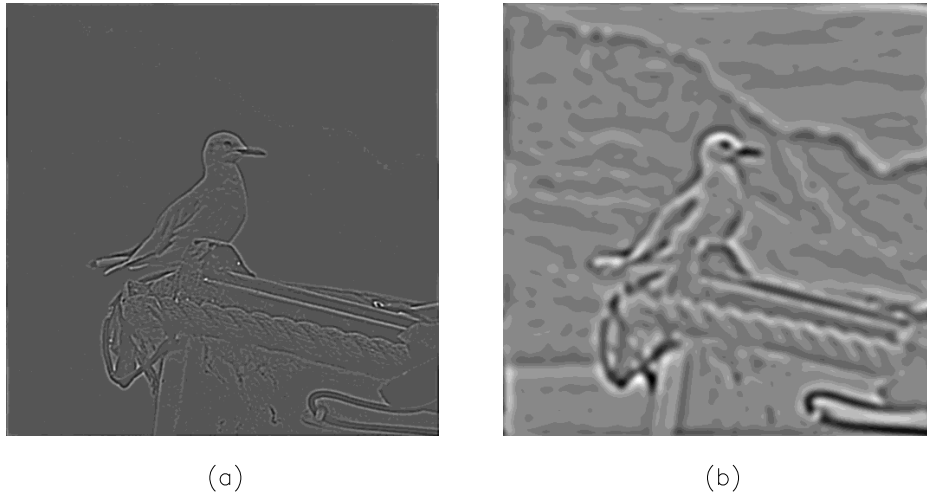


Figure 4.13: (a). Small magnification image ($M = 1.2\text{x}$) has been taken at $z_1 = 0.3\text{m}$ and $z_2 = 0.06\text{m}$. (b). Large magnification image $M = 5\text{x}$ has been taken at $z_1 = 0.3\text{m}$ and $z_2 = 1.2\text{m}$.

source distribution with $\text{FWHM} = 15\mu\text{m}$. A convolution of each figure with a magnified Gaussian source distribution will represent the actual image in the detector plane. The

³This figure is a photograph taken by a friend, <http://www.paswindar.com/> and is used with permission

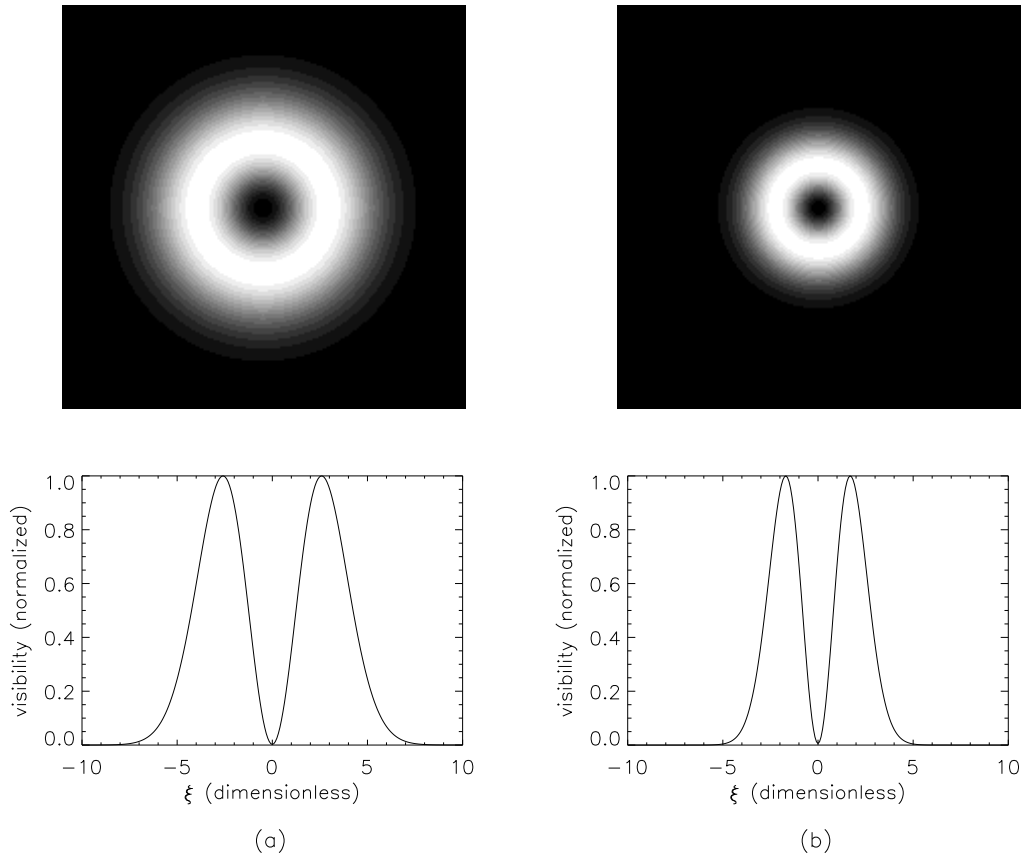


Figure 4.14: Normalized visibility for (a). small magnification condition (b). large magnification condition. (The top plots show two dimensional visibility as a function of spatial frequencies ξ_x and ξ_y . The bottom plots show the visibility along the angular radial direction).

small magnification ($M = 1.2x$) and large magnification ($M = 5x$) images are shown in Figure 4.13. We notice that each of these images contains significantly different information. More information concerning higher spatial frequencies is contained in the low magnification data sets of Figure 4.13(a). In contrast, the large magnification data sets of Figure 4.13(b) contain more information regarding the lower spatial frequencies. This is a manifestation of the frequency dependence on propagation distance as we described earlier. In a real experiment, achieving high spatial frequency images at small magnification is a difficult task because the detector resolution becomes the limiting factor in the visibility. We need, in this case, a very high spatial resolution detector. Figure 4.14 shows the normalized visibility that we used to process the images for objective filtering. Based on Figure 4.14(a), we see that visibility is nearly zero at $|\xi| \approx 7$ for the small magnification case. This means that object features of around $6\mu m$ will

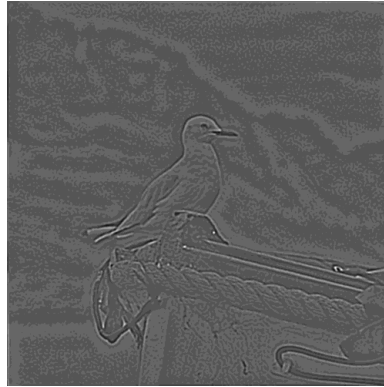


Figure 4.15: The combined image using Equation 4.22 and 4.23. The image quality is improved obviously.

start to vanish. While for the high magnification case of Figure 4.14(b) smallest object features of around the size of the source are just visible. Using the normalized visibility, the images in the Figure 4.13 were then processed according to the objective filtering in Equations 4.22 and 4.23, in order to yield contrast enhancement for the whole frequency range. The result is given in Figure 4.15. The improvement in the image quality is obvious. Figure 4.16 gives a comparison of the spatial frequency information along a horizontal line through the center of the images in Figures 4.13 and 4.15 in the first 150 pixels. The plot shows how the objective filtering combines the high spatial frequencies

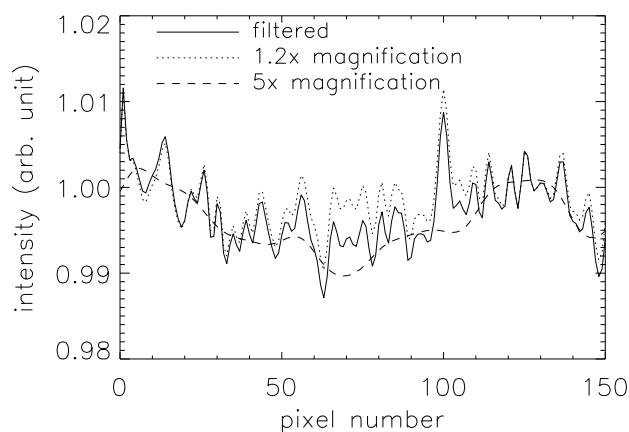


Figure 4.16: Comparison of the spatial frequency information along a horizontal line through the center of the individual images and the combined image, in the first 150 pixels.

and the low spatial frequencies.

4.4.1 Implications for quantitative phase retrieval

In this subsection we consider the implication of objective filtering for the phase retrieval images that we discussed in Section 2.4.2. In a noise free environment, the best condition for phase recovery is for very small z_2 because in this case, source blurring will be negligible (see Equation 3.1). In this condition the retrieved phase is perfect for both high frequency and low frequency features. However, in practice we do not have a noise free environment. In the presence of noise the retrieved phase from a very small z_2 will more sensitive to noise than one from a larger z_2 [Pag04a]. For small z_2 the change in intensity due to the evolution of the image on propagation is small; for large z_2 it is larger. Thus in the latter case a given amount of noise has less effect. Therefore



Figure 4.17: Phase retrieval in a noise free environment for (a) small propagation distance $z_2 = 0.03m$, phase retrieval is perfect for the whole frequency spectrum, and (b) larger distance $z_2 = 0.63m$, the source blurring influences phase retrieval.

increasing z_2 will reduce the effect of noise. But this will result in source blurring. The objective filtering criterion in Equations 4.22 and 4.23 can be used to improve this problem by creating a frequency weighted average of the phase based on multiple data sets. The lost information because of noise in the case of very small z_2 is ameliorated when combined with information from a larger propagation distance which is more stable to

noise. As we use a simple weighted average of the data sets the resulting image has essentially the same frequency spectrum as the true image.

Noise can occur for many reasons in practice, including poor dynamic range in the detector, a weak radiation source that requires a long exposure time, and electronic noise in the detector. In order to model the noise, we use pseudo-random numbers with a normal (Gaussian) distribution with a mean of zero and a standard deviation of a percentage of the mean intensity. For each pixel location, the noise is added to each raw intensity value from which the phase is calculated.

To consider the effects of noise we start with a numerical model for a phase image obtained in a noise free environment. This is shown in Figure 4.17. Figure 4.17(a) is the retrieved phase for small z_2 and is reconstructed from Figure 4.12(a) at $z_2 = 0$ and Figure 4.13(a) at $z_2 = 0.06m$. The phase retrievals were calculated using the Transport of Intensity Equation, as shown in Equation 2.57 which determines the phase of the object by measuring the intensity and intensity derivative of the data. This reconstruction can be assumed to be made at the mid plane between the two data sets and so is at a distance $z_2 = 0.03m$, corresponding to $M = 1.1$. Note that the data was taken at a source sample distance of $z_1 = 0.3m$. The figure shows that the retrieved phase is perfect for the whole frequency range. On the other hand, Figure 4.17(b) is the retrieved phase for larger z_2 . We use Figure 4.13(a) at $z_2 = 0.06m$ and 4.13(b) at $z_2 = 1.2m$ for the input intensities. This second reconstruction will correspond to a mid plane from the two data sets and so is at distance of $z_2 = 0.63m$, with $M = 3.1$. The effect of source blurring on the retrieved phase is clearly seen.

The effect of noise in the mid plane intensity and the intensity derivative of the modelled data can be seen in Table 4.1. We see that in the presence of noise, the intensity derivative for the large propagation distance is more stable to noise than for the short propagation distance. If propagation distance is increased then this will tend to reduce the effect of noise because of the construction of the derivative in the intensity $\partial I / \partial z$. However, it should be recalled that the effect of this strategy for reducing the effect of noise will be limited by the image blurring that becomes apparent at larger propagation distances due to finite source size. A more rigorous explanation regarding

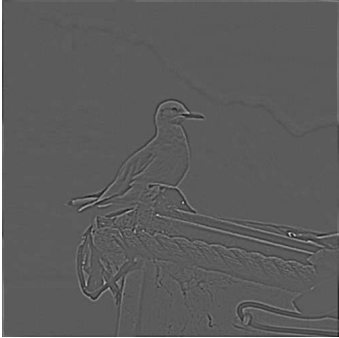
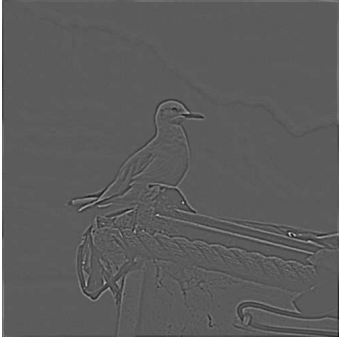


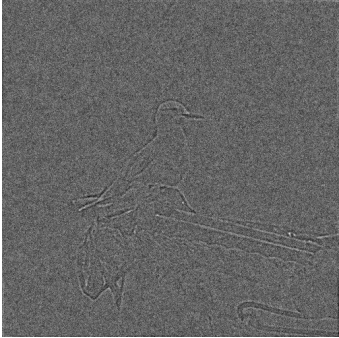
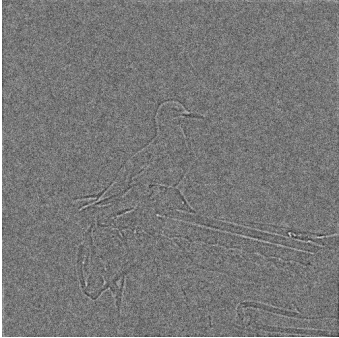


Noise 0 %	$\text{mid plane intensity}(\frac{I_1+I_2}{2})$	$\frac{\partial I}{\partial z}$
small propg.		
large propg.		
Noise 10 %	$\text{mid plane intensity}(\frac{I_1+I_2}{2})$	$\frac{\partial I}{\partial z}$
small propg.		
large propg.		

Table 4.1: The effect of noise on $\frac{\partial I}{\partial z}$ for small and large propagation distances.

the presence of noise in the phase retrieval can be found in the PhD thesis of Paganin [Pag99]. From Equation 2.12, we understand that increasing propagation distance can be done by increasing either z_1 or z_2 . If increasing propagation distance is to be done by increasing the source sample distance z_1 , the requirement of 'small' in Equation 4.11 must be fulfilled.

The effect of noise on the retrieved phase can be seen in Table 4.2. The first column of the figure shows phase retrieval for the small propagation distance $z_2 = 0.03m$ with a variation in the noise percentage. The second column shows phase retrieval for the larger propagation distance $z_2 = 0.63m$. The loss of information due to noise is seen to be more severe in the small propagation case as is expected. In the third column of Table 4.2, the objective filtering criterion for phase images has been implemented, similar to Equation 4.22, as follows:

$$\tilde{\phi}(\mathbf{u}) = \sum_{i=1}^N \frac{\overline{V}(\boldsymbol{\xi}, M_i)}{V_T(\boldsymbol{\xi})} \tilde{\phi}_i(\mathbf{u}) \quad (4.24)$$

where $\tilde{\phi}_i(\mathbf{u})$ is the Fourier transform of the i^{th} retrieved phase image and $\tilde{\phi}(\mathbf{u})$ is the Fourier transform of the combined phase image. An improvement in the phase image is readily apparent. We conclude that around 5% noise is at the upper limit for which a reasonable image can be retrieved for this system, though improvement is seen in our cases.

Quantitative improvement of the retrieved phase when considering the combined image is apparent via a comparison of the real phase and the phase reconstruction in the presence of 3% noise, see Figure 4.18. We see how the objective filtering strategy takes the combination of small magnification and large magnification images so that the filtered image is a better match to the real phase features. Note that there is an arbitrary dc offset in the retrieved phase which means that the filtered phase, shown in Figure 4.18 can be offset downward to more closely align with the real value.

The phase image obtained using the objective filtering strategy led to a marked increase in quality across the whole spatial frequency spectrum, as shown in Table 4.2. This is helpful when attempting to solve problems in phase retrieval in the presence of noise and allows an optimal phase recovery to be achieved. This filtering strategy can













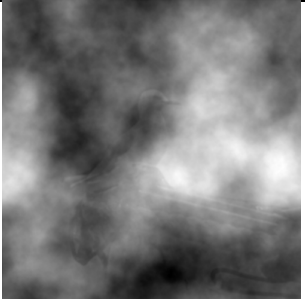
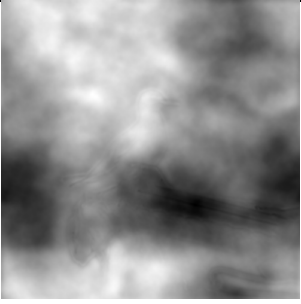

Noise	$z_2 = 0.03m$	$z_2 = 0.63m$	filtered image
0%			
1%			
3%			
5%			
8%			

Table 4.2: The effect of noise on the retrieved phase and the improvement in the phase image using the objective filtering strategy.

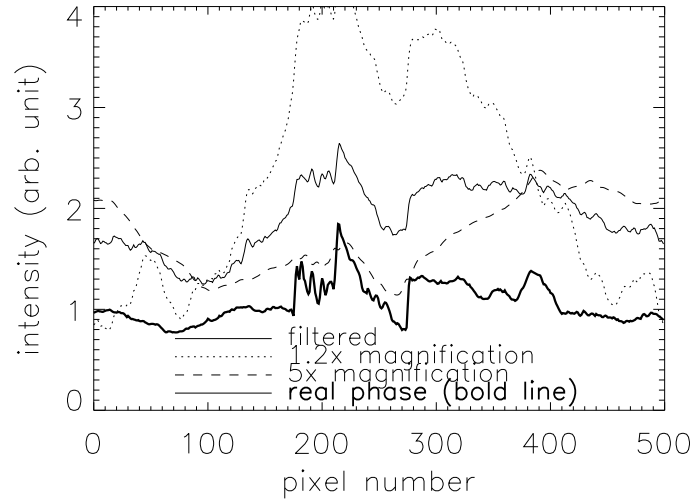


Figure 4.18: Comparison of the real phase with the phase reconstruction in the presence of 3% noise, along a horizontal line through the center of images. An arbitrary constant offset in the phases has been retained for case of comparison.

also be implemented for the tomographic reconstruction of more structurally complex 3D objects as is shown later in Section 6.3.1.

4.4.2 Objective filtering for experimental phase retrieval data

In this subsection⁴, we show the application of the objective filtering criterion for experimental neutron data. Experiments were conducted at the National Institute of Standards Technology (NIST), NG0 Neutron Depth Profiling Facility, NIST Center for Neutron Research (NCNR), Gaithersburg, MD, USA using a thermal distribution of neutrons with a wavelength peak of 4.32\AA [McM01].

The experimental set up is shown in Figure 4.19. The source was a beam of neutrons delivered by a neutron guide. A $200\mu\text{m}$ diameter pinhole was placed at the exit of the beam port in order to provide a point-like source of illumination. Then another 25.4mm aperture is placed about 1.5m further downstream of the pinhole, in order to define the

⁴We would like to acknowledge Dr. Philip McMahon, Dr. Brendan Allman, Dr. D. L. Jacobson, and Dr. M. Arif who acquired the neutron image data used here and in the published paper by Arhatari et.al. [Arh04].

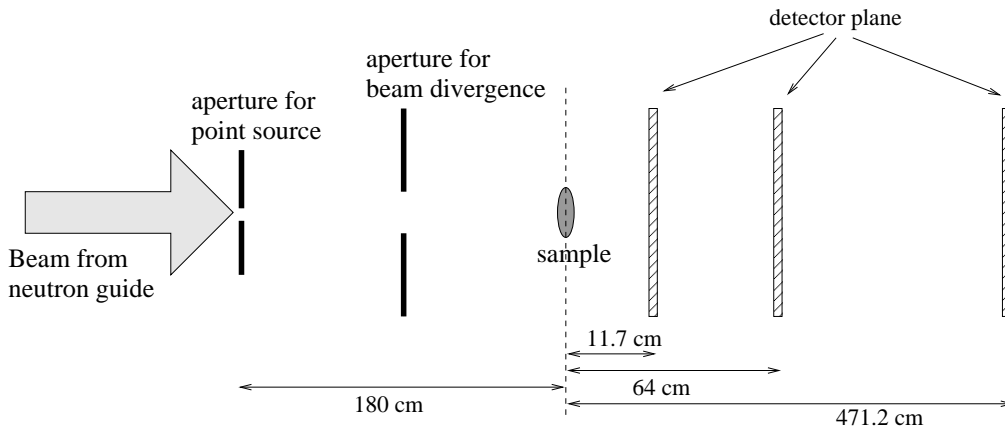


Figure 4.19: Schematic set up of the neutron experiment



Figure 4.20: The tapered lead slug sample used in the neutron experiment. The scale is in millimeters.

maximum beam divergence. The sample in this experiment was a tapered lead slug approximately 15mm in length and 8mm in maximum diameter, with an approximately 1.5mm hole drilled through the center, see Figure 4.20.

The sample was placed at $z_1 = 1.8m$ from the first pinhole. Intensity images were recorded using an NE426 neutron scintillator screen coupled with an optical CCD camera with 512x512 pixels of $50\mu m$ size. Three images were collected for three differing propagation distances from the sample, allowing two different retrieved phase images to be reconstructed. The first phase reconstruction can be assumed to be made at the mid plane between the two distances $z_2 = 11.7cm$ and $z_2 = 64cm$ and so is at a dis-

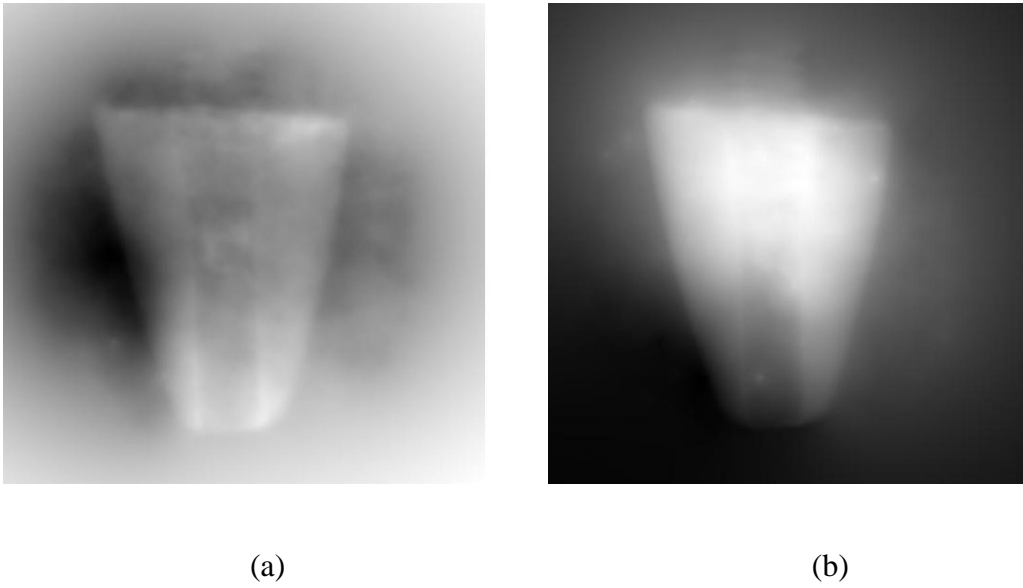


Figure 4.21: (a). Recovered phase from small magnification image ($M = 1.21x$) (b). Recovered phase from large magnification image $M = 2.49x$.

tance of $z_2 = 37.9cm$ corresponding to $M = 1.21$. The second phase reconstruction will correspond to a mid plane between the distances $z_2 = 64cm$ and $z_2 = 471.2cm$ and so is at $z_2 = 267.6cm$, with $M = 2.49$. Both phase reconstructions are shown in Figure 4.21⁵.

We see that each of these images contains significantly different information. This is a manifestation of the presence of noise in the phase reconstruction and of source blurring. The closer image 4.21(a) tends to lose some low spatial frequency information due to noise. The far image 4.21(b) tends to lose some high spatial frequency information due to the blurring effect because of the finite source size. The objective filtering criterion of Equations 4.24 was then used for the image combination strategy. The result is shown in Figure 4.22. Improvement in the image quality is obvious across the spatial frequency range. Quantitative comparison has been made between the standard deviation of the calculated phase reconstructions based on the knowledge of the composition and size of the sample and the standard deviation of the combined phase image of Figure 4.22. It was found that the combined image has been improved by a factor of 8 over the image in Figure 4.21(a), and by a factor of 2 over the image in

⁵The phase images and the filtered image presented here were calculated by Adrian P. Mancuso.

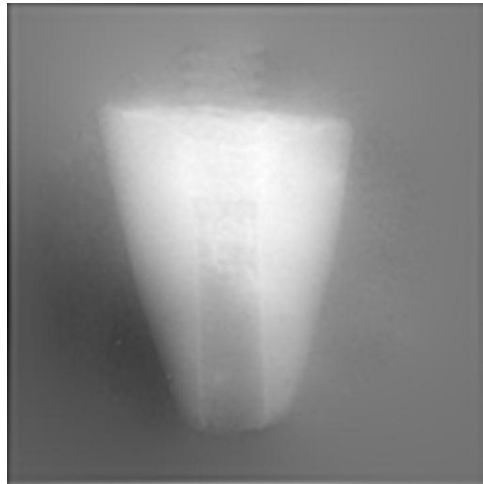


Figure 4.22: The combined image using objective filtering strategy.

Figure 4.21(b).

Chapter 5

Image modelling for complex objects

In this chapter, we extend the phase contrast analysis developed in Chapter 4 to the case of a complex object. That is an object with some degree of absorption as well as phase shift. Parts of this chapter have been published [Arh05]. In Section 5.1, we begin by developing an image model in the region for which the transport of intensity equation (TIE) is valid. This validity can be achieved by requiring only a small propagation distance. The polychromatic nature of the beam is also considered in the development of the image model. Experimental testing using an x-ray laboratory source has also been done, and the results are in excellent agreement with theory. We show also a useful application of the image model and illustrate its potential for improving resolution and contrast. In Section 5.2 we describe an alternative image model that is valid for larger propagation distances. The trade off is that this approach requires an additional condition for validity; that is that the objects are low in absorption and slowly varying in phase. Both models incorporate an extended partially coherent source. We discuss the comparison of both approaches in Section 5.3. Hopefully, these considerations can give a basic principal allowing for the establishment of practical applications in x-ray radiography.

We consider a uniform transmission sample with a one-dimensional harmonic phase and attenuation variation. The wave field at the exit surface of the sample (i.e. at

distance $z = 0$) can be described by the complex function:

$$S(\mathbf{r}, 0) = S_0 \exp[i\phi(\mathbf{r}) - \frac{1}{2}\mu(\mathbf{r})]$$

or

$$S(\mathbf{r}, 0) = S_0 \exp[i\phi_0 \cos(\mathbf{k}_s \cdot \mathbf{r}) - \frac{1}{2}\mu_0 \cos(\mathbf{k}_s \cdot \mathbf{r})] \quad (5.1)$$

The sample influences not only the phase but also the intensity of the beam. The phase shift, $\phi(\mathbf{r})$, and attenuation variation, $\mu(\mathbf{r})$, introduced by the sample, are given by:

$$\begin{aligned} \phi(\mathbf{r}) &= \phi_0 \cos(\mathbf{k}_s \cdot \mathbf{r}) = -\frac{2\pi}{\lambda} \int \delta \cos(\mathbf{k}_s \cdot \mathbf{r}) dz \\ &= -\frac{2\pi}{\lambda} \delta t \cos(\mathbf{k}_s \cdot \mathbf{r}) \end{aligned} \quad (5.2)$$

$$\begin{aligned} \mu(\mathbf{r}) &= \mu_0 \cos(\mathbf{k}_s \cdot \mathbf{r}) = \frac{4\pi}{\lambda} \int \beta \cos(\mathbf{k}_s \cdot \mathbf{r}) dz \\ &= \frac{4\pi}{\lambda} \beta t \cos(\mathbf{k}_s \cdot \mathbf{r}) \end{aligned} \quad (5.3)$$

where t is the amplitude of the modulation on the sample. Both functions 5.2 and 5.3 give the projection of a characteristic of the object along the optical axis.

5.1 Image modelling for short propagation distances

5.1.1 Image formation model

The basic configuration of the propagation-based phase contrast formation used here is the same as in Figure 4.1. Using Equation 5.1, the coherent intensity image of the transmission function directly after the sample (i.e at $z = 0$) is:

$$I_{coh}(\mathbf{r}, 0) = |S(\mathbf{r}, 0)|^2 = I_0 \exp[-\mu_0 \cos(\mathbf{k}_s \cdot \mathbf{r})] \quad (5.4)$$

For sufficiently short propagation distances, we can use the transport of intensity equation (TIE). Using Equation 5.2 for the phase shift and Equation 5.4 for the coherent intensity directly after the sample, the TIE in Equation 4.7 takes the form:

$$\frac{\partial I_{coh}(\mathbf{r}, 0)}{\partial z} = \frac{I_0 \phi_0 k_s^2}{k_0} e^{-\mu_0 \cos(\mathbf{k}_s \cdot \mathbf{r})} [\mu_0 \sin^2(\mathbf{k}_s \cdot \mathbf{r}) + \cos(\mathbf{k}_s \cdot \mathbf{r})] \quad (5.5)$$

Assume a small propagation distance, z , such that

$$I_{coh}(\mathbf{r}, z) = I_{coh}(\mathbf{r}, 0) + z \frac{\partial I_{coh}(\mathbf{r}, 0)}{\partial z} \quad (5.6)$$

where, as we mentioned before, 'small' means that:

$$z \frac{k_s^2}{k_0} \mid \phi_0 \mid \ll 1 \quad (5.7)$$

Substituting Equation 5.4 and Equation 5.5 into Equation 5.6, we get:

$$I_{coh}(\mathbf{r}, z_2) = I_0 e^{-\mu_0 \cos(\mathbf{k}_s \cdot \mathbf{r})} \left[1 + \frac{z_2 \phi_0 k_s^2}{k_0} \cos(\mathbf{k}_s \cdot \mathbf{r}) + \frac{z_2 \phi_0 \mu_0 k_s^2}{k_0} \sin^2(\mathbf{k}_s \cdot \mathbf{r}) \right] \quad (5.8)$$

An extended spherical wave source with spatial distribution $\sigma(\mathbf{r})$, as described in Equation 4.2, is located at a distance z_1 from the sample. The intensity measured at a distance z_2 from the sample, is then given by the convolution of the coherent intensity image at the measured plane, $I_{coh}(\mathbf{r}, z_2)$, with the source distribution:

$$I(\mathbf{r}, z_2) = \frac{1}{M^2} \int I_{coh}\left(\frac{1}{M}\mathbf{r}', \frac{1}{M}z_2\right) \sigma\left(\frac{1}{M-1}[\mathbf{r} - \mathbf{r}']\right) d\mathbf{r}' \quad (5.9)$$

Using Equation 5.8 for the coherent intensity, we can rewrite the above equation as:

$$\begin{aligned} I(\mathbf{r}, z_2) = \frac{I_0}{M^2} & \left[\frac{1}{(M-1)\sigma_s\sqrt{2\pi}} \int e^{-\mu_0 \cos(\mathbf{k}_s \cdot \frac{\mathbf{r}'}{M}) + \frac{(\mathbf{r}-\mathbf{r}')^2}{(M-1)^2 2\sigma_s^2}} d\mathbf{r}' \right. \\ & + \frac{1}{(M-1)\sigma_s\sqrt{2\pi}} \frac{z_2 \phi_0 k_s^2}{M k_0} \int e^{-\mu_0 \cos(\mathbf{k}_s \cdot \frac{\mathbf{r}'}{M}) + \frac{(\mathbf{r}-\mathbf{r}')^2}{(M-1)^2 2\sigma_s^2}} \cos(\mathbf{k}_s \cdot \frac{\mathbf{r}'}{M}) d\mathbf{r}' \\ & \left. + \frac{1}{(M-1)\sigma_s\sqrt{2\pi}} \frac{z_2 \phi_0 \mu_0 k_s^2}{M k_0} \int e^{-\mu_0 \cos(\mathbf{k}_s \cdot \frac{\mathbf{r}'}{M}) + \frac{(\mathbf{r}-\mathbf{r}')^2}{(M-1)^2 2\sigma_s^2}} \sin^2(\mathbf{k}_s \cdot \frac{\mathbf{r}'}{M}) d\mathbf{r}' \right] \quad (5.10) \end{aligned}$$

The difficulty of the integrals in this equation is strongly dependent on the model chosen for the source distribution. In this case the gaussian distribution makes the integrals intractable. However, in general we can simplify matters by limiting the analysis to low absorption objects. This does limit the generality of the TIE-based expression somewhat. However, we still obtain an expression which is valid for a different set of approximations than those developed previously; being that of pure phase [Arh04] or slowly varying phase and small absorption [Tur04a]. As we shall also see, the approximation allows us to develop the intensity expression into one based on the visibility of the propagated object, which extends our previous pure phase result. By making the small μ_0 approximation and expanding the exponential in Equation 5.8 to first order in μ_0 , then applying the meaning of 'small' in Equation 5.7 we obtain:

$$I_{coh}(\mathbf{r}, z_2) = I_0 \left[1 - \mu_0 \cos(\mathbf{k}_s \cdot \mathbf{r}) + \frac{z_2 \phi_0 k_s^2}{k_0} \cos(\mathbf{k}_s \cdot \mathbf{r}) \right] \quad (5.11)$$

Using this equation for the coherent intensity and convolving with the source distribution, we can rewrite Equation 5.9 for the measured intensity as:

$$I(\mathbf{r}, z_2) = \frac{I_0}{M^2} \left(1 - \mu_0 \exp\left(-\frac{1}{2}\left[\frac{M-1}{M}\right]^2 \sigma_s^2 k_s^2\right) \cos(\mathbf{k}_s \cdot \frac{\mathbf{r}}{M}) \right. \\ \left. + \frac{z_2}{M} \phi_0 \frac{k_s^2}{k_0} \exp\left(-\frac{1}{2}\left[\frac{M-1}{M}\right]^2 \sigma_s^2 k_s^2\right) \cos(\mathbf{k}_s \cdot \frac{\mathbf{r}}{M}) \right) \quad (5.12)$$

Applying the dimensionless variables from Equation 4.14 as the Fresnel number of the source in the sample plane and Equation 4.15 as the number of resolution elements contained in the source, we get:

$$I(\mathbf{r}, z_2) = \frac{I_0}{M^2} \left(1 - \left[\mu_0 \exp\left(-\frac{1}{2}\left[\frac{M-1}{M}\right]^2 \xi^2\right) \right. \right. \\ \left. \left. - \frac{M-1}{M} \phi_0 \frac{\xi^2}{N_F} \exp\left(-\frac{1}{2}\left[\frac{M-1}{M}\right]^2 \xi^2\right) \right] \cos(\mathbf{k}_s \cdot \frac{\mathbf{r}}{M}) \right) \quad (5.13)$$

We again use the dimensionless distance $X = \mathbf{r}/\sigma_s$, so the equation can be expressed in term of ξ and M :

$$I(\xi, M) = \frac{I_0}{M^2} \left(1 - \left[\mu_0 \exp\left(-\frac{1}{2}\left[\frac{M-1}{M}\right]^2 \xi^2\right) \right. \right. \\ \left. \left. - \frac{M-1}{M} \phi_0 \frac{\xi^2}{N_F} \exp\left(-\frac{1}{2}\left[\frac{M-1}{M}\right]^2 \xi^2\right) \right] \cos\left(\xi \cdot \frac{X}{M}\right) \right) \quad (5.14)$$

If we introduce the definition of the general visibility function:

$$I(\xi, M) = \frac{I_0}{M^2} [1 - V_{TIE}(\xi, M) \cos(\xi \cdot \frac{X}{M})], \quad (5.15)$$

then we can see that the visibility function for a sample with a one dimensional harmonic phase and attenuation variation which takes into account the finite source size and contrast mechanism in small propagation distance (TIE) regime, is:

$$V_{TIE}(\xi, M) = \underbrace{\mu_0 \exp\left(-\frac{1}{2}\left[\frac{M-1}{M}\right]^2 \xi^2\right)}_{\text{absorption-term}} - \underbrace{\frac{M-1}{M} \phi_0 \frac{\xi^2}{N_F} \exp\left(-\frac{1}{2}\left[\frac{M-1}{M}\right]^2 \xi^2\right)}_{\text{phase-term}} \quad (5.16)$$

The equation contains separately the effects of absorption and phase. The first term of the equation (the absorption term) will have a maximum of μ_0 at $\xi \rightarrow 0$ for any magnification or when $M = 1$ for any spatial frequencies. The last term of the equation (the phase term) is the same as the visibility function for a pure phase sample, as we

have seen in Equation 4.19. This term dominates when the absorption is negligible or μ_0 is zero. The phase term will be maximum at $\xi \rightarrow \sqrt{2}$ for $M \rightarrow \infty$, as is described in Equation 4.20. The absolute value of the visibility as a function of spatial frequency and magnification can be seen in Figure 5.1. The figure shows the visibility for $10\mu\text{m}$ thick Aluminium at $\lambda = 1.1 \text{ \AA}$, for the case where the Fresnel number, $N_F = 10$, with the values of $\phi_0 = 1.26$ and $\mu_0 = 0.02$.

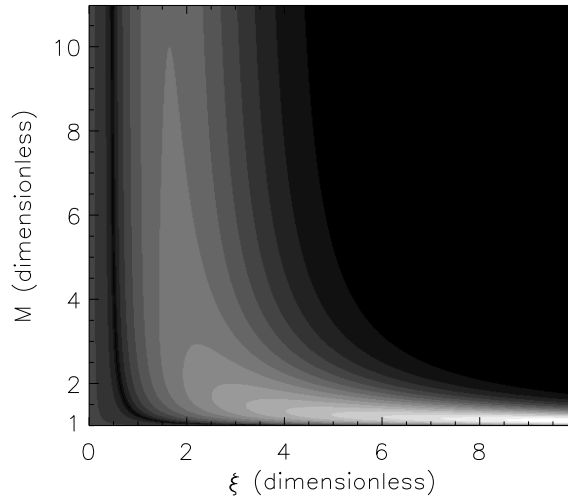


Figure 5.1: Visibility function as a function of spatial frequency, ξ , and magnification, M , for a sample with a one dimensional harmonic phase and attenuation variation, with $N_F = 10$. Black represents a 0 value, and white represents the highest value of 0.75.

Note that there are regions of parameter space for which the visibility vanishes. A certain object size will be invisible under this particular magnification condition. This happens at $\xi \approx 0.5$ for $M \rightarrow \infty$. This represents the worst case condition for imaging. Similarly, it can be seen that at a given magnification there will be an optimal visibility for a particular spatial frequency present in an object. The same phenomenon seen with the transparent sample are also observed here. At high magnification the visibility will be limited by the source size and the peak sensitivity occurs at low spatial frequency. The peak sensitivity of the visibility function moves to higher spatial frequencies when the magnification is slightly bigger than unity and will be limited by detector resolution.

5.1.2 Visibility for polychromatic phase contrast

We develop here a formalism for the visibility using a highly polychromatic beam. A characteristic property of our micro focus x-ray source is that it emits a range of energies, see Section 3.1.1. The effect of beam polychromaticity can be incorporated by using a wavelength-dependent combined detector response function and energy distribution of the beam, $D(\lambda)$.

$$D(\lambda) = S(\lambda)d(\lambda) \quad (5.17)$$

where $S(\lambda)$ is spectrum of the beam and $d(\lambda)$ is detector response function. We define a general visibility function for a polychromatic beam, based on our TIE model for small propagation distance:

$$\frac{I_{poly}(\mathbf{r})}{I_0} = \frac{\int I_\lambda(\mathbf{r})D(\lambda)d\lambda}{I_0 \int D(\lambda)d\lambda} = \frac{1}{M^2} \left[1 - V_{TIE,poly}(\xi, M) \cos(\mathbf{k}_s \cdot \frac{\mathbf{r}}{M}) \right] \quad (5.18)$$

where $V_{TIE,poly}$ is the visibility function for a polychromatic beam, based on small propagation distances, according the formula:

$$V_{TIE,poly} = \frac{\int V_{TIE}D(\lambda)d\lambda}{\int D(\lambda)d\lambda} \quad (5.19)$$

Thus we can obtain a polychromatic variant of the visibility function for samples with a one dimensional harmonic phase and attenuation variation, by multiplying both sides of Equation 5.16 by the wavelength dependent function $D(\lambda)$ and integrating over wavelength, to give:

$$V_{TIE,poly}(\xi, M) = \frac{\int \mu_0(\lambda)D(\lambda)d\lambda}{\int D(\lambda)d\lambda} \exp\left(-\frac{1}{2} \left[\frac{M-1}{M}\right]^2 \xi^2\right) - \frac{M-1}{M} \xi^2 \frac{\int \frac{\phi_0(\lambda)}{N_F(\lambda)} D(\lambda)d\lambda}{\int D(\lambda)d\lambda} \exp\left(-\frac{1}{2} \left[\frac{M-1}{M}\right]^2 \xi^2\right) \quad (5.20)$$

This expression is easily be evaluated because the spectrum and the wavelength dependent detector response are known, see Figure 3.2. This allows us to calculate the visibility function accurately, especially in the energy region when there is an absorption edge of the sample.

The plot in Figure 5.2 shows the difference in visibility between polychromatic and monochromatic beams for copper, $7.5\mu m$ thick, with an absorption edge in the interesting energy range. The $D(\lambda)$ used was that from Figure 3.2. The absorption edge of

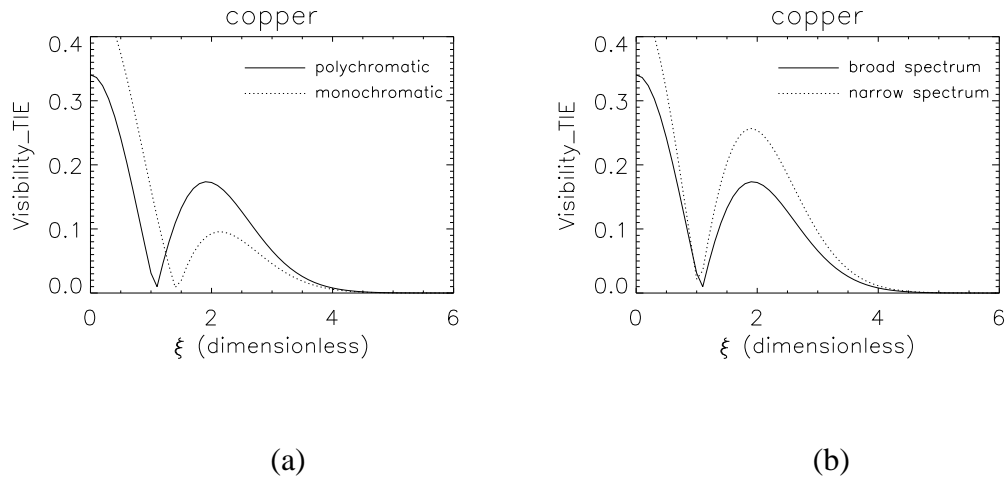


Figure 5.2: (a). Polychromatic effect compared with monochromatic for copper, $7.5\mu m$ thick, with an absorption edge. (b). Broad spectrum effect compared with narrow spectrum effect.

copper can be seen in Figure 5.5. We used Equation 5.20 to calculate the polychromatic effect with parameters $z_1 = 0.2m$, $z_2 = 1.6m$, $FWHM=14\mu m$. The monochromatic

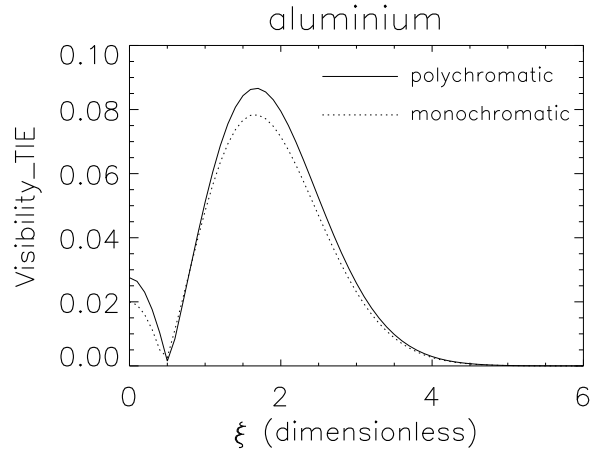


Figure 5.3: Polychromatic effect compared with monochromatic for aluminium, $7.5\mu m$ thick, far away from absorption edge.

effect for the same sample has been calculated with the same parameters using Equation 5.16 with a wavelength, $\lambda = 1.1 \text{ \AA}$, as a spectrally weighted sum from the energy spectrum. It seems that for particular object sizes, the polychromatic effect reduces the visibility in the absorption term but increases it in the phase term. The effect can also be characterized as a shifting in the spatial frequency response of the object. For

example an object with spatial frequencies that are invisible using a monochromatic beam, will be visible using polychromatic beam and vice versa. It is also worth noting that a filtered spectrum such as that produced from a broad source using a Ross filter can further improve the contrast. The effect is shown in Figure 5.2(b) where the broad spectrum of the source has a range as shown in Figure 3.2. The narrow spectrum has an effective range from 7 to 10 keV. While a narrow spectrum may increase the contrast, the reduction in flux may unacceptably degrade the signal to noise ratio.

Figure 5.3 shows the difference in visibility between a polychromatic and a monochromatic beam for aluminium, $7.5\mu m$ thick, far away from the absorption edge. There is very little difference between the two types of beam. The calculations were made using Equation 5.20 and the $\phi_0(E)$, and $\mu_0(E)$ data for aluminium, shown in Figure 5.4¹, for the polychromatic beam. Equation 5.16 was used for the calculations for the monochromatic beam, with $\lambda = 1.1 \text{ \AA}$.

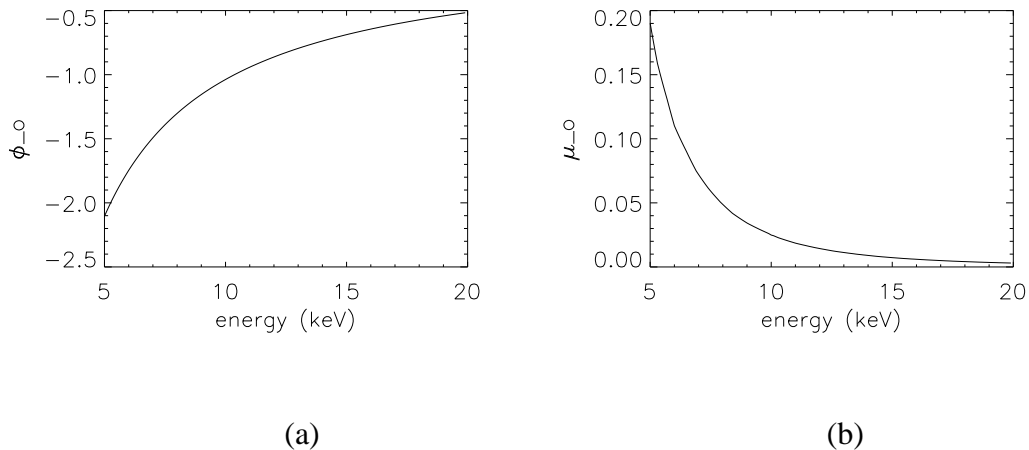


Figure 5.4: (a). $\phi_0(E)$ and (b). $\mu_0(E)$ of aluminium, used for calculating polychromatic effect.

5.1.3 Experimental test of the model

For the experiment, we used a series of copper grid meshes as the samples. Grids with six different mesh sizes were used to investigate six different spatial frequencies. The samples have both phase and attenuation variation, as described in Equation 5.1. The

¹This data is retrieved from NIST, National Institute of Standards and Technology, Physics Laboratory, USA, <http://physics.nist.gov/PhysRefData/FFast/html/form.html>.

grid size and thickness of these samples are shown in Table 5.1. The experiments were

Sample	Mesh size (periods per inch)	Period (μm)	Thickness (μm)
1	100	253.8	7.5
2	200	126.7	7.5
3	400	63.5	5
4	1000	25.4	2.5
5	1500	16.9	2.5
6	2000	12.7	2.5

Table 5.1: The periods and the thickness of the Copper grid mesh materials used in the experiment.

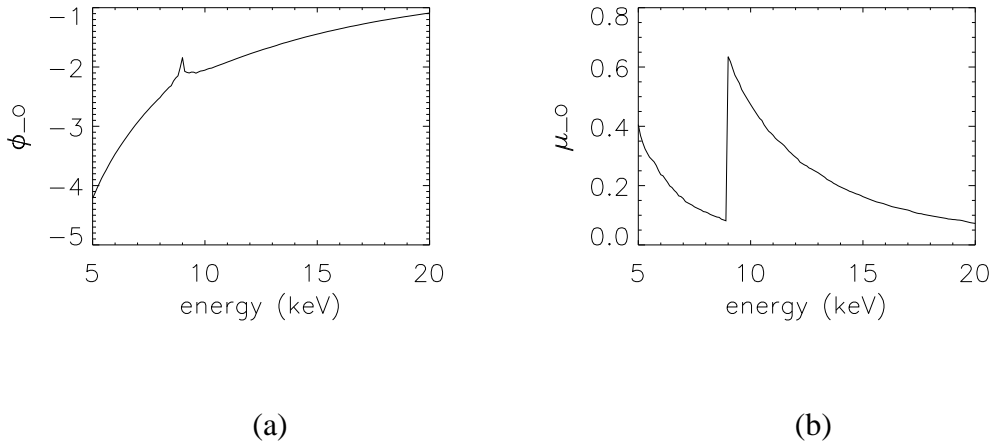


Figure 5.5: (a). $\phi_0(E)$ for a $2.5\mu m$ thick copper (b). $\mu_0(E)$ for a $2.5\mu m$ thick copper.

performed with a Fein Focus x-ray tube source, as we mentioned before with the same operating condition of 20 kV, 400 μA . The spectrum of the source was measured using a Si-PIN Photodiode x-ray detector. The imaging detector is a Photometrics CH260 CCD camera as used in the previous experiment. The combined detector response function and spectrum of the beam is shown in Figure 3.2 for 20 kV and is used for $D(\lambda)$ in calculating Equation 5.20. Copper has an absorption edge in the energy range used here,

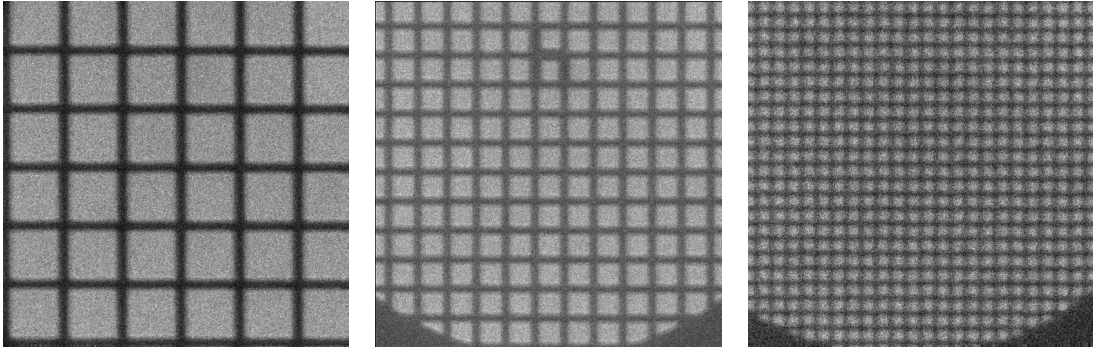


Figure 5.6: X-ray images of Sample 1,2 and 3 with respectively periods of $253.8\mu m$, $126.7\mu m$ and $63.5\mu m$.

see Figure 5.5 ², so it is necessary to take into account the polychromatic effect. The figures show the wavelength dependence of $\phi_0(E)$ and $\mu_0(E)$ for $2.5\mu m$ thick copper in the energy range from 5keV to 20keV. The source size was determined to have a vertical FWHM of $14 \pm 5\mu m$. As noted in Section 3.1 every filament change will lead

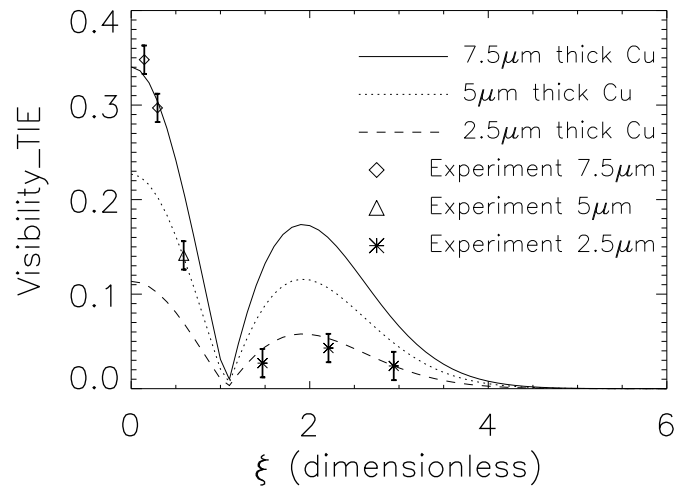


Figure 5.7: A comparison of the experimental results with the theoretical values for the polychromatic visibility from Equation 5.20, with a source FWHM of $14\mu m$. Three different sample thicknesses (see Table 5.1) have been used.

²This data is retrieved from NIST, National Institute of Standards and Technology, Physics Laboratory, USA, <http://physics.nist.gov/PhysRefData/FFast/html/form.html>.

to a difference source size. The sample was placed at a distance of $z_1 = 20 \pm 0.5\text{cm}$ from the source and the detector was placed at $z_2 = 160 \pm 2\text{cm}$ from the sample. This configuration satisfies the small propagation distance requirement with an effective z of 0.18m . The images in the detector plane from samples 1, 2, and 3 are shown in Figure 5.6. The intensity images were corrected for the dark current image and for non uniformities in the imaging system, using Equation 3.3. The horizontal visibility is then obtained using Equation 3.6 for each grid size and compared to the theoretical value of Equation 5.20. The results are shown in Figure 5.7. The vertical case is not discussed here as it had almost identical results to the horizontal.

The copper mesh samples we used had different thicknesses for different mesh dimensions. Consequently, there is a different visibility function corresponding to each different thickness. It can be seen over a range of different spatial frequencies and thicknesses that the agreement between the measured values and the predicted theoretical values is excellent.

5.1.4 Applications

Alternative method for source size measurement

One of many practical applications of the developed model for samples with phase and absorption variation is for source size measurement. A characteristic feature of

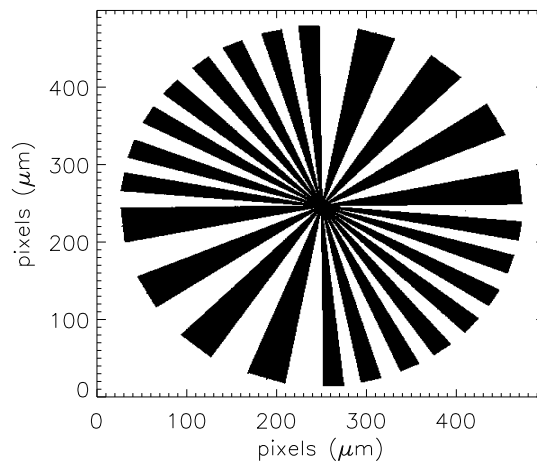


Figure 5.8: Star sample made of Aluminium, $5\mu\text{m}$ thickness.

the visibility function is the zero area or *the blind area*. In this region a given spatial frequency is invisible. If we examine a visibility plot without taking the absolute value, there will be a reversal from positive contrast to negative contrast in the object fringes as the spatial frequencies of the object pass through the blind area. This characteristic can be applied to a sample with gradually varying spatial frequencies. Such a sample might be the star sample, shown in Figure 5.8. We assume that the sample has the properties of aluminium with $5\mu m$ thickness. The object size is gradually varied with the spoke size variation. The size of the square area is $500 \times 500 \mu m$. For this numerical simulation we used an x-ray energy of 11 keV ($\lambda = 1.1\text{\AA}$). At this energy aluminium has $\beta = 4.476 \times 10^{-8}$ and $\delta = 4.528 \times 10^{-6}$. We used a source size of FWHM = $16\mu m$, with

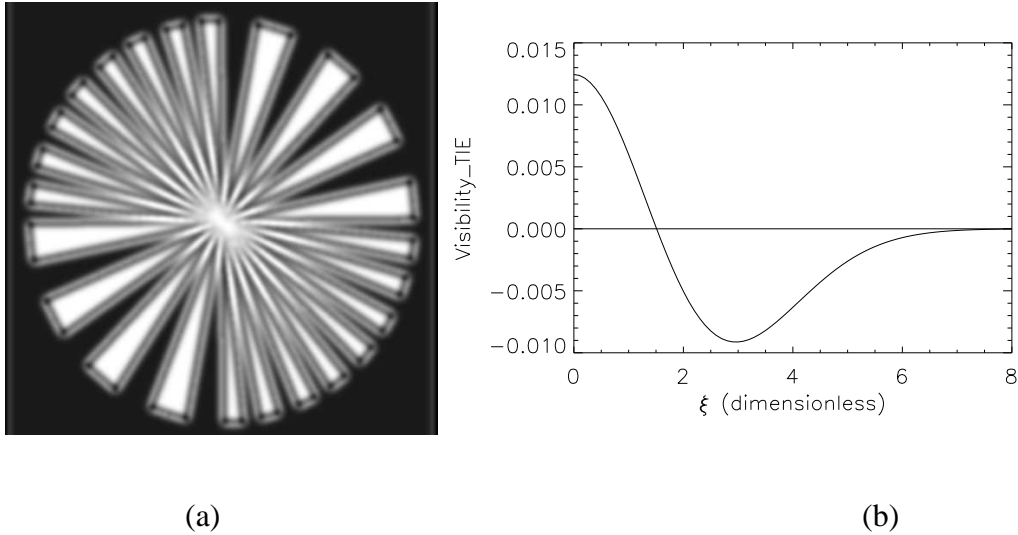


Figure 5.9: (a). Image of the star sample, at $z_1 = 4cm$, $z_2 = 5cm$. (b). The correspond visibility function

the characteristic value of $\sigma_s = 6.79 \times 10^{-6}m$. The star sample is placed at $z_1 = 4cm$ with $z_2 = 5cm$, and the magnification is 2.25. The measured intensity at the detector plane can be seen in Figure 5.9. Measuring from this figure we see that the black-white reverse area happens when the object size period is around $23\mu m$ to $31\mu m$. From the visibility plot in Figure 5.9(b), we see that visibility is zero at $\xi = 1.45$. Based on Equation 4.15 that describes the relation between object size and source size which is also valid for a complex object, we calculate back to the characteristic size of the source which gives a source size with FWHM between $13\mu m$ to $17\mu m$. This compares

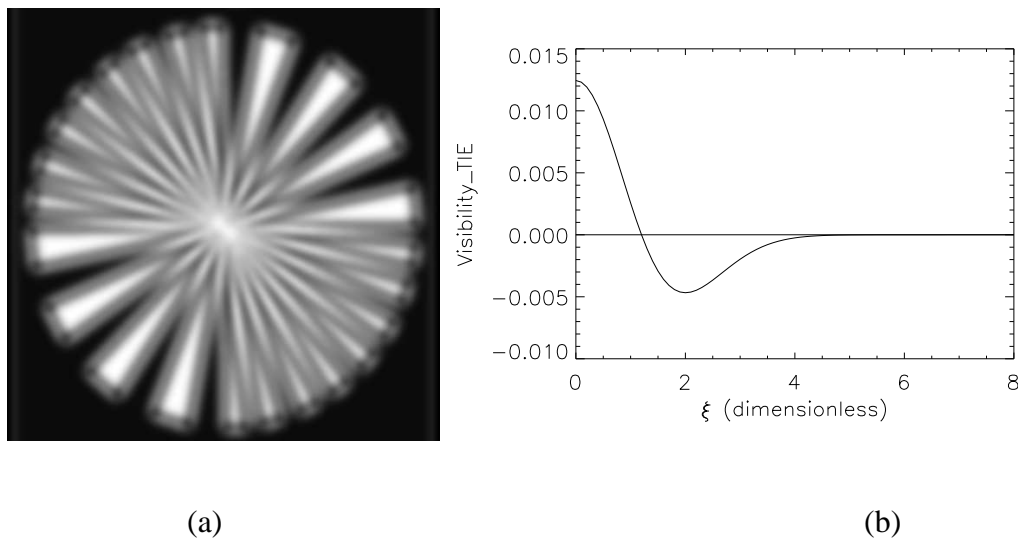


Figure 5.10: (a). Image of the star sample at different distances, $z_1 = 4cm$, $z_2 = 30cm$. (b). The corresponding visibility function.

favorably with the actual source size used to create the intensity at the detector plane.

We can introduce a different set of distances so that $z_1 = 4cm$ and $z_2 = 30cm$, with a magnification of 8.5 times. The calculated intensity can be seen in Figure 5.10. As we expect, source blurring is more detectable for the larger propagation distance. The black-white reverse area happens at a bigger object size period. But in the corresponding visibility plot a smaller value of ξ shows zero visibility. This value leads to the same predicted size for the source. We propose that this technique can be an useful tool for measuring source size.

Optimized radiography contrast: cracks

Another application we explored is to optimize the contrast of a radiograph of a piece of aluminium containing fine cracks (micron size). In this experiment we used a $1mm$ thick aluminium-lithium alloy sheet³ with a $0.3mm$ machined end slot. A fatigue load was imposed, in tearing mode, to produce cracks a few mm long. The optical image of both surfaces of the aluminium sheet can be seen in Figure 5.11. The dark region on the left of the figures is the end slot which is the beginning of the crack growth. The visible crack on the surface on both sides has been measured and is around $20\mu m$ to

³We would like to acknowledge John Thornton (DSTO) for supplying this sample.

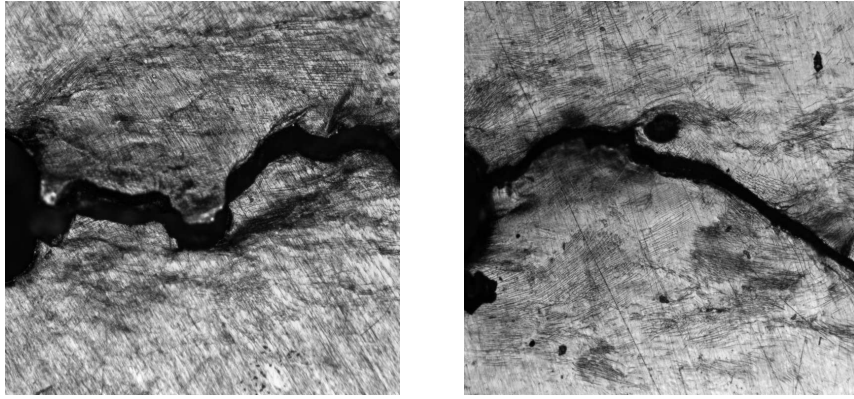


Figure 5.11: Optical microscope image of the cracks in aluminium on both surfaces. The end slot is at the left of the figures.

$40\mu m$ wide along the bulk of its length.

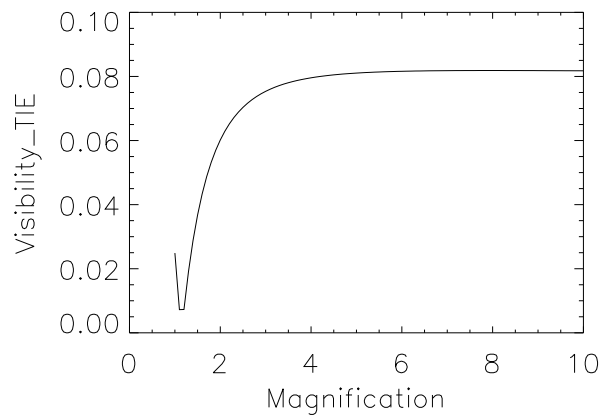


Figure 5.12: Visibility of aluminium as a function of magnification, for a sample period of $30\mu m$, at a source sample distance, $z_1 = 0.2m$.

Next, we plot in Figure 5.12 the visibility as a function of magnification for $10\mu m$ maximum thickness of aluminium for a sample period of $30\mu m$, at source sample distance, $z_1 = 0.2m$ with source FWHM= $14\mu m$. It can be seen that the visibility in the $M = 9$ geometry (phase image, $z_2 = 1.6m$) is around four times higher than for $M = 1$ (absorption image, $z_2 = 0m$). The experiment for optimizing the contrast, was performed with a Fein Focus x-ray tube source with the operating condition of 20 keV,

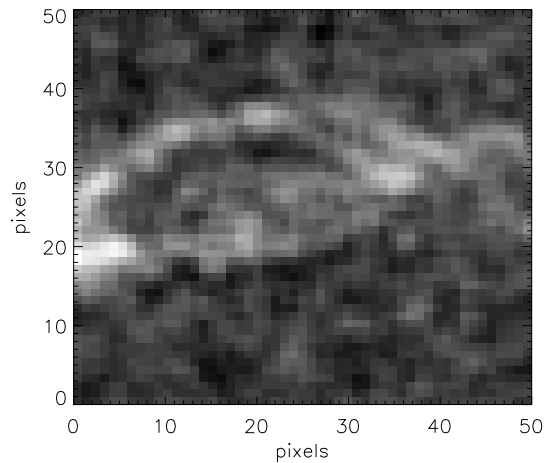


Figure 5.13: Absorption contrast using a CCD detector, $M=1$ geometry.

$400\mu\text{A}$. The measured intensity for absorption contrast, see Figure 5.13, was taken using a Photometrics CH260 CCD camera. The image has been smoothed to reduce the statistical noise and some structure can be discerned. In this case, the resolution of the image is limited by the detector pixel size of $27\mu\text{m}$. In Figure 5.14 an x-ray film has

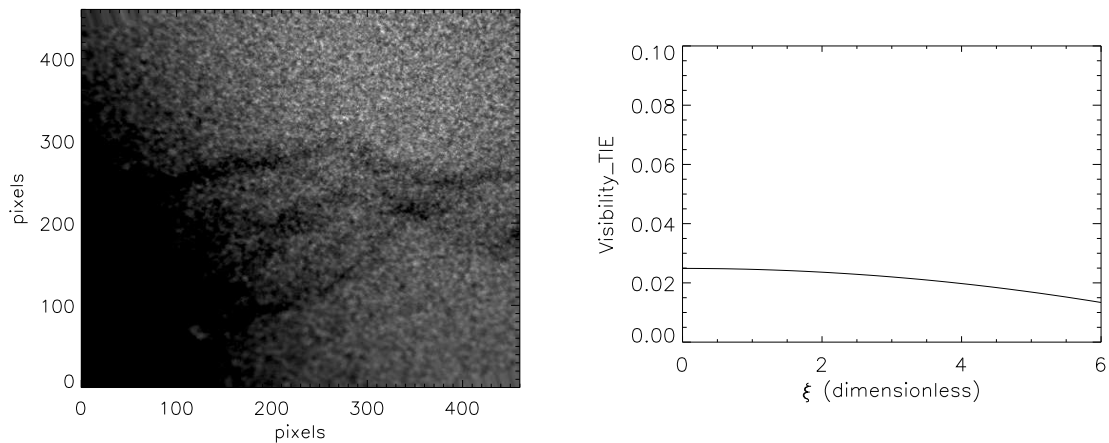


Figure 5.14: Absorption contrast using a film as detector with the correspond visibility function.

been used as the detector in order to show the same absorption image and to achieve resolution that is comparable with the phase contrast image, shown in Figure 5.15. The times 9 magnification of the phase-contrast image configuration should achieve a resolution of $3\mu\text{m}$ if limited by the detector pixel size. However, the resolution of this phase-contrast configuration is actually limited by the source size to $14 \pm 5\mu\text{m}$. The

three images have been scaled so as to have the same field of view.

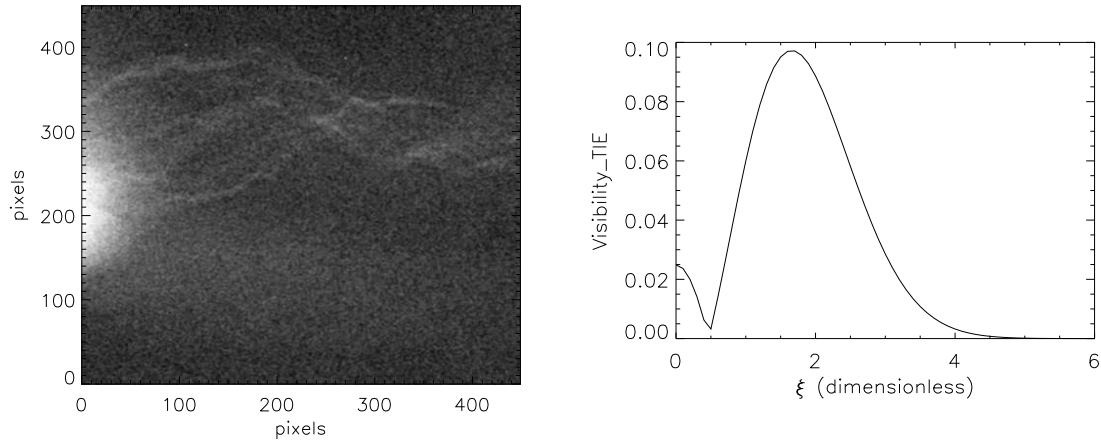


Figure 5.15: Phase contrast image, $M=9$ with the corresponds visibility function.

In the plot of Figure 5.14, we see that absorption contrast can only achieve visibility of around 0.02 for all crack sizes. In the case of the phase contrast image, see Figure 5.15, for which $M = 9$ ($z_1 = 0.2m$, $z_2 = 1.6m$), the crack features are clearly visible and the structure is more detailed. The improved structure is partly due to better resolution arising from higher magnification, but the increased contrast arises from the effects of phase. The phase effect increases the contrast up to 5 times for a $22\mu m$ object period. And increased contrast is obtained for object periods between $12\mu m$ to $55\mu m$.

Optimized radiography contrast: corrosion

Corrosion is a different type of damage in materials. The physical size of corrosion flakes, see Figure 5.16 is much bigger than micro cracks. Micro cracks have micron size while corrosion flakes have millimeter sizescale. Due to their bigger sizes, is it possible to optimize the radiography contrast? According Equation 5.16, if the object period is large or $\xi \rightarrow 0$, the visibility will approach a maximum value of μ_0 and the phase term approaches zero. We will demonstrate this experimentally for the case of corrosion in an aluminium sample ⁴. Corrosion was initiated by spraying salt (Na Cl) mist onto an aluminium alloy plate inside a $35^\circ C$ chamber for 2 - 3 days. The sample was tapered in its thickness, so that the top side of Figure 5.16 is the thinnest part,

⁴We thank to John Thornton for providing the sample.

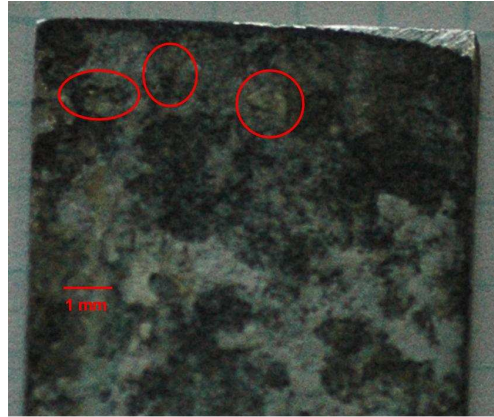


Figure 5.16: Optical image of the corrosion sample. Three circle show the example of the corrosion flakes.

0.35mm thick, and the bottom part is thicker, 0.85mm thick. The sample was made to allow the x-ray beam to easily penetrate through the thinnest part of the aluminium plate.

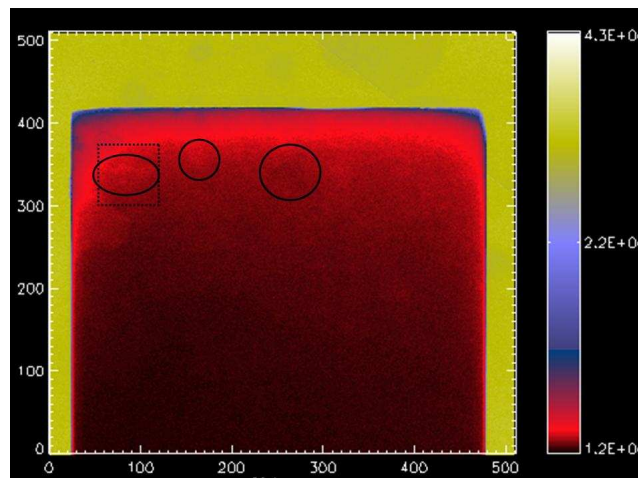


Figure 5.17: Contact image for the corrosion sample, $M = 1$

The same x-ray source, operating condition and detector as for the cracks experiment were used. The contact image is shown in Figure 5.17. Three corrosion flakes in the thinnest part of the sample are visible with limited contrast, while the thicker part of the plate acts to block the x-ray beam. The phase contrast image for which $M = 9$ times ($z_1 = 0.2m$, $z_2 = 1.6m$), is shown in Figure 5.18. The magnified image of the

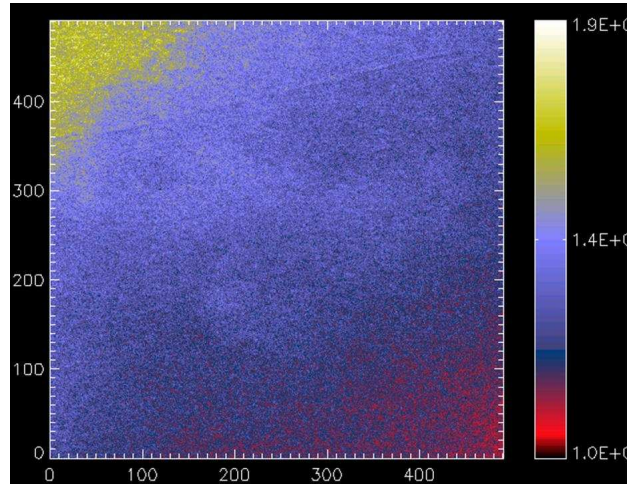


Figure 5.18: Phase contrast image, $M = 9$, for imaging area of a dot square shown on Figure 5.17.

flake in the first circle in Figure 5.17 can be seen. There is no increasing contrast, as we expected.

5.2 Image modelling for long propagation distances

We discuss another image formation model that is valid for larger propagation distances. We call this approach the Contrast Transfer Function (CTF) model. It is based on a more general treatment of x-ray image formation by Fresnel diffraction theory. We rewrite the CTF equation as seen in Equation 2.66 as:

$$\tilde{I}_{coh,z}(\mathbf{u}) = I_0 \left[\delta(\mathbf{u}) - \tilde{\mu}(\mathbf{u}) \cos(\pi\lambda z\mathbf{u}^2) + 2\tilde{\phi}(\mathbf{u}) \sin(\pi\lambda z\mathbf{u}^2) \right] \quad (5.21)$$

In Fourier space, the effect of a partially coherent extended source is equivalent to multiplication of the coherent intensity, $\tilde{I}_{coh,z}(\mathbf{r})$, by the Fourier Transform of the source distribution, $\tilde{\sigma}(\mathbf{u})$. Then, the measured intensity at a distance z becomes:

$$\tilde{I}_z(\mathbf{u}) = I_0 \left[\delta(\mathbf{u}) - \tilde{\mu}(\mathbf{u}) \cos(\pi\lambda z\mathbf{u}^2) + 2\tilde{\phi}(\mathbf{u}) \sin(\pi\lambda z\mathbf{u}^2) \right] \tilde{\sigma}(\mathbf{u}) \quad (5.22)$$

This eliminates spatial frequencies above some cut-off value, corresponding to the width of the source size, see Figure 5.19. This is consistent with the previous discussion in the explanation of Figure 5.1.

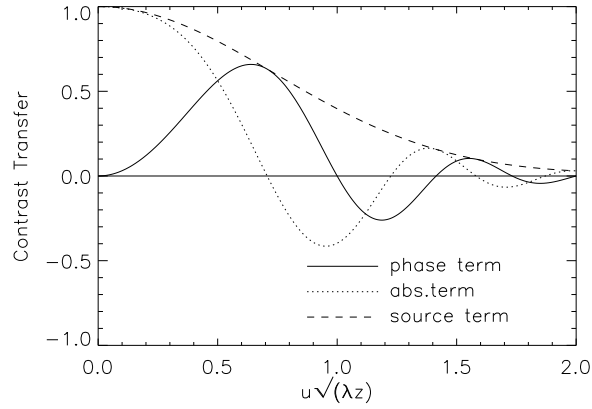


Figure 5.19: Absorption component and phase component in the presence of an incoherent extended source.

We now include the phase shift and the attenuation variation from Equations 5.2 and 5.3, and use the relation $k_s = 2\pi u_s$. The Fourier Transform of the phase shift and attenuation variation becomes:

$$\tilde{\phi}(\mathbf{u}) = \phi_0[\delta(\mathbf{u} - 2\pi\mathbf{u}_s) + \delta(\mathbf{u} + 2\pi\mathbf{u}_s)] \quad (5.23)$$

$$\tilde{\mu}(\mathbf{u}) = \mu_0[\delta(\mathbf{u} - 2\pi\mathbf{u}_s) + \delta(\mathbf{u} + 2\pi\mathbf{u}_s)] \quad (5.24)$$

Now, $\tilde{\phi}(\mathbf{u})$ has a magnitude of ϕ_0 only at frequency \mathbf{u}_s and is zero elsewhere. Similarly, $\tilde{\mu}(\mathbf{u})$ has a value of μ_0 only at frequency \mathbf{u}_s and is zero elsewhere. Substituting into Equation 5.21:

$$\tilde{I}_{coh,z}(\mathbf{u}_s) = I_0 [\delta(\mathbf{u}_s) - \mu_0 \cos(\pi\lambda z \mathbf{u}_s^2) + 2\phi_0 \sin(\pi\lambda z \mathbf{u}_s^2)] \quad (5.25)$$

If we take the Fourier Transform of Equation 5.9 on both sides and apply only for one object frequency \mathbf{u}_s , we find:

$$\tilde{I}(\mathbf{u}_s, z_2) = \frac{1}{M^2} \left[\tilde{I}_{coh}(M\mathbf{u}_s, \frac{z_2}{M}) \tilde{\sigma}((M-1)\mathbf{u}_s) \right] \quad (5.26)$$

In this case we can write $u' = Mu_s$ and $z_2 = Mz$. So, for a small incoherent source, we multiply Equation 5.25 with the Fourier transform of the source intensity distribution,

$\tilde{\sigma}(\mathbf{u}_s)$, and after appropriate scaling we find:

$$\begin{aligned}\tilde{I}(\mathbf{u}', z) &= \frac{I_0}{M^2} [\delta(\mathbf{u}') - \mu_0 \cos(\pi \lambda z \mathbf{u}'^2) + 2\phi_0 \sin(\pi \lambda z \mathbf{u}'^2)] \tilde{\sigma}\left(\frac{M-1}{M}\mathbf{u}'\right) \\ &= \frac{I_0}{M^2} \left[\delta(\mathbf{u}') - \{ \mu_0 \cos(\pi \lambda z \mathbf{u}'^2) - 2\phi_0 \sin(\pi \lambda z \mathbf{u}'^2) \} \tilde{\sigma}\left(\frac{M-1}{M}\mathbf{u}'\right) \right] \quad (5.27)\end{aligned}$$

This gives a simple interpretation in terms of image contrast of the amplitude and phase components of the object transmission function. In this case, we can write Equation 5.27 in terms of the general visibility function based on the CTF method as follows:

$$\frac{\tilde{I}(\mathbf{u}', z)}{I_0} = \frac{1}{M^2} [\delta(\mathbf{u}') - V_{CTF}(\mathbf{u}')] \quad (5.28)$$

$V_{CTF}(\mathbf{u}')$ represents the image contrast due to both the absorption and the phase variation. The visibility as a function of spatial frequency, based on the CTF approximation becomes:

$$V_{CTF}(\mathbf{u}') = [\mu_0 \cos(\pi \lambda z \mathbf{u}'^2) - 2\phi_0 \sin(\pi \lambda z \mathbf{u}'^2)] \tilde{\sigma}\left(\frac{M-1}{M}\mathbf{u}'\right) \quad (5.29)$$

Equation 5.28 is written in the same form as Equation 5.15 but in the frequency domain.

If we take the Fourier transform of Equation 5.15, we get:

$$\begin{aligned}\frac{\tilde{I}(\mathbf{u})}{I_0} &= \frac{1}{M^2} [\delta(\mathbf{u}) - V_{TIE}(\mathbf{u})\delta(\mathbf{u} \pm 2\pi\mathbf{u}')] \\ &\quad \text{or} \\ \frac{\tilde{I}(\mathbf{u}')}{I_0} &= \frac{1}{M^2} [\delta(\mathbf{u}') - V_{TIE}(\mathbf{u}')] \quad (5.30)\end{aligned}$$

The equation is valid only for one frequency, \mathbf{u}' , because of the multiplication by the delta function $\delta(\mathbf{u} \pm 2\pi\mathbf{u}')$. As the spatial frequency term, \mathbf{u}' , only appears in the visibility term as a square then this equation becomes directly comparable to Equation 5.28. The main difference between the two visibility terms then arises from the different approximations made in reaching them: the CTF approximation is valid under the approximations in Equations 2.67, 2.68, 2.69, while the TIE approximation requires $\mu(r) \ll 1$ and short propagation distances for validity. Figure 5.20 shows the function V_{CTF} from Equation 5.29 that consists of the absorption term with amplitude μ_0 and the phase term with amplitude $-2\phi_0$. This is for a $2\mu m$ thick aluminium sample at $z_1 = 2m$, $z_2 = 2m$, FWHM = $10\mu m$. The absorption term becomes less important

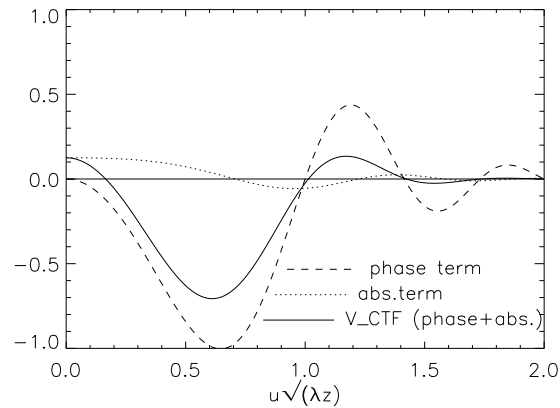


Figure 5.20: Components of visibility function based on CTF method.

for large propagation distances and/or at high spatial frequencies. The absorption term also tends to reduce the visibility from the phase component. Therefore sometimes a pure phase sample becomes a good choice for exploring large propagation distances, for example in experimental work that has been done by Turner et.al. [Tur04a], and by Cloetens et.al. [Clo97b].

5.2.1 Talbot effect

A special characteristic of the imaging model based on the CTF method is that it is valid for large propagation distances. This means that several contrast reversals may be observed. These sequential peaks of contrast are a manifestation of the Talbot effect.

The Talbot effect describes the phenomenon that under spatially coherent, quasi monochromatic plane wave illumination, perfect images of a periodic object are observed if the propagation distance is an integral multiple of the Talbot distance of $z_T = 2a^2/\lambda$, where a is the period of the object [Clo97b]. Talbot images show two types of periodicity; periodicity in spatial frequencies of the object, and periodicity in the direction of propagation distance (Talbot distance).

The requirement of spatial coherence on the beam for Talbot effect implementation can be achieved by placing the sample at a large enough distance, z_1 . It means a high flux beam is necessary, such as at synchrotron sources. The visibility based on the CTF

method for a pure phase sample is given by:

$$V_{CTF}(\mathbf{u}) = 2|\phi_0| \sin(\pi\lambda z\mathbf{u}^2)\tilde{\sigma}\left(\frac{M-1}{M}\mathbf{u}\right) \quad (5.31)$$

The equation shows that zero contrast occurs when $\lambda z\mathbf{u}^2$ is an integer number. So that, for the corresponding frequency $u = 1/a$, zero contrast occurs at repeating propagation distance of:

$$z = \frac{a^2}{\lambda}, \quad 2\frac{a^2}{\lambda}, \quad 3\frac{a^2}{\lambda}, \quad \dots n\frac{a^2}{\lambda} \quad (5.32)$$

where n is an integer.

Zero contrast occurs also in repeating object period of:

$$a = \sqrt{\frac{\lambda z}{1}}, \quad \sqrt{\frac{\lambda z}{2}}, \quad \sqrt{\frac{\lambda z}{3}}, \quad \dots \sqrt{\frac{\lambda z}{n}} \quad (5.33)$$

Figure 5.21 shows a simulated intensity image of a star sample of Kapton ($C_{22}H_{10}N_2O_4$), a pure phase sample, with parameters $z_1 = 1.5m$, $z_2 = 1.5m$, $FWHM = 5\mu m$, $\lambda = 1.1\text{\AA}$, sample thickness = $5\mu m$, sample diameter = $200\mu m$. We see that zero visibility occurs

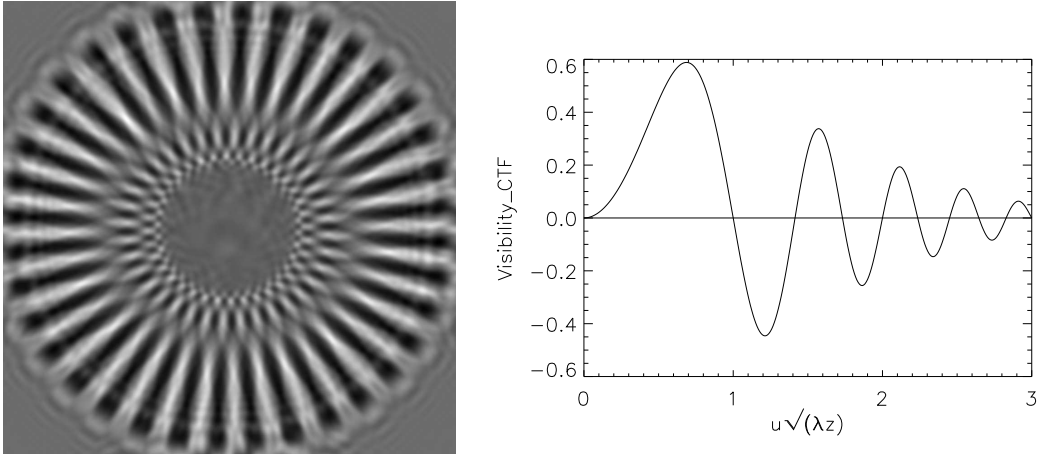


Figure 5.21: Intensity image of a Kapton star sample $5\mu m$ thick, with the corresponds V_{CTF} plot.

several times across the range of spatial frequencies of the object. Zero visibility at this propagation distance indicates clearly that a single Fresnel diffraction pattern can contain no information on certain spatial frequencies. We calculate that zero visibility occurs for object sizes: $9\mu m$, $6.4\mu m$, $5.2\mu m$, $4.5\mu m$ etc. In order to observe this phenomenon the propagation distance must be sufficiently large so that the zero crossings in Figure 5.21 are reached.


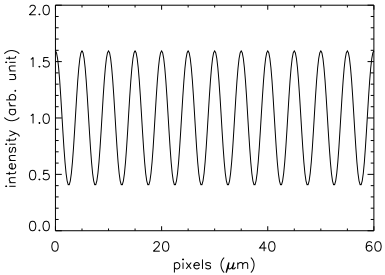

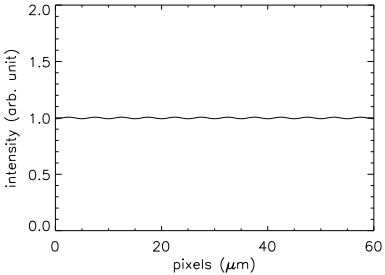

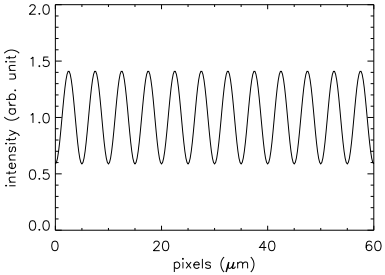

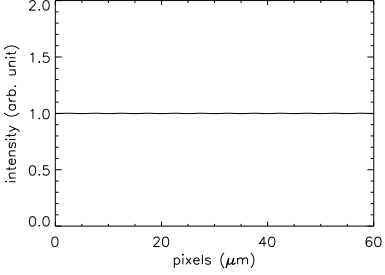

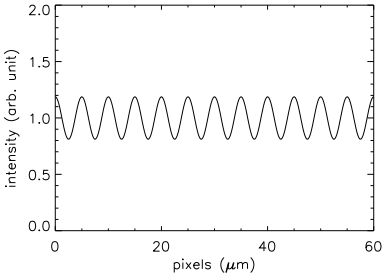
z	contrast	images	intensity profiles
$\frac{1}{2} \frac{a^2}{\lambda}$	1 st max(pos.)		
$\frac{a^2}{\lambda}$	1 st zero		
$\frac{3}{2} \frac{a^2}{\lambda}$	2 nd max (neg.)		
$2 \frac{a^2}{\lambda}$	2 nd zero		
$\frac{5}{2} \frac{a^2}{\lambda}$	3 th max (pos.)		

Table 5.2: Talbot images for a $5\mu\text{m}$ period Kapton grating.

For a highly coherent beam, the damping factor from the finite source size will be small. Consequently, the maxima in contrast will also be repeated with almost the same contrast value. The maximum contrast occurs when $\lambda z \mathbf{u}^2$ is a half odd integer number, that is at repeating propagation distances of:

$$z = \frac{1}{2} \frac{a^2}{\lambda}, \quad \frac{3}{2} \frac{a^2}{\lambda}, \quad \frac{5}{2} \frac{a^2}{\lambda}, \quad \dots \quad \frac{ma^2}{2\lambda} \quad (5.34)$$

where m is an odd number.

Table 5.2 shows images of a $5\mu m$ period Kapton grating with $5\mu m$ thickness, taken at increasing distances, z_2 , keeping $z_1 = 1m$ constant, so that the effective propagation distance, z (according Equation 2.12), is achieved as shown in the first column. FWHM of $5\mu m$ and an x-ray wavelength of $\lambda = 1.1\text{\AA}$ is used. The periodicity in the propagation direction is not perfect in intensity as shown in the intensity profiles in the last column. The decreasing of contrast in the Talbot images is due to the extended source size. It is also observed that the third row has negative contrast compared to the first row, as expected from the CTF.

5.3 Simulation results

In this section we show the comparison between the TIE based method and the CTF based method, in numerical simulations. We use the properties of an aluminium object with a sinusoidal profile at $\lambda = 1.1\text{\AA}$, to represent an object with absorption and phase variation. Variation in the period of the sinusoidal profile has been made for this simulation to represent the spatial frequency variation. The refractive index of aluminium at this energy is $\delta = 4.48 \times 10^{-6}$ and $\beta = 4.42 \times 10^{-8}$. A Gaussian source distribution with FWHM of $10\mu m$ is used. The visibility is then measured using Equation 3.6.

The simulated results are compared with the Visibility based on the TIE method, V_{TIE} , from Equation 5.16 and the Visibility based on the CTF method, V_{CTF} , from Equation 5.29. Figures 5.22 and 5.23 show the visibility in the small propagation regime ($z_1 = 0.1m$ and $z_2 = 1m$), for two different amplitude modulations of $2\mu m$ and $6\mu m$, with $\phi_0 = 0.5$ and $\mu_0 = 0.01$ for the $2\mu m$ amplitude modulation; and $\phi_0 = 1.5$ and $\mu_0 = 0.03$ for the $6\mu m$ amplitude modulation respectively. Each simulation point

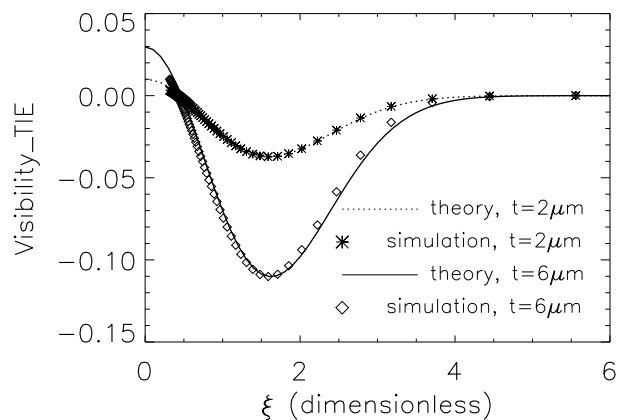


Figure 5.22: Simulation results of aluminium at a small propagation distance ($z_1 = 0.1m$ and $z_2 = 1m$), compared with the theoretical visibility function based on TIE method.

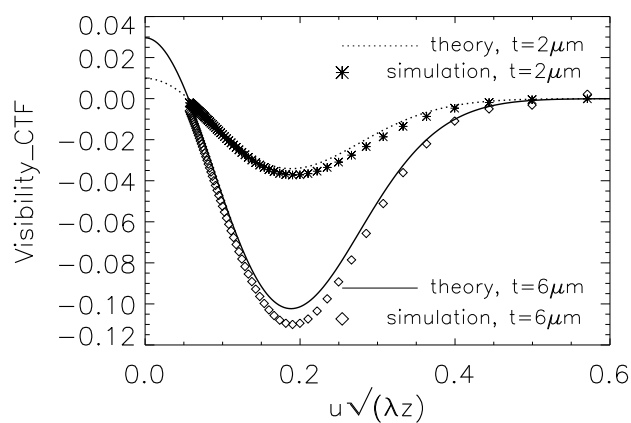


Figure 5.23: Simulation results of aluminium at a small propagation distance ($z_1 = 0.1m$ and $z_2 = 1m$), compared with the theoretical visibility function based on the CTF method.

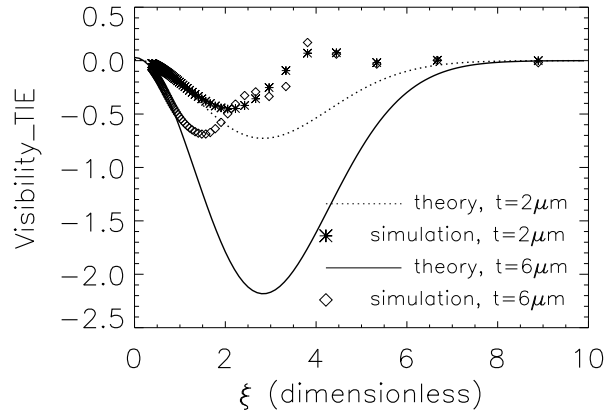


Figure 5.24: Simulation results for aluminium at a large propagation distance ($z_1 = 1m$ and $z_2 = 1m$), compared with the theoretical visibility function based on the TIE method.

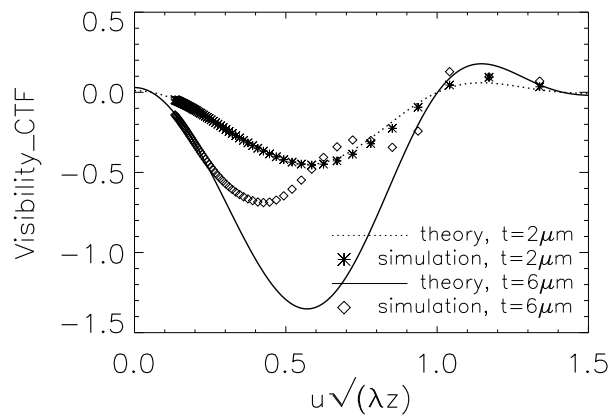


Figure 5.25: Simulation results for aluminium at a large propagation distance ($z_1 = 1m$ and $z_2 = 1m$), compared with the theoretical visibility function based on the CTF method.

represents one spatial frequency of the object. It is shown that the V_{TIE} is a better fit to the simulation results than the V_{CTF} in the small propagation regime.

Figures 5.24 and 5.25 show the visibility in the large propagation regime ($z_1 = 1m$ and $z_2 = 1m$), for two different amplitude modulations of $2\mu m$ and $6\mu m$. It is shown that the V_{CTF} is a better fit in this condition, provided the V_{CTF} approximation in Equations 2.67, 2.68 or 2.69 is satisfied.

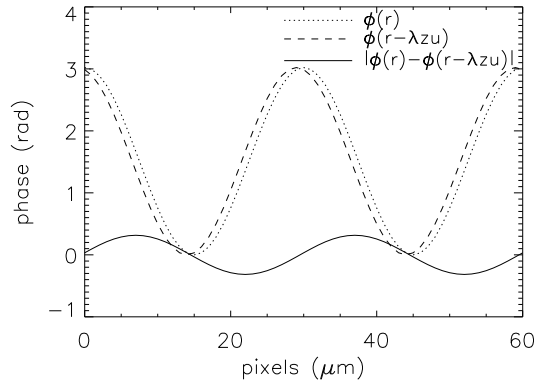


Figure 5.26: The slowly varying phase condition is well satisfied for $30\mu m$ object period.

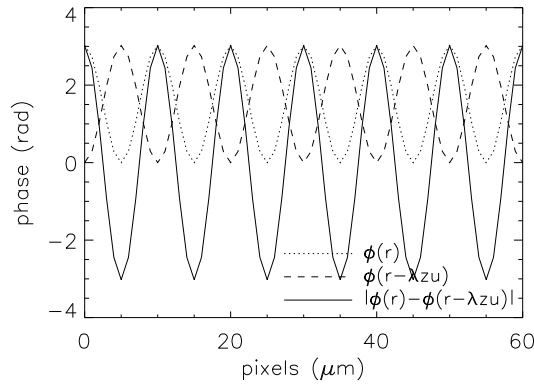


Figure 5.27: The slowly varying phase condition is no longer fulfilled for a $10\mu m$ object period

In Figure 5.25 the theory for the V_{CTF} for the $6\mu m$ amplitude modulation is no longer a good approach for $u\sqrt{\lambda z} > 0.25$, or similarly it is no longer a good approach for object periods smaller than $30\mu m$ under this experimental conditions. As we see

from Equations 2.67, 2.68 or 2.69, the slowly varying phase condition can be rewritten as :

$$|\phi(\mathbf{r}) - \phi(\mathbf{r} - \lambda z \mathbf{u})| \ll 1 \quad (5.35)$$

This means that the phase shift must vary by much less than one radian over a distance $\lambda z u$. For a $30\mu m$ object, the distance $\lambda z u$ is $1.8\mu m$. Figure 5.26 shows the phase after the sample, the phase shift over the equivalent distance of $\lambda z u$ and the phase difference. It is shown that the phase difference is much smaller than one. Thus, for a $30\mu m$ object period, the slowly varying phase condition is satisfied . For a smaller object period, the slowly varying phase condition is no longer fulfilled as is shown in Figure 5.27 for a $10\mu m$ object period, where for our example $\lambda z u$ is $5.5\mu m$.

5.4 Conclusions

We have derived a visibility function for x-ray flux that propagates, under conditions satisfying the TIE solution, from an object with a one dimensional phase and attenuation variation with given feature sizes. This visibility function takes into account the effect of partial coherence from a source due its finite size and to its polychromatic emission. Our results are compared with experimental measurements and excellent agreement is shown. An application of this model using a micro focus x-ray laboratory source convinces us that this model is very useful as a tool for guiding experimental conditions [Tho05]. Our visibility function is then compared with that derived from the contrast transfer function formalism, which is valid under different conditions. It can be seen that a correct application of the two techniques has the potential to cover a broad range of practical applications for x-ray radiography.

Chapter 6

Tomography

The goal of this technique is implicit in its name. Tomo is derived from the Greek word for slice. It is a method for imaging a single slice of a three-dimensional object without superimposing the on the other layers in the object as what happen with the projection imaging technique. For example, in a conventional chest radiograph, the heart, lungs, and ribs are all superimposed on the same film, whereas a computed tomography (CT) captures a slice through each organ in its actual three dimensional position. X-ray tomography started in the 1970's with Hounsfield's invention of the first computed tomography scanner. Dedicated to medical imaging, this device brought a Nobel prize (1979) to its inventor. The required data in x-ray tomography are obtained from transmission measurements whose paths are restricted to lie within the plane of interest and are viewed under a large number of incident angles.

In most tomography work, the reconstruction of the distribution of the imaginary part of the refractive index in the object is obtained from intensity measurements based on absorption. In recent years effort has been made to develop tomographic reconstructions based on phase information. The reconstruction of the full complex refractive index in a slice has been achieved by some groups [Bar00; Bro99; Clo99a; Jon04; McM03b] from amplitude and phase reconstructions. X-ray phase tomography has also been demonstrated at extremely high resolution [McM03a].

In Section 6.1, we begin with a basic review of the tomographic technique. This is followed in Section 6.2 by developing an image formation model for the reconstruction

of a 3D object. We quantify the object reconstruction in terms of a quality function which varies as a function of object frequencies. We define our quality function as a comparison between the reconstruction and the actual distribution of the physical quantity (δ or β) in the object. The effect of an extended source size, such as that in a micro focus x-ray source is also incorporated. This model will be useful for the experimental design of tomography experiments. The model is tested numerically in Section 6.3. The effect of noise on reconstructions will also be discussed. Finally, we show some experimental results in Section 6.4.

6.1 Principle

The principle of tomography is illustrated schematically in Figure 6.1. An x-ray beam passes through a sample and produces a 2D projection of the sample which is recorded on a CCD detector set behind the sample. A number of 2D projection images for different rotations of the sample are combined mathematically to make a sinogram. Then a filtered back projection software is used to re-create a 3D map of the object. Two of the many basic theories for tomography will be explained here: these are Radon transform theory and the Fourier slice theorem.

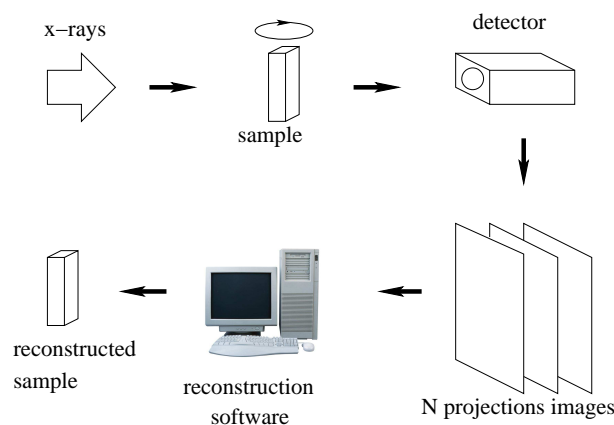


Figure 6.1: Principle of x-ray tomography.

6.1.1 Radon transform theory

Analytically, the measured projection images can be described by a Radon Transform which corresponds to one angular position, θ , of the sample in its rotation axis. The Radon transform is a projection transformation of a two-dimensional function onto polar coordinate space, which transforms lines through an image to points in the Radon domain. The Radon transform of a density distribution $\rho(x, z)$ in each slice for every angular position, is given by [Her79]:

$$P_{\theta}(x_r) = \int \rho(x_r \cos \theta - z_r \sin \theta, x_r \sin \theta + z_r \cos \theta) dz_r \quad (6.1)$$

where the slice is in the $x - z$ plane, and the $x_r - z_r$ plane is the rotated coordinate system under rotation by an angle θ around a rotation axis (y axis here), as shown in Figure 6.2. This equation describes the integral along a line z_r through the image. The x-ray beam

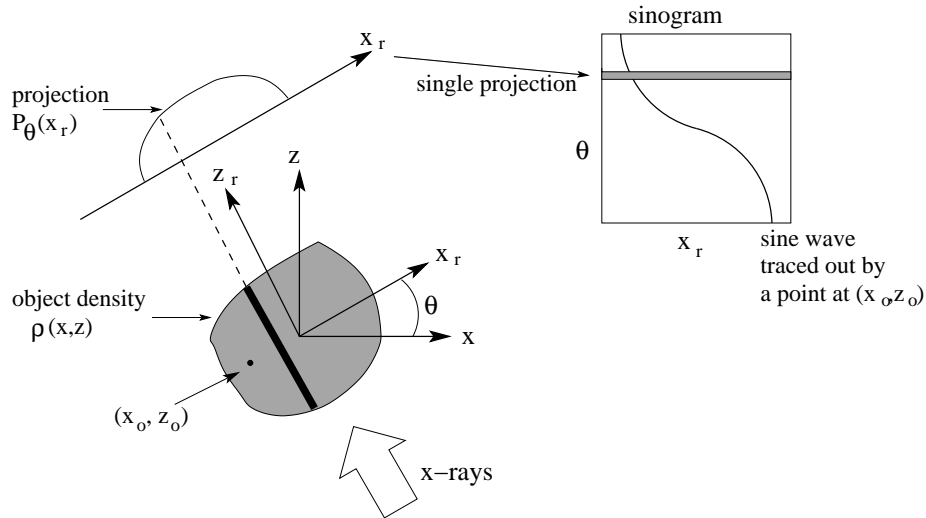


Figure 6.2: Radon transform in each slice.

is parallel to the z_r axis. The function $P_{\theta}(x_r)$ is called a sinogram because the Radon transform of an off-center point object is a sinusoid. The coordinate transformations in this case are:

$$\begin{pmatrix} x \\ z \end{pmatrix} = \begin{pmatrix} \cos \theta & -\sin \theta \\ \sin \theta & \cos \theta \end{pmatrix} \begin{pmatrix} x_r \\ z_r \end{pmatrix} \quad (6.2)$$

and the inverse coordinate transformation is:

$$\begin{pmatrix} x_r \\ z_r \end{pmatrix} = \begin{pmatrix} \cos \theta & \sin \theta \\ -\sin \theta & \cos \theta \end{pmatrix} \begin{pmatrix} x \\ z \end{pmatrix} \quad (6.3)$$

It is sufficient to acquire images over a half turn, because images recorded 180° apart, are each other's mirror image, i.e. $P_\theta(x_r) = P_{\theta+\pi}(-x_r)$ [Bar81].

The distribution of a quantity, such as the object density, is then reconstructed from the projections of many different angles (or the sinogram). This is the inversion of the Radon transform in Equation 6.1 or the back projection operator. Mathematically, the Radon back projection operation is defined as:

$$\rho_{BP}(x, z) = \int_0^\pi P_\theta(x \cos \theta + z \sin \theta) d\theta \quad (6.4)$$

The back projection operation simply propagates the measured sinogram back into the image space along the projection paths, where each point in the Radon domain is transformed to a straight line in the image. In the parallel beam geometry, the slices of the sample corresponding to different heights in the sample can be treated independently. To obtain a complete 3D distribution, one must reconstruct for every value of y . The simple back projection image, $\rho_{BP}(x, z)$, is, however, not exactly the same as the original image, $\rho(x, z)$, but is badly blurred. This is because the back projection operation is not a reversible process of the Radon transform. To be truly reversible this requires the inverse Radon transform associated with an infinite number of projections and an infinite number of zero-width pixels (see discussion at last part of Section 6.1.2).

6.1.2 Fourier slice theorem

The Fourier slice theorem relates the Fourier transform of the object distribution and its projections, as shown in Figure 6.3. The one-dimensional Fourier transform of a single projection corresponds to a single radial line through the center of the frequency image. It follows that enough projections will fill up a complete estimate of the entire frequency domain data. It should then be possible to reconstruct the object by simply performing a two-dimensional inverse Fourier transform [Kak88].

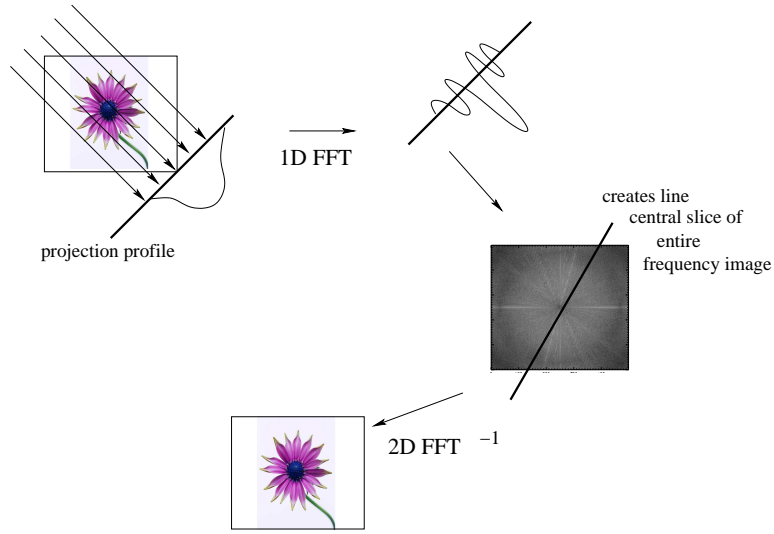


Figure 6.3: Fourier slice theorem

The derivation of the Fourier slice theorem can be written analytically by considering the rotation coordinate as in Equation 6.3. In the rotation coordinate system x_r - z_r , a projection of the object density along lines of constant x_r can be written as:

$$P_\theta(x_r) = \int \rho(x_r, z_r) dz_r \quad (6.5)$$

So, its one-dimensional Fourier transform is given by:

$$\begin{aligned} S_\theta(u) &= \int P_\theta(x_r) e^{i2\pi u x_r} dx_r \\ &= \int \left[\int \rho(x_r, z_r) dz_r \right] e^{i2\pi u x_r} dx_r \end{aligned} \quad (6.6)$$

where the variable u is the frequency. Using the relationships in Equations 6.2 and 6.3, this equation can be transformed into the x - z coordinate system, as:

$$\begin{aligned} S_\theta(u) &= \int \int \rho(x, z) e^{-i2\pi u(x \cos \theta + z \sin \theta)} dx dz \\ &= \int \int \rho(x, z) e^{-i2\pi(u_x x + u_z z)} dx dz \end{aligned} \quad (6.7)$$

The right hand side of the equation represents the two-dimensional Fourier transform at a spatial frequency of $(u_x = u \cos \theta, u_z = u \sin \theta)$. Thus, the one-dimensional Fourier transform of the projections is given by the two-dimensional Fourier transform of the object density.

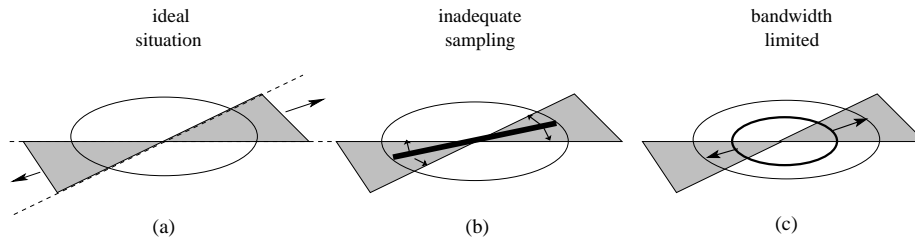


Figure 6.4: Frequency domain data available from one projection (a) ideal situation, (b) and (c) actually measured.

The blurring of the reconstructed object can then be explained according to Figure 6.4. The infinitely long pie-shaped wedge of Figure 6.4(a) is what we want from one single projection. What is actually measured is limited by sampling, Figure 6.4(b), and bandwidth, Figure 6.4(c). High frequency losses due to the bandwidth limitation explains the majority of the blurring in the reconstruction and other artifacts can also arise if sampling is not sufficient.

6.1.3 Filtered back projection

A ramp filter, $h(x)$, defined in frequency space as $H(u) = |u|$ is implemented to correct the blurring problem and the reconstruction of the density, $\rho(x, z)$, is obtained by filtering the projections before back projection [Kak88]. Hence, the reconstruction procedure is called filtered back projection (FBP).

A filter and its frequency response are shown in Figure 6.5. Since the projection data are measured with a sampling interval of τ , the ideal filter (Figure 6.5(b)) has been bandlimited to $1/2\tau$ (Nyquist frequency), and is set to zero outside the frequency interval of $(-\frac{1}{2\tau}, \frac{1}{2\tau})$. The imaging system is then insensitive beyond the Nyquist frequency. The filter itself (Figure 6.5(a)) is given by the function [Kak88]:

$$h(x) = h(n\tau) = \begin{cases} 1/4\tau^2 & n = 0 \\ 0 & n \text{ even} \\ -1/(n\pi\tau)^2 & n \text{ odd} \end{cases} \quad (6.8)$$

where n are positive and negative integers.

A Ramp filter amplifies high frequency so it will tend to enhance high frequency

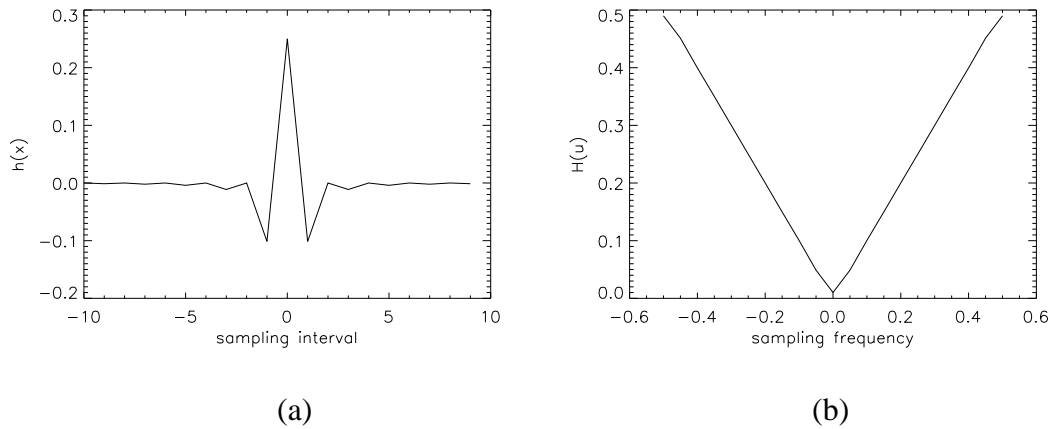


Figure 6.5: (a) Ramp filter and (b) its corresponded frequency response.

noise in real data. Applying a smoothing filter (usually the Shepp-Logan filter, or other low-pass filters such as Hann, Hamming, Ram-Lak, Cosine or others) [Her79] suppresses the high spatial frequencies and tends to reduce noise. Figure 6.6 shows the low-pass filters often used for the filtered back projection algorithm. In this thesis we use the Shepp-Logan filter.

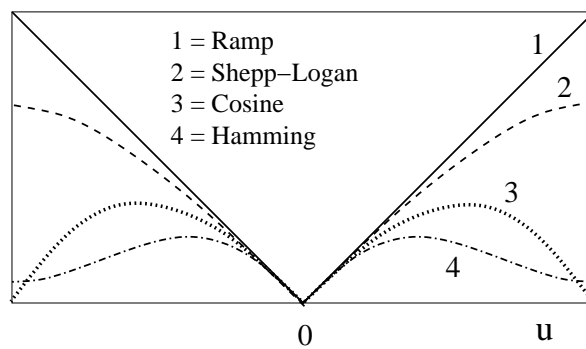


Figure 6.6: Schematic figure of filters that used for the filtered back projection algorithm.

6.2 Extended model for tomography

We consider an ideal transparent object with a one dimensional density variation to represent one spatial frequency in the entire field of view, as shown in Figure 6.7. The

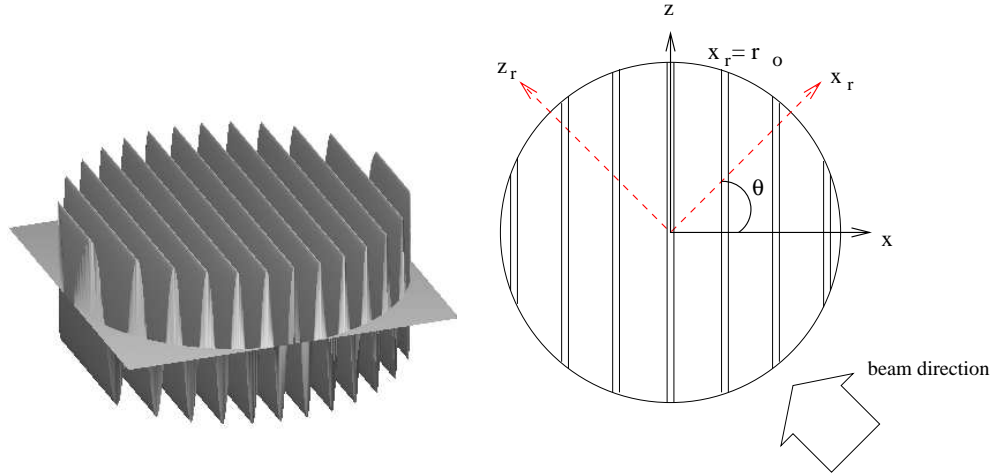


Figure 6.7: Density variation of the object used in the tomography model.

density function is given by:

$$\rho(x) = \begin{cases} \delta \cos(k_s x) & \text{for } x^2 + z^2 \leq r_o^2 \\ 0 & \text{elsewhere} \end{cases} \quad (6.9)$$

where δ is the real part of the refractive index. We place the object in the original coordinate system $x - z$ and rotate the direction of the x-ray beam parallel to the rotated axis z_r as shown in Figure 6.7. Using the rotation matrix in Equation 6.2, we can write the object density in rotated coordinates as:

$$\rho_\theta(x_r) = \delta \cos(k_s x_r \cos \theta - k_s z_r \sin \theta) \quad (6.10)$$

The projection of the object phase at an angle θ is then calculated according to:

$$\begin{aligned} \phi_\theta(x_r) &= -\frac{2\pi}{\lambda} \int_{-\sqrt{r_o^2 - x_r^2}}^{\sqrt{r_o^2 - x_r^2}} \rho_\theta(x_r) dz_r \\ &= -\frac{2\pi}{\lambda} \delta \frac{2}{k_s \sin \theta} \left[\cos(k_s x_r \cos \theta) \sin(k_s \sqrt{r_o^2 - x_r^2} \sin \theta) \right] \end{aligned} \quad (6.11)$$

We then calculate the projection of the object phase using this equation for the whole range of angles between 0° to 180° . The angular step used will determine the resolution of the reconstructed image and the corresponding sampling requirements will be discussed in Section 6.2.1. In the limit $\theta \rightarrow 0^\circ$ the above equation reduces to:

$$\phi_0(x_r) = -\frac{2\pi}{\lambda} 2\sqrt{r_o^2 - x_r^2} \delta \cos(k_s x_r) \quad (6.12)$$

The projections are then "stacked" together into a sinogram. Each sinogram row corresponds to the x-ray projection at one angle as in Equation 6.11. Stacking together each projection for all angle projections from 0° to 180° , we get a complete a 2D sinogram. Figure 6.8 shows the sinogram of the object's phase projection for every angle

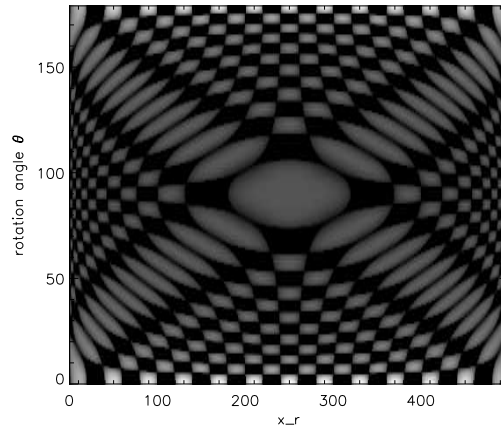


Figure 6.8: Sinogram of the object's phase projection

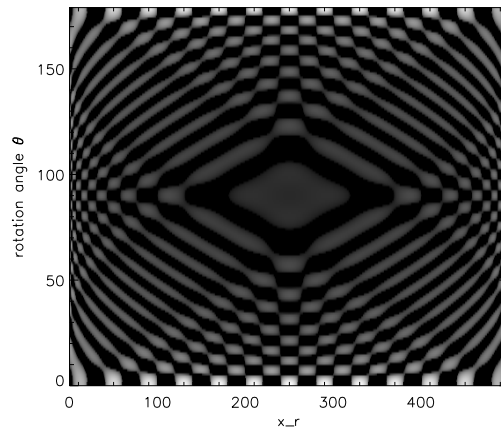


Figure 6.9: Sinogram after Shepp-Logan filtering.

between 0° to 180° . After implementing a Shepp-Logan filter, the filtered sinogram is shown in Figure 6.9. The tomographic reconstruction calculated from each sinogram is a reconstructed 2D image which is a slice through the internal structure of the object. The result of the back projection algorithm from the filtered sinogram is shown in Figure 6.10. This represents a reconstruction of the object density from projections of the

object phase:

$$\rho(x) = FBP[\phi_\theta(x_r)] \quad (6.13)$$

where FBP is the filtered back projection operator. This corresponds to Equation 6.4 applied to the filtered sinogram. The reconstruction result shows the object density of

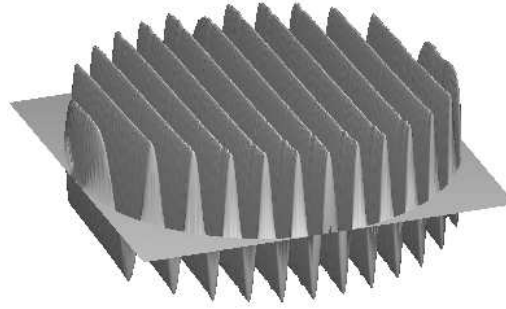


Figure 6.10: Reconstruction of the object density.

$\delta \cos(k_s x)$ through the origin along the x -axis inside the circle with radius r_o .

In classical tomography (absorption tomography), the contrast in the 2D projection arises from the distribution of attenuation in the material. When the attenuation in the material is weak, then phase contrast tomography can provide reconstructed images with improved contrast [McM03a]. The experimental setup for phase contrast tomography is similar to the absorption mode, only the detector is located further away from the object, as shown in Figure 6.11.

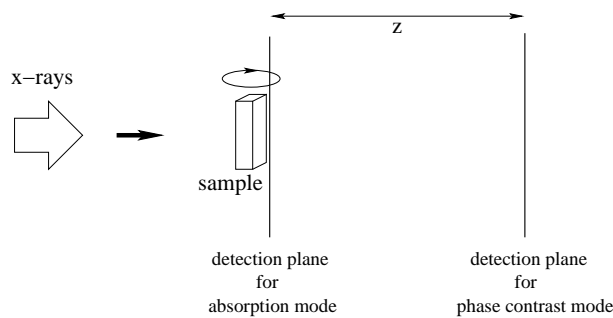


Figure 6.11: Absorption and phase contrast tomography setup.

In an ideal coherent plane wave, the object density of a transparent sample is reconstructed according to the flowchart shown in Figure 6.12. A transparent sample

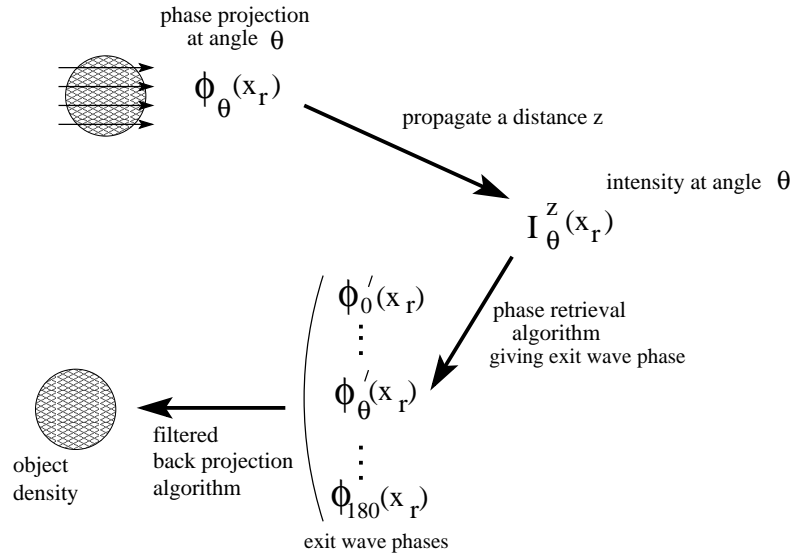


Figure 6.12: Flowchart for tomography reconstruction of a transparent sample using a coherent source.

influences only the phase of the beam on the objects. The phase projection of the sample for every rotation angle is written as $\phi_{\theta}(x_r)$. The wave function transmitted through the sample is observed at the measurement plane placed at a distance z from the sample. We denote the intensity at certain angle θ at the measurement plane as $I_{\theta}^z(x_r)$. These intensities are inverted to retrieve the exit wave phase distribution. There are a number of ways in which the phase may be retrieved as we discussed in Section 2.4.2. The methods chosen often depend on the imaging regime where the projection data have been acquired. The phase at a certain angle, $\phi'_{\theta}(x_r)$, is then retrieved from intensity using the phase retrieval algorithm. When the phase retrieval algorithms used here such as the Transport of Intensity Equation [Nug96], single plane TIE based algorithm [Pag02] and the single plane CTF based algorithm [Tur04a] are implemented correctly, the original phase projection at every angle is retrieved. Having completed acquisition of the phase data from 0° to 180° , we can use the filtered back projection algorithm to reconstruct the object density.

Using an extended and spatially incoherent source, the object density of a trans-

parent sample is also reconstructed according to the flowchart shown in Figure 6.12. However, in this case, the measured intensity at every projection angle can be treated

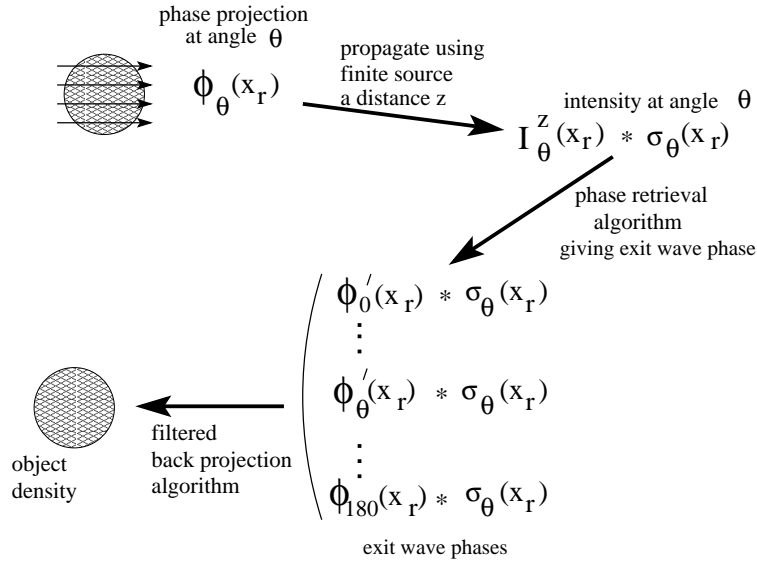


Figure 6.13: Flowchart for tomography reconstruction of a transparent sample using an extended and spatially incoherent source.

as a simple convolution result with the projection of the source intensity distribution $\sigma_\theta(x_r)$ (and including appropriate scaling if a point source is used in projection to provide a magnification factor), as shown in Figure 6.13. We follow here the approach of Paganin [[Pag99] pp. 196-198], where the retrieved phase can be treated as the convolution with the same source projection of $\sigma_\theta(x_r)$ under certain conditions. These conditions will be met in the case of the single plane phase retrieval algorithms.

After correctly implementing the phase retrieval algorithm, the reconstructed density can be written as:

$$\rho_{rec}(x) = FBP [\phi_\theta(x_r) * \sigma_\theta(x_r)] \quad (6.14)$$

According to Natterer [Nat86], the above equation can be written as:

$$\rho_{rec}(x) = FBP [\phi_\theta(x_r)] * \sigma(x) \quad (6.15)$$

We know from Equation 6.13 that the $FBP [\phi_\theta(x_r)]$ inside the circle with radius r_o is $\delta \cos(k_s x)$. Taking into account the magnification factor due to point projection, the

above equation can be rewritten as:

$$\rho_{rec}(x) = \int \delta \cos(k_s \frac{x'}{M}) \cdot \sigma(\frac{x-x'}{M-1}) dx' \quad (6.16)$$

In order to be explicit, a Gaussian distribution is used as a model for the finite source distribution, $\sigma(x)$, as shown in Equation 4.2. We can now rewrite the above equation as:

$$\rho_{rec}(x) = \delta \cos(k_s \frac{x}{M}) \left[\exp(-\frac{1}{2}(\frac{M-1}{M})^2 k_s^2 \sigma_s^2) \right] \quad (6.17)$$

Applying the dimensionless variable from Equation 4.15 as the number of resolution elements contained in the source, we get:

$$\rho_{rec}(x) = \delta \cos(k_s \frac{x}{M}) \left[\exp(-\frac{1}{2}(\frac{M-1}{M})^2 \xi^2) \right] \quad (6.18)$$

We introduce the definition of the quality of the tomographic reconstruction as a division of the reconstructed density by the real density as:

$$Q(\xi, M) = \frac{\rho_{rec}(x)}{\rho(x)} \quad (6.19)$$

Then we can see that the quality function for tomographic reconstructions for a transparent sample as a function of object frequency, ξ , and magnification, M , is:

$$Q(\xi, M) = \exp(-\frac{1}{2}(\frac{M-1}{M})^2 \xi^2) \quad (6.20)$$

Figure 6.14 shows this quality function for a transparent object. At high magnification, the exponential term of Equation 6.20 will be independent of the magnification. The quality function describes then the effect of source blurring and shows the reduction of the quality at higher spatial frequencies. However, for $M \rightarrow 1$ the quality will be perfect for the whole range frequencies. Under this condition significant quality can be observed for structures that are smaller than the source size. Of course, as usual, in such cases detector resolution will become important and in practice will limit the observation of high spatial frequencies.

A similar derivation will now be described for a two dimensional density variation, as shown in Figure 6.15, with the density function given by:

$$\rho(x, z) = \begin{cases} \delta \cos(k_x x) \cos(k_z z) & \text{for } x^2 + z^2 \leq r_o^2 \\ 0 & \text{elsewhere} \end{cases} \quad (6.21)$$

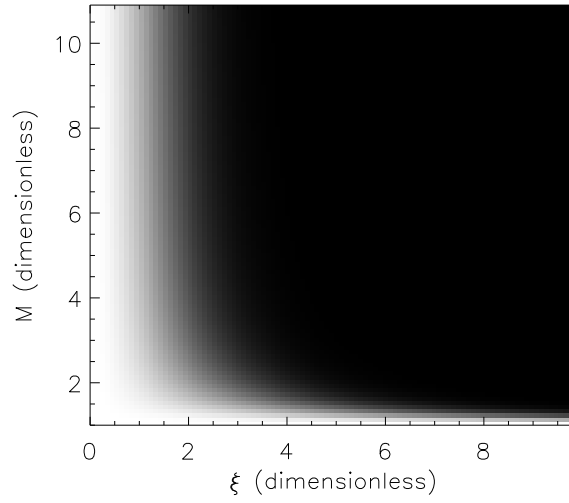


Figure 6.14: The quality function for tomographic reconstruction as a function of dimensionless spatial frequency, ξ , and Magnification, M . The color map is [white = 1, black = 0].

where (k_x, k_z) is the object variation in x and z direction respectively. Most real objects, have a two dimensional density variation rather than one dimensional density variation. For the two dimensional density variation case, Equation 6.15 will have the form:

$$\rho_{rec}(x, z) = FBP[\phi_\theta(x_r)] * \sigma(x, z) \quad (6.22)$$

Evaluating this equation as before and assuming that the source distribution is separable in x and z directions, we have:

$$\rho_{rec}(x, z) = \int \delta \cos(k_x \frac{x'}{M}) \cos(k_z \frac{z'}{M}) \cdot \sigma(\frac{x-x'}{M-1}) \cdot \sigma(\frac{z-z'}{M-1}) dx' dz' \quad (6.23)$$

and when the Gaussian source distribution is included:

$$\rho_{rec}(x, z) = \delta \cos(k_x \frac{x}{M}) \cos(k_z \frac{z}{M}) \left[\exp\left(-\frac{1}{2} \left(\frac{M-1}{M}\right)^2 (\xi_x^2 + \xi_z^2)\right) \right] \quad (6.24)$$

where (ξ_x, ξ_z) is the dimensionless characteristic spatial frequency in the x and z direction respectively. The quality function is then:

$$Q_{round}(\xi, M) = \exp\left(-\frac{1}{2} \left(\frac{M-1}{M}\right)^2 (\xi_x^2 + \xi_z^2)\right) \quad (6.25)$$

In the case when $k_x = k_z$ the quality function become:

$$Q_{round}(\xi, M) = \exp\left(-\left(\frac{M-1}{M}\right)^2 \xi^2\right) \quad (6.26)$$

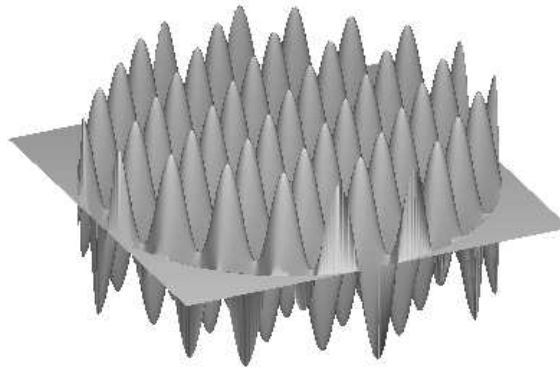


Figure 6.15: Two dimensional density variation in an object.

Note that reduction of the quality function for a 2D structure due to an extended source decreases more quickly than for the 1D case. Consequently, the effect for high spatial frequencies will be larger.

6.2.1 Sampling requirements

In a tomography experiment, a general rule for the number of projections, n_p , required to give reconstruction resolution equal to the detector pixel size is about $\pi/2$ times the number of pixels in the detector [Clo99b]. The choice of n_p determines the angle between projections and therefore the spatial resolution of the reconstructed image, as shown in Figure 6.16. If we acquire images over a half turn of π , then the angle θ between each projections is:

$$\theta = \frac{\pi}{n_p} = \frac{\pi}{\frac{\pi}{2}N_d} = \frac{2}{N_d} \quad (6.27)$$

where N_d is the number of pixels in the detector. The resolution of the reconstructions is therefore given by:

$$\Delta_{rec} = \frac{1}{2}N_d\Delta p. \sin \theta \quad (6.28)$$

where Δp is the detector pixel size. Consequently, in the case when the number of projections, n_p is $(\pi/2).N_d$, the resolution of the reconstructed image will be as good as the detector pixel size itself. When the number of projections is less than $(\pi/2).N_d$, the

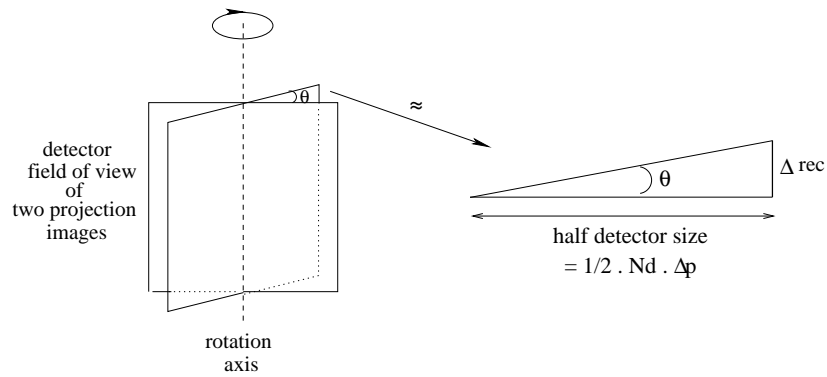


Figure 6.16: Relation between the number of projections with the spatial resolution of the reconstruction.

resolution element in the reconstruction will be larger than the detector pixel size. When a large number of projections is to be performed, there is also the practical limitation of the available hardware for the machine used for the reconstruction, for example the limits of the memory in the hardware.

Poor pixel resolution can be obviated to some degree by using point projection magnification. This was demonstrated by McMahan et al [McM03a] for imaging a $9\mu m$ AFM tip with a $900nm$ bump. A spatial resolution of better than $900nm$ was achieved using a focal beam waist of $60nm$ from a zone plate and magnification of around 160 times, while the nominal detector pixel size was $24.5\mu m$. In these cases though the analysis of Chapter 4 shows that the source to sample distance must become small. For example McMahan et al. used a distance of $6mm$ for source sample distance and $971mm$ for source detector distance.

6.3 Numerical simulation

To evaluate the theory, we modeled a numerical simulation of a phase object. Figure 6.17 shows a slice of round samples with various spatial frequencies. The periods of the samples were $5, 10, 17$ and $38\mu m$ in an array. Each sample was characterized by the real refractive index value of $\delta = 2 \cdot 10^{-6}$. First, the function ϕ_θ was computed by making a projection for every θ at an angular step size of 0.3° . This produces 600

projections over a half turn of 180° . Then, the phase contrast data were computed by applying the Kirchhoff propagator algorithm of Equation 2.26 modified for the spherical wave illumination case at a propagation distance of $z_1 = 0.1m$, $z_2 = 1.7m$ with a magnification factor of 18 times. We assumed in this example that the sample is transparent

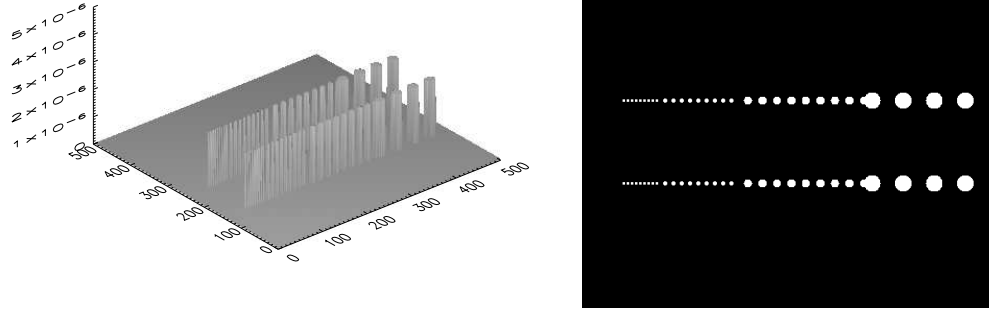


Figure 6.17: Object density function used in the numerical simulation, with period of 5, 10, 17 and $38\mu m$.

($\mu = 0$). The intensity in the measurement plane for every angle was convolved with an extended source with FWHM of $5\mu m$. The x-ray wavelength was $\lambda = 1\text{\AA}$, whereas the detector pixel size was $\Delta p = 1\mu m$ and the number of pixels were 500×500 .

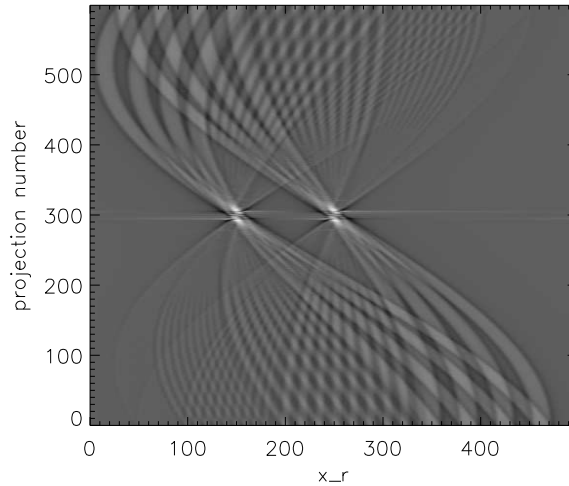


Figure 6.18: Sinogram of the retrieved phase ($\phi'_\theta * \sigma_\theta$) for every projection.

Then, we performed a phase retrieval algorithm for each intensity measurement. In

this example we used the single plane TIE based phase retrieval algorithm of Equation 2.61. The retrieved phase for every projection angle ($\phi'_\theta * \sigma_\theta$) is shown in Figure 6.18 in the form of a sinogram.

The filtered back projection algorithm Equation 6.13 was applied to this sinogram

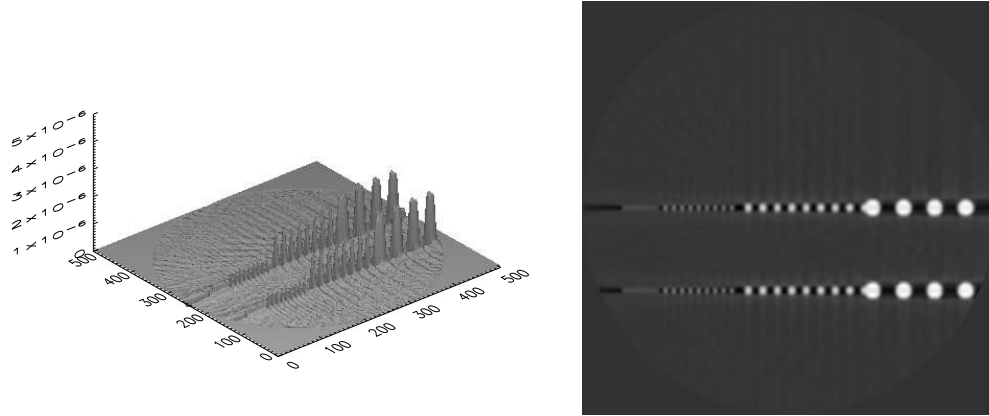


Figure 6.19: The reconstruction of the object density.

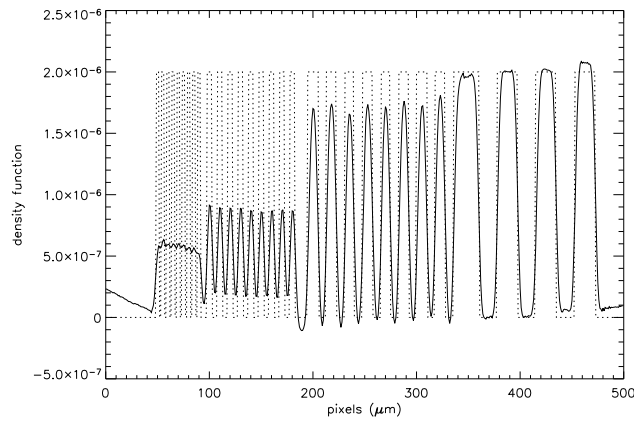


Figure 6.20: Object density profiles along the x-axis direction through the center of the object array. The real object (dot line) and reconstructed object (solid line) shows the same periodicity.

to reconstruct the object density. The reconstruction result is shown in Figure 6.19. To make a more quantitative comparison, we take the profiles of the object density and the reconstructed object along the line going through the center of the array in the x-axis direction. The profiles in Figure 6.20 show that for low spatial frequencies

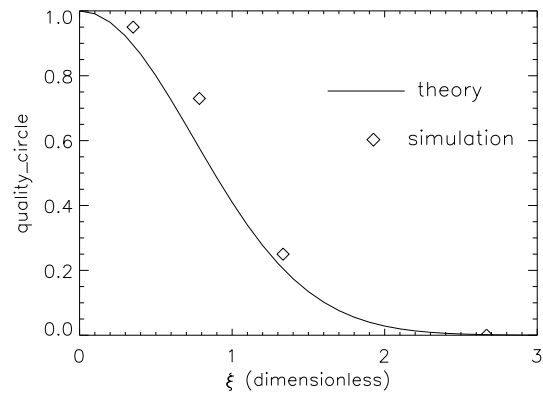


Figure 6.21: Theoretical quality function is plotted against the simulation results, with $z_1 = 0.1m$, $z_2 = 1.7m$.

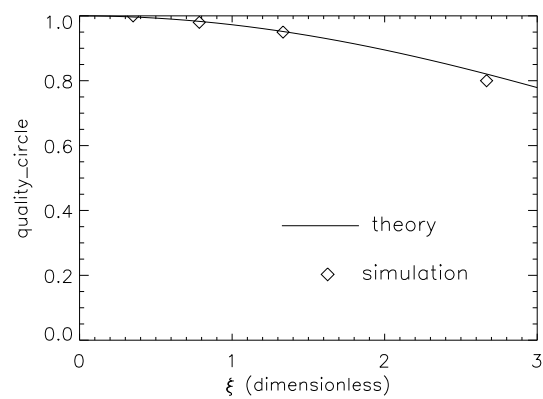


Figure 6.22: Theoretical quality function is plotted against the simulation results, with $z_1 = 0.1m$, $z_2 = 0.02m$.

the object density is well reconstructed with the same periodicity as the input. For higher spatial frequencies the quality of the reconstruction reduces as expected. It is also noticeable that the edges roll off due to the loss of high spatial frequency information. Tomographic artefacts due to inadequate angular sampling and the effect of using a Shepp-Logan filter instead of the ideal Ramp filter will also produce similar round off in the reconstructed features. It would be a worthwhile area of further investigation to disentangle these effects.

We calculated the quality based on the comparison of the reconstructed with the real object density as shown in Equation 6.19. The plot in Figure 6.21 shows the quality function for the reconstruction from Equation 6.26 against the simulation result for the various object frequencies. We see that the source size of $5\mu m$ FWHM becomes a limiting factor for the quality. In this case, an object spatial frequency of $5\mu m$ is reconstructed poorly.

Figure 6.22 shows another simulation result for distances of $z_1 = 0.1m$, $z_2 = 0.02m$, with $M = 1.2$. The same variation in object periods of 38, 17, 10, $5\mu m$ was used. The figure shows that high spatial frequencies are reconstructed with better quality. In this case a theoretical resolution of around $1.6\mu m$ based on Equation 6.28 will be the limit for a viable reconstruction. At this point the limitation is due to the sampling used as given by Equation 6.28.

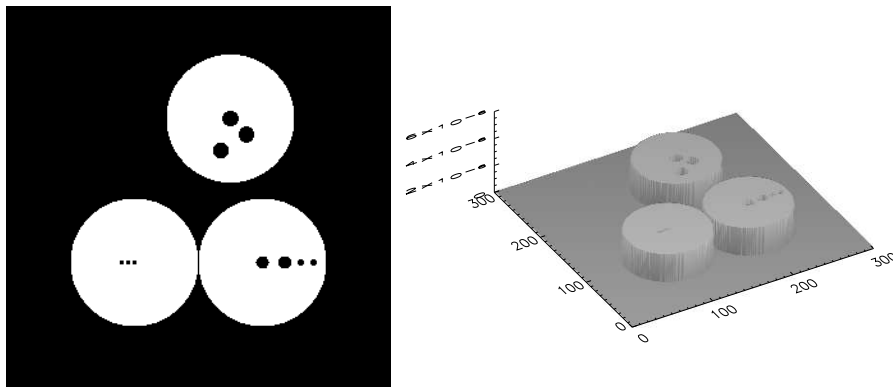


Figure 6.23: Kapton ball sample with voids in one slice.

When quantitative phase retrieval is not applied it has been a common practice to perform the tomographic reconstruction directly from the intensity measurement

[Clo97a; May03]. We applied this technique to a simulation of kapton balls with voids in one slice of the sample, as shown in Figure 6.23. The resulting reconstruction can be seen in Figure 6.24(a). The reconstruction shows a qualitative resemblance to the real object but artefacts can clearly be seen. These are due to the strong edge enhancement seen in the phase contrast images. The effect is similar to what would be observed for a poor signal to noise data set resulting in something that looks like a noisy reconstruction. The result does however show that, where only identification of strong boundary-like features is required, the technique may be used as a qualitative tool. Therefore, Cloetens et al [Clo97a] used this kind of tomographic reconstruction technique for detecting microstructure damage such as cracks in materials.

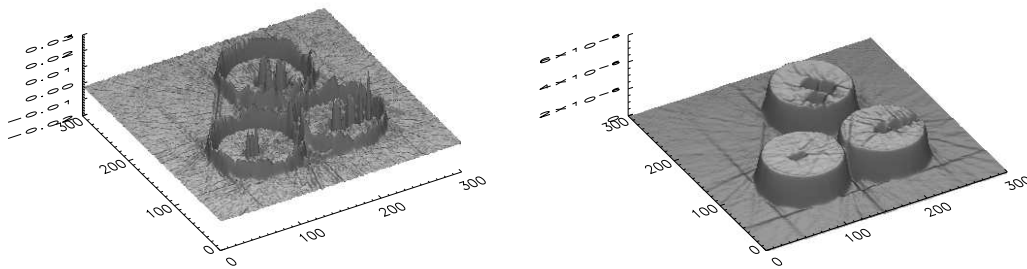


Figure 6.24: Tomography reconstruction (a) from intensity measurement directly (b) after applying phase retrieval.

6.3.1 Effect of noise

As we discussed in Subsection 4.4.1, phase retrieval techniques are more sensitive to noise for small propagation distances. Therefore increasing z_2 will reduce the effect of noise. The same effect applies for phase tomography reconstructions since we apply a phase retrieval technique on the way to reconstructing the object density. Figures 6.25 and 6.26 show the reconstruction of the object density in the presence of 8% noise in the detector plane for the object shown in Figure 6.17. The simulation results were obtained with distances $z_1 = 0.1m$, $z_2 = 0.02m$ with $M = 1.2$ and for $z_1 = 0.1m$,

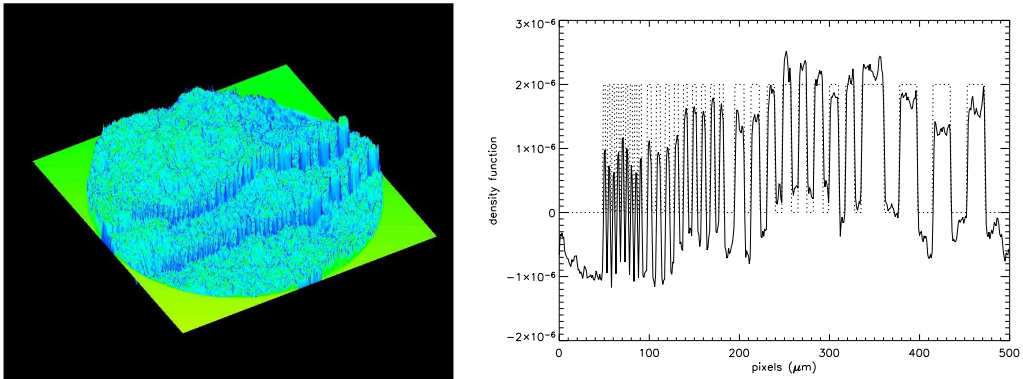


Figure 6.25: Tomography reconstruction for small propagation distance data for the object in Figure 6.17 in the presence of 8% noise with the corresponding plot along one of the lines of the objects.

$z_2 = 1.7m$ with $M = 18$ respectively. Noise was added in the raw intensity data in the same manner as described in Subsection 4.4.1. We see that the result is more sensitive to noise for the small propagation distance.

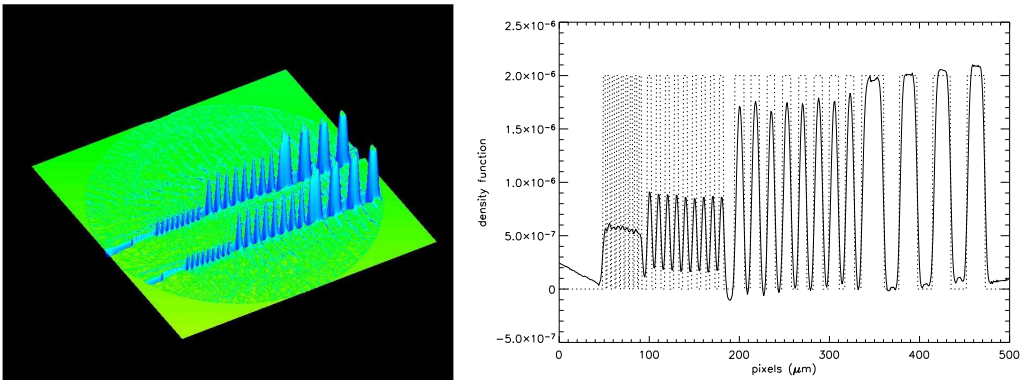


Figure 6.26: Tomography reconstruction for large propagation distance data for the object in Figure 6.17 in the presence of 8% noise with the corresponding plot along one of the lines of the objects.

However, from Figures 6.21 and 6.22, we know that high spatial frequencies are reconstructed better for small propagation distances. Therefore to reduce the problem of noise and to reconstruct better for high spatial frequencies, we apply the objective filtering strategy of Equations 4.22 and 4.23 to the phase images before reconstruction.

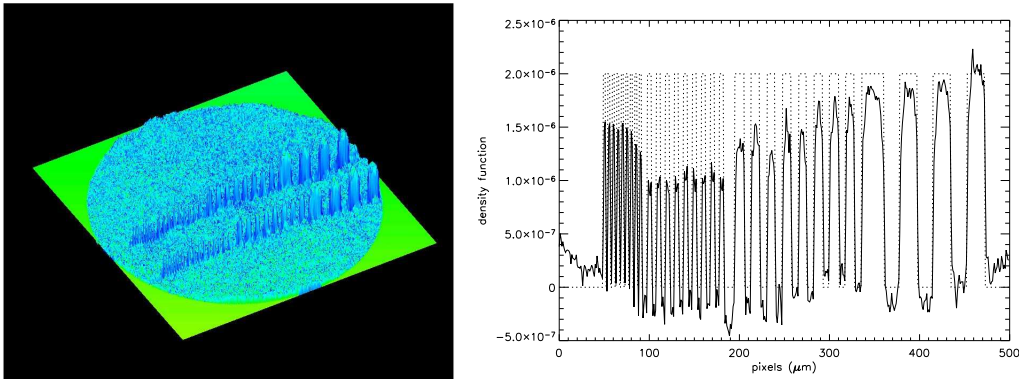


Figure 6.27: Tomography reconstruction for the object in Figure 6.17 after applying an objective filtering strategy in the presence of 8% noise with the corresponding plot along one of the lines of the objects.

Quantitative improvement of the reconstruction when considering the combined images is apparent in Figure 6.27.

6.4 Experiment results

In this section we present some preliminary experiment results¹. These make use of access to a tomography facility in experiments that were performed at beam line 2BM (bending magnet) at the Advanced Photon Source (APS) in Argonne National Laboratory. This facility does not employ focusing optics so all configurations are for the case $M \approx 1$. Nevertheless they allow us to test our model for different object sizes. We describe below the experimental setup and then the results of three experimental arrangements. A monochromatic beam with energy of 7, 10 and 15 keV was used. The samples were polystyrene micro-spheres of different diameters. The samples were mounted on a precision stage with rotation about the vertical axis. The x-ray beam that passed through samples was propagated some distance downstream to a detector. The detector is coupled via an objective lens with an approximately $300\mu\text{m}$ thick cadmium tungstate (CdWO_4) scintillator screen, giving an effective pixel size that depends on the objective used. In the experiment described here a $10\times$ objective was used in such a

¹I would like to acknowledge Dr. Andrew G. Peele who acquired this tomography data.

way as to give an effective pixel size of $0.735 \times 0.735 \mu\text{m}^2$.

Each projection was taken in 0.25° steps, for a half turn between 0° to 180° . Each projection intensity image was corrected for dark current and non uniform illumination of the intensity as described in Equation 3.3. A completed tomography data set was collected in tens of minutes because of the combination of the high brilliance x-ray source and the fast detector readout systems. Preprocessing and phase reconstruction calculations were performed offline on a PC and we reconstruct only a region of interest in the data sets.

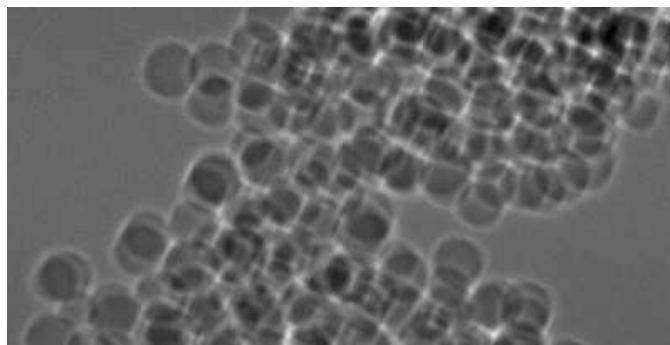


Figure 6.28: Phase contrast image of one projection of polystyrene balls with $20\mu\text{m}$ diameter.

Figure 6.28 shows the phase contrast image for one projection of polystyrene balls with $20\mu\text{m}$ diameter in a small region of 400×200 pixels after applying the intensity correction. An energy of 10 keV was used with a propagation distance of 30mm downstream to the detector. The image shows that the micro-spheres are stacked together and that edge enhancement is clearly visible.

Figure 6.29(a) shows a 3D visualization of the $200 \times 200 \times 200$ voxels² for the tomographic reconstruction based on the measured projections for the $20\mu\text{m}$ diameter polystyrene balls. Figure 6.29(b) shows one slice of 650×650 pixels through the reconstructed volume. This reconstruction was made using the raw phase contrast intensity images without any post-processing or phase retrieval. The reconstructed section clearly shows the main features of the object. It also shows features such as bright fringes around the edges of the object arising from the phase contrast features of the

²Voxel is the three dimensional unit of pixel.

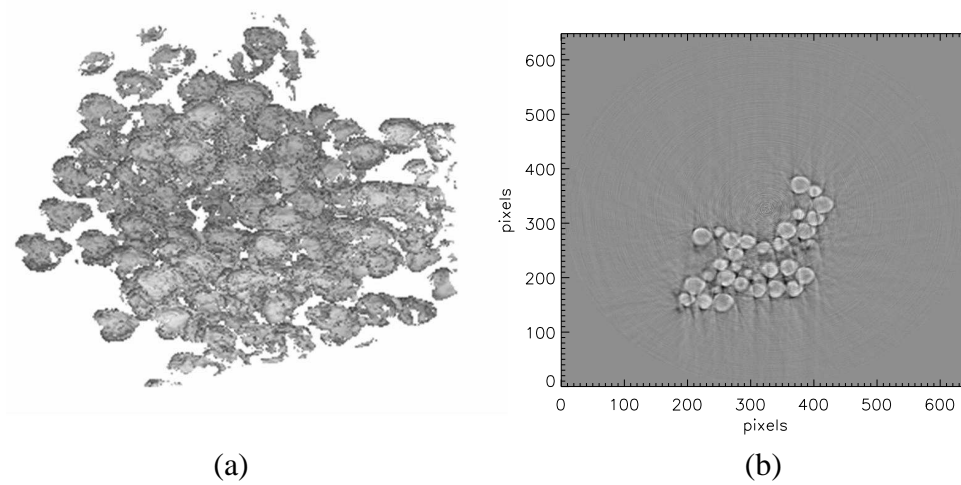


Figure 6.29: A surface rendering of a qualitative 3D reconstruction of the $20\mu\text{m}$ diameter polystyrene balls with the corresponding view of a single slice.

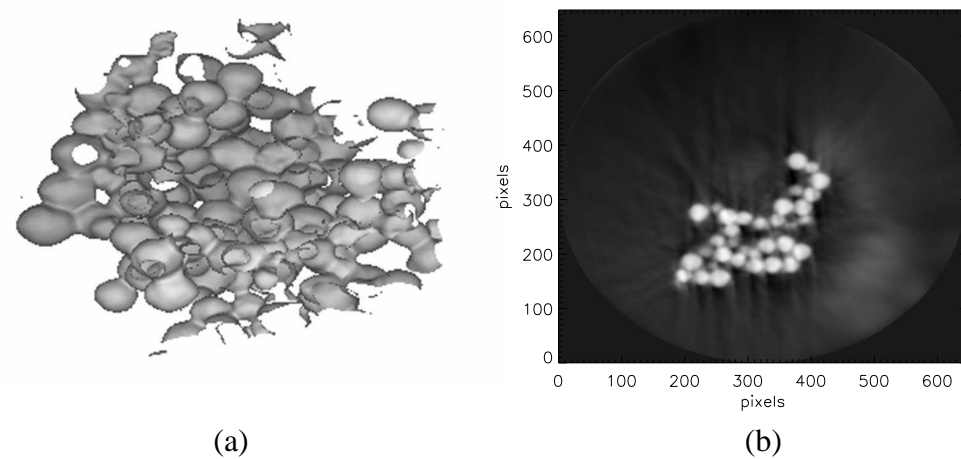


Figure 6.30: A surface rendering of a quantitative 3D reconstruction of the $20\mu\text{m}$ diameter polystyrene balls with the corresponding view of a single slice.

raw data. As discussed previously, the phase contrast image is edge enhanced. This can be confusing in a 3D visualization as it is hard to determine the true boundary of the object.

Applying the single plane TIE based phase retrieval of Equation 2.61 for each intensity projection and then implementing the filtered back projection algorithm, we get a *quantitative* tomographic reconstruction of the object, as shown in Figure 6.30. The confusion as to the edges of the overlapping object in 3D as seen in Figure 6.29 is now improved and the individual balls can be more clearly identified. The individual spheres (in white color) can now be resolved.

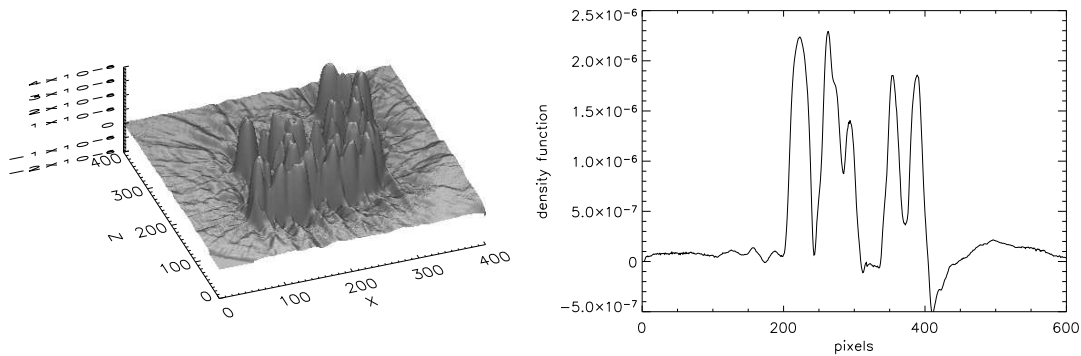


Figure 6.31: The density function of a reconstruction in one slice for the object in Figure 6.30(b), with a corresponding profile along x-axis, at $z = 275$.

Figure 6.31 shows the density function from the reconstruction in the slice shown in Figure 6.30(b) and a corresponding profile parallel to the x-axis at a constant $z = 275$. Most of the reconstructed spheres are close to the actual value of the refractive index (within 15%). At 10 keV, polystyrene (C_9H_{12}) with the density $1.05\text{gram}/\text{cm}^3$ has the refractive index value³ of $\delta = 2.3980 \times 10^{-6}$ and $\beta = 2.0869 \times 10^{-9}$. The correct value is revealed in the area around the center of the spheres. The edges roll off partly due to the shape of the balls so that not all voxels are "filled" with polystyrene and partly due to the blurring caused by the loss of high spatial frequency information and the effect of the Shepp-Logan filter as mentioned previously. It is also worth pointing

³The refractive index of polystyrene (C_9H_{12}) is retrieved from http://www-cxro.lbl.gov/optical_constants/.

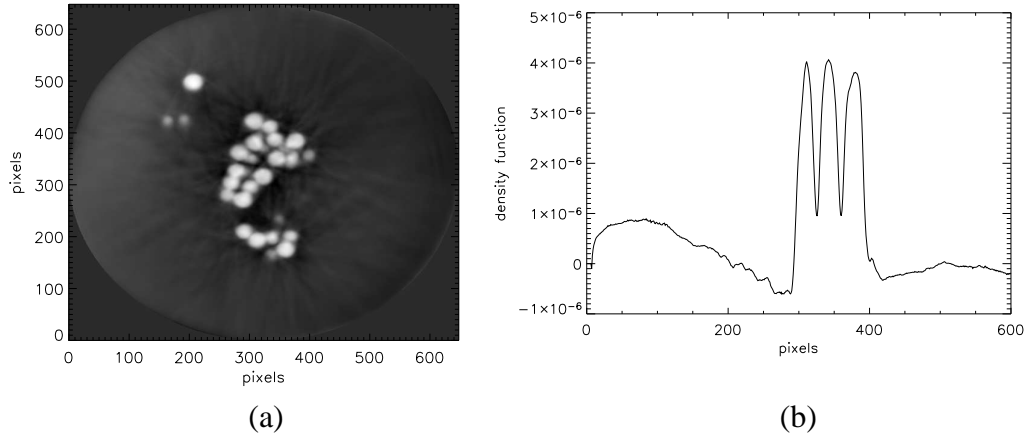


Figure 6.32: (a) A quantitative reconstruction in one slice of the $20\mu m$ diameter balls with an x-ray energy of 7 keV, (b) a corresponding profile at $z = 389$.

out that the geometric details of the object are correctly reconstructed. In the plot of Figure 6.31(b) the first peak represents one sphere. The FWHM of that peak consists of 28 pixels which corresponds to $21\mu m$ (since the detector has an effective pixel size of $0.735\mu m$). This is in a good agreement with the by the manufacturer's specified diameter of $20 \pm 3.2\mu m$. The dimension can be measured in the orthogonal direction also and again is in agreement with the specification.

Another data set was acquired at an energy of 7 keV for the $20\mu m$ spheres placed at a distance of 30 mm from the detector. At this energy, polystyrene has the refractive index components of $\delta = 4.9018 \times 10^{-6}$ and $\beta = 8.9087 \times 10^{-9}$. A quantitative reconstruction in one slice with a corresponding profile are shown in Figure 6.32. The reconstruction shows the density function within 17% of the actual value.

Polystyrene balls with a diameter of $75\mu m$ were used in the last data set which was acquired at an energy of 15 keV, and a propagation distance of 922 mm. At this energy, $\delta = 1.0647 \times 10^{-6}$ and $\beta = 4.5287 \times 10^{-10}$. The reconstruction result is shown in Figure 6.33 with the density function within 15% of the actual value.

The characteristic size of the source (σ_s) was $102\mu m$ horizontally and $35.1\mu m$ vertically. The source sample distance is $z_1 = 50m$. If we placed the detector at a distance $z_2 = 0.03m$ or $z_2 = 0.922m$, we will get image with magnification $M \approx 1$. Figure 6.34 shows the the theoretical quality function plotted with the quality of the recon-

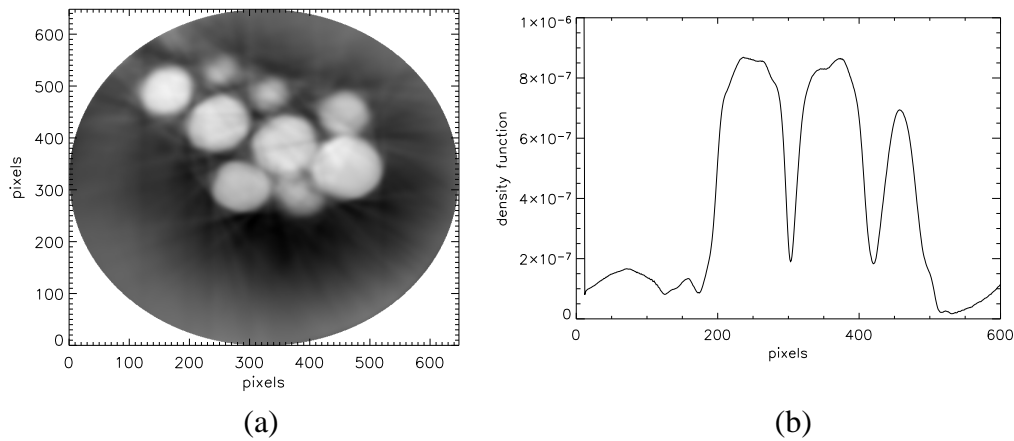


Figure 6.33: (a) A quantitative reconstruction in one slice of the $75\mu\text{m}$ diameter balls with an x-ray energy of 15 keV, (b) the corresponding profile at $z = 410$.

struction results for the three of the polystyrene balls. Note that the quality function is independent of the energy used.

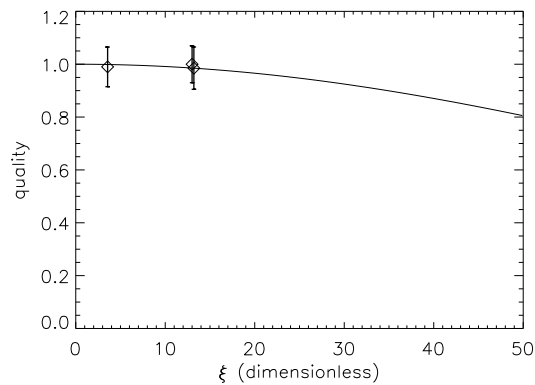


Figure 6.34: Theoretical quality function plotted against the experimental result for the 20 and $75\mu\text{m}$ spheres with $M \approx 1$.

We see from Figure 6.34 that the experimental results agree well with the theoretical predictions. While the agreement of the recovered phase with the theoretical predictions are not spectacular, we now know that for these object sizes the potential quality of the reconstruction is high. This would then give us confidence to apply the standard procedures to improve the accuracy of the phase retrieval. These procedures might include taking multiple data sets to improve signal to noise and applying our ob-

jective filtering criteria of Equation 4.22 and 4.23 to improve the reconstruction over a large range of spatial frequencies. This technique has the benefit of also introducing redundant data sets thus further improving signal to noise and hence the possible accuracy of the phase retrieval. This type of improvement in the data is similar to that demonstrated by Cloetens et al [Clo99a] in their "holotomography" results. Applying these methods is however beyond the scope of this thesis and we leave it as an avenue for further exploration.

In future work, an experiment using spherical wave illumination could also be performed to test the theory. This could be done using a micro computed tomography system from a lab based x-ray source or in a synchrotron source using a zone plate.

Chapter 7

Conclusion

7.1 Overview

Phase contrast imaging is a rapidly evolving field with many new developments based on its ability to image the complex refractive index of materials. We have developed an image formalism for phase contrast image formation using the propagation based phase contrast method. The formalism explicitly incorporated a partially coherent beam, which for x-ray sources can be closely related to source size and energy bandwidth. The optimum condition for image quality and its sensitivity to different spatial frequencies is described in the formalism.

This model is suitable for imaging experiment performed with a micro focus x-ray tube. Since x-ray tubes are compact and readily available, we believe that this study has great potential for applications in phase contrast imaging. A benefit of the model is that we can tailor an experiment to be sensitive to the desired feature sizes in the object thus maximizing the visibility of the image. An extended model has been also developed for 3D tomography phase contrast. This will benefit phase contrast radiography and tomography for light materials using hard x-rays.

7.2 Summary of results

In Chapter 2, the existing phase contrast imaging techniques, as a forward problem, were described including the free space propagation method. This imaging model used no lenses to form images and so is useful at x-ray wavelengths. The optimum contrast for a particular object size can be achieved at a particular propagation distance. Images obtained in the edge detection regime can be interpreted directly: this allows us to make use of Fresnel imaging as a direct imaging technique for hard x-rays. Different methods of phase retrieval for quantitatively extracting the phase were also described. The method chosen often depends on the imaging regime where the data has been acquired.

The experimental arrangement and installation that were used for the experimental work in this study, were described in Chapter 3. A micro focus x-ray source was used to do the experimental work in radiography for transparent and for complex objects. A synchrotron experiment was used to acquire the tomography data set. The detector resolution plays a major role in the case of plane wave illumination because it limits the spatial resolution in the recorded image and therefore also limits the resolution of the reconstruction image in the case of 3D phase contrast tomography.

An analytic expression for contrast using the imaging model was derived in Chapter 4 for pure phase samples. The image formation started by assuming that the sample is in the differential regime of propagation which limits the applicability primarily to very short wavelength radiation over short propagation distance. In this case the image magnification can still be achieved by using a spherical wave illumination that projects an enlarged diffraction pattern onto the detector. We limited our case to a small propagation distance in which the Transport of Intensity Equation is valid. Information related to the object, such as the image visibility, is the main purpose for calculating the image quality incorporating an extended source size. The model was then tested experimentally using a micro focus x-ray laboratory source, and the experimental results confirmed the validity of the theory. The model is then applied to develop methods for dealing with improving image quality. A description of the transfer of spatial frequency information (objective filtering) was used in Chapter 4 to propose a rational method for combining images obtained over a range of propagation distances in order to recover

a single high quality image. This objective filtering strategy is successfully applied at intensity data, phase recovery and experimental neutron data. In phase recovery data, this strategy was used in combining many retrieved phase images in the presence of noise. Phase images for short propagation distance are perfect for a wide range frequency features but are more sensitive to noise. Increases in propagation distance will reduce the effect of noise but the influence of source blurring becomes more apparent. A combination of both images using our objective filtering strategy resulted in one high quality image.

The imaging model was then extended to complex objects in Chapter 5. This study demonstrated the contribution of absorption and phase to the image contrast. Our formalism also explicitly included the role of a partially coherent source, which is closely related to source size and source spectral distribution. The effect of the source size in the case of high magnification image can be seen as a blurring of the image that limits the spatial resolution of the system. With the magnification close to unity, the effect of source blurring is negligible. The effect of the beam spectrum can be separated into two cases. Near an absorption edge, the phase contrast image shows some blurring and some shifting in the spatial frequencies. Far from an absorption edge, phase contrast using a polychromatic source showed the same result as for a monochromatic source when an equivalent energy calculated from the spectrally weighted sum was used. The experimental tests of the model using a micro focus x-ray source were found to be in excellent agreement with the theory. Application of the model to imaging micro cracks and corrosion in aluminium sheets proved that this analytical form of imaging is useful for selecting the optimum parameters for a given radiography experiment. The formalism was applied for an alternative method of source size measurement. In Chapter 5, we discussed the result for the short propagation distance region using the transport of intensity formalism, and for larger propagation distances using the contrast transfer function. It can be seen that a correct application of the two techniques has the potential to cover a broad range of practical application in x-ray radiography. Using the contrast transfer function, the variation in propagation distances were used to study Talbot effects for periodic objects.

Finally, an extended formalism for 3D tomography phase contrast for pure phase samples was derived in Chapter 6 which quantified a reconstruction quality factor as a function of object frequencies. The quantitative 3D reconstruction when phase retrieval was applied during the reconstruction steps, brings out the mapping of density function of an object. However, the common practice of 3D reconstruction directly from intensity data, showed only qualitatively important information about an object. A quantitative improvement in 3D reconstruction was demonstrated in the presence of noise by applying a frequency combination strategy for different propagation distances to the retrieved phase before applying the filtered back projection algorithm. The three dimensional distribution of the density function of polystyrene micro spheres was determined experimentally. The results show the agreement with the theoretical predictions.

7.3 Suggestions for further research

Chapter 6 described an extended formalism for 3D tomographic phase contrast for pure phase samples. It would be interesting to extend the formalism for complex objects and thus show the ability to separate between absorption and phase contributions in the image reconstruction. Further work could also include taking multiple data sets to improve signal to noise and to extend the frequency response of the reconstructed data set. Experimental work using spherical wave illumination would also be worthwhile to evaluate the theory for a broader region of spatial frequencies for the object. Performing image deconvolution using the known source properties is also worth exploring for the purpose of increasing the high spatial frequency reconstructions.

Appendix A

Publications

I have contributed the following refereed publications during the course of my PhD candidature, in addition to a number of conference presentations.

- B.D. Arhatari, A.P. Mancuso, A.G. Peele, K.A. Nugent, *Phase contrast radiography: Image modelling and optimization*, Review of Scientific Instruments, 75 (12), 5271-6, (2004).
- B.D. Arhatari, K.A. Nugent, A.G. Peele, J. Thornton, *Phase contrast radiography II: Imaging of complex object*, Review of Scientific Instruments, 76 (1), 1137041-6, (2005).
- J. Thornton, B.D. Arhatari, A.G. Peele, K.A. Nugent, *Optimizing visibility for the neutron radiography of titanium and nickel gas turbine components*, Elsevier Science (accepted).
- A.G. Peele, H.M. Quiney, B.B. Dhal, A.P. Mancuso, B.D. Arhatari, K.A. Nugent *New Opportunities in X-ray Tomography*, Elsevier Science (accepted).
- B.D. Arhatari, K.A. Nugent, A.G. Peele, *Phase Contrast Imaging with a micro-focus x-ray source*, Oral presentation at 8th International Conference on Optics within Life Sciences, Nov 2004, Melbourne, Victoria.
- B.D. Arhatari, K.A. Nugent, A.G. Peele, *Phase Contrast Imaging with a micro-focus source*, Poster presentation at ACOLS 03 (Australasian conference on Optics, Lasers and Spectroscopy), Dec 2003, The University of Melbourne, Victoria.

Bibliography

- [Abo00] A.O. Aboyan. Investigation of deformation fields in ion-implanted analyzing crystal of x-ray interferometer. *Journal of Contemporary Physics*, 35(4):38–44, 2000.
- [All00] B. E. Allman, P. J. McMahon, K. A. Nugent, D. Paganin, D. L. Jacobson, and S. A. Arif, M. Werner. Phase radiography with neutrons. *Nature (London)*, 408:158–9, 2000.
- [Amp98] MCA8000 and XR-100CR User’s Manual. Amptek inc. website: <http://www.amptek.com>.
- [And72] M. Ando and S. Hosoya. An attempt at x-ray phase-contrast microscopy. *Proc. 6th Intern. Conf. on X-ray Optics and Microanalysis*, pages 63–68, 1972.
- [Arh04] B.D. Arhatari, A.P. Mancuso, A.G. Peele, and K. A. Nugent. Phase contrast radiography: Image modelling and optimization. *Review of Scientific Instruments*, 75(12):5271–6, 2004.
- [Arh05] B.D. Arhatari, K. A. Nugent, A.G. Peele, and J. Thornton. Phase contrast radiography II: Imaging of complex objects. *Review of Scientific Instruments*, 76(1):1137041–6, 2005.
- [Baj00] S. Bajt, A. Barty, K.A. Nugent, M. McCartney, M. Wall, and D. Paganin. Quantitative phase-sensitive imaging in a transmission electron microscope. *Ultramicroscopy*, 83(1-2):67–73, 2000.
- [Ban91] P.P. Banerjee and T.C. Poon. *Principles of Applied Optics*. Aksen Associates Incorporated Publishers, 1991. ISBN: 0-256-08860-8.
- [Bar00] A. Barty, K.A. Nugent, A. Roberts, and D Paganin. Quantitative phase tomography. *Optics Communications*, 175:329–36, 2000.

- [Bar81] H.H. Barrett and W. Swindell. *Radiological imaging (The theory of image formation, detection, and processing)*, vol. 2. Academic press inc., 1981. ISBN 0-12-079602-3 (vol. 2).
- [Bar98] A. Barty, K.A. Nugent, D. Paganin, and A. Roberts. Quantitative optical phase microscopy. *Optics Letters*, 23(11):1–3, 1998.
- [Bar99] A. Barty. *Quantitative Phase-Amplitude Microscopy*. PhD thesis, School of Physics, University of Melbourne, 1999.
- [Bon00] U. Bonse, F. Beckmann, and T. Biermann. X-ray microtomography (μ CT) using interferometric phase contrast. *AIP Conference Proceedings*, (507):69–75, 2000.
- [Bon65] U. Bonse and M. Hart. An x-ray interferometer. *Applied Physics Letters*, 6(8):155–6, 1965.
- [Bor99] M. Born and E. Wolf. *Principles of Optics*. Cambridge university press, 7th edition, 1999.
- [Bro99] A.V. Bronnikov. Reconstruction formulas in phase-contrast tomography. *Optics Communications*, 171:239–44, 1999.
- [Bur84] P. Burstein, P. J. Bjorkholm, R. C. Chase, and F. H. Seguin. The largest and smallest x-ray computed tomography systems. *Nuclear Instruments and Methods in Physics Research*, 221(1):207–12, 1984.
- [Clo01] P. Cloetens, E. Boller, W. Ludwig, J. Baruchel, and M. Schlenker. Absorption and phase imaging with synchrotron radiation. *Europhysics News*, 32(2), 2001.
- [Clo96] P. Cloetens, R. Barrett, J. Baruchel, J.P. Guigay, and M. Schlenker. Phase objects in synchrotron radiation hard x-ray imaging. *Journal of Physics D-Applied Physics*, 29:133–46, 1996.
- [Clo97a] P. Cloetens, M. Pateyron-Salome, J. Y. Buffiere, G. Peix, F. Baruchel, J. Peyrin, and M. Schlenker. Observation of microstructure and damage in materials by phase sensitive radiography and tomography. *Journal of Applied Physics*, 81(9):5878–86, 1997.
- [Clo97b] P. Cloetens, J.P. Guigay, C. De Martino, and J. Baruchel. Fractional talbot imaging of phase gratings with hard x-ray. *Optics Letters*, 22(14):1059–61, 1997.

- [Clo99a] P. Cloetens, W. Ludwig, J. Baruchel, D. Van Dijck, J. Van Landuijt, JP. Guigay, and M. Schlenker. Holotomography: Quantitative phase tomography with micrometer resolution using hard synchrotron radiation x-rays. *Applied Physics Letters*, 75:2912–4, 1999.
- [Clo99b] P. Cloetens. *Contribution to phase contrast imaging, reconstruction and tomography with hard synchrotron radiation*. PhD thesis, Faculteit Toegepaste Wetenschappen, Vrije Universiteit Brussel, 1999.
- [Coe92] W. Coene and G. Janssen. Phase retrieval through focus variation for ultra resolution in field emission transmission electron microscopy. *Physical Review Letters*, 69(26):3743–6, 1992.
- [Cow95] J.M. Cowley. *Diffraction Physics*. North-Holland, Amsterdam, 3rd revised edition, 1995.
- [Dav95] T. J. Davis, D. Gao, T. E. Gureyev, A. W. Stevenson, and S. W. Wilkins. Phase-contrast imaging of weakly absorbing materials using hard x-rays. *Nature*, 373(6515):595–8, 1995.
- [Fie72] J.R. Fiebigler and R.S. Muller. Pair production energies in silicon and germanium bombarded with low-energy electrons. *Journal of Applied Physics*, 43:3202, 1972.
- [Fie82] J.R. Fienup. Phase retrieval algorithms: a comparison. *Applied Optics*, 21(15):2758–69, 1982.
- [Fod03] I.M. Fodchuk and N. Raransky. Moire images simulation of strains in x-ray interferometry. *Journal of Physics D (Applied Physics)*, 36(10A):A55–9, 2003.
- [Gao95] D. Gao, T.J. Davis, and S. W. Wilkins. X-ray phase contrast imaging study of voids and fibres in a polymer matrix. *Australian Journal of Physics*, 48:103–11, 1995.
- [Gao98] D. Gao, A. Pogany, A. W. Stevenson, and S. W. Wilkins. Phase-contrast radiography. *Imaging and Therapeutic Technology*, 18(5):1257–67, 1998.
- [Gas99] J. Gastaldi, L. Mancini, E. Reinier, P. Cloetens, W. Ludwig, C. Janot, J. Baruchel, J. Hartwig, and M. Schlenker. The interest of x-ray imaging for the study of defects in real quasicrystals. *Journal of Physics D-Applied Physics*, 32(10A):A152–9, 1999.

- [Ger72] R.W. Gerchberg and W.O. Saxton. A practical algorithm for the determination of phase from image and diffraction plane pictures. *Optik*, 35(2):237–46, 1972.
- [Gui77] J.-P. Guigay. Fourier transform analysis of fresnel diffraction patterns and in-line holograms. *Optik*, 49:121–5, 1977.
- [Gur00] T. E. Gureyev, A. W. Stevenson, D. Paganin, S. C. Mayo, A. Pogany, D. Gao, and S. W. Wilkins. Quantitative methods in phase-contrast x-ray imaging. *Journal of Digital Imaging*, 13(2):121–6, 2000.
- [Gur01] T. E. Gureyev, S. Mayo, S. W. Wilkins, D. Paganin, and A. W. Stevenson. Quantitative in-line phase-contrast imaging with multienergy x rays. *Physical Review Letters*, 86(25):5827–30, 2001.
- [Gur03] T. E. Gureyev. Composite techniques for phase retrieval in the fresnel region. *Optics Communications*, 220:49–58, 2003.
- [Gur04] T. E. Gureyev, A. Pogany, D. M. Paganin, and S. W. Wilkins. Linear algorithms for phase retrieval in the fresnel region. *Optics Communications*, 231:53–70, 2004.
- [Gur95] T. E. Gureyev, A. Roberts, and K. A. Nugent. Partially coherent fields, the transport-of-intensity equation, and phase uniqueness. *Journal of the Optical Society of America A-Optics & Image Science*, 12(5):1942–6, 1995.
- [Gur98] T. E. Gureyev and S. W. Wilkins. X-ray phase imaging with a point source. *Journal of the Optical Society of America A-Optics & Image Science*, 15(3):579–85, 1998.
- [Hal79] R. Halmshaw. Defect size measurement by radiography. *British Journal of Non-Destructive Testing*, 21(5):245–8, 1979.
- [Hec97] E. Hecht. *Optics*. Addison-Wesley Publishing Co. Inc., 2nd edition, 1987.
- [Her79] G.T. Herman. *Image reconstruction from projections*. Springer-Verlag Berlin Heidelberg New York, 1979.
- [Hwu02] Y. Hwu, W. Tsai, A. Groso, G Margaritondo, and J.H. Je. Coherence-enhanced synchrotron radiology: simple theory and practical applications. *Journal of Physics D: Applied Physics*, 35:R105–20, 2002.

- [Ing95] V. N. Ingal and E. A. Beliaevskaya. X-ray plane-wave topography observation of the phase contrast from a non-crystalline object. *Journal of Physics D: Applied Physics*, 28(11):2314–17, 1995.
- [Ing98] V. N. Ingal, E. A. Beliaevskaya, A. P. Brianskaya, and R. D. Merkurieva. Phase mammography - a new technique for breast investigation. *Physics in Medicine and Biology*, 43(9):2555–67, 1998.
- [Jon04] P. Jonas and Louis A.K. Phase contrast tomography using holographic measurements. *Inverse Problems*, 20:75–102, 2004.
- [Kak88] A.C. Kak and M. Slaney. *Principles of Computerized Tomographic Imaging*. IEEE Press, New York, 1988. ISBN 0-87942-198-3.
- [Lum90] D.H. Lumb. Calibration and x-ray spectroscopy with silicon CCDs. *Nuclear Instruments and Methods in Physics Research*, A290:559–64, 1990.
- [Mad89] J.U. Madsen. Focal spot size measurements for microfocus x-ray sets. *NDT International*, 22(5):292–6, 1989.
- [Maj96] B. Maj, P.H.A. Mutsaers, E. Rokita, and M. J. A. de Voigt. Determination of the microbeam profile using deconvolution procedures. *Nuclear Instruments and Methods in Physics Research Section B: Beam Interactions with Materials and Atoms*, 113(1-4).
- [Man95] L. Mandel and E. Wolf. *Optical Coherence and Quantum Optics*. Cambridge University Press, 1995. ISBN 0 521 41711 2.
- [May02] S. C. Mayo, P. R. Miller, S. W. Wilkins, T. J. Davis, D. Gao, T. E. Gureyev, D. Paganin, D. J. Parry, A. Pogany, and A. W. Stevenson. Quantitative x-ray projection microscopy: phase-contrast and multi-spectral imaging. *Journal of Microscopy*, 207:79–96, 2002.
- [May03] S. C. Mayo, T. J. Davis, T. E. Gureyev, P. R. Miller, D. Paganin, A. Pogany, A. W. Stevenson, and S. W. Wilkins. X-ray phase-contrast microscopy and microtomography. *Optics Express*, 11(19):2289–302, 2003.
- [McM01] P. J. McMahon, B. E. Allman, K. A. Nugent, D. L. Jacobson, M. Arif, and S. A. Werner. Contrast mechanisms for neutron radiography. *Applied Physics Letters*, 78(7):1011–13, 2001.

- [McM03a] P. J. McMahon, A. G. Peele, D. Paterson, J.J.A. Lin, T.H.K. Irving, I. McNulty, and K. A. Nugent. Quantitative x-ray phase tomography with sub-micron resolution. *Optics Communications*, 217:53–8, 2003.
- [McM03b] P. J. McMahon, A. G. Peele, D. Paterson, K. A. Nugent, A. Snigirev, T. Weitkamp, and C. Rau. X-ray tomographic imaging of the complex refractive index. *Applied Physics Letters*, 83(7):1480–2, 2001.
- [McM03c] P. J. McMahon, B.E. Allman, D.L. Jacobson, M Arif, S.A. Werner, and K. A. Nugent. Quantitative phase radiography with polychromatic neutrons. *Physical Review Letters*, 91(14):1455021–4, 2003.
- [Mom03] A. Momose. Phase-sensitive imaging and phase tomography using x-ray interferometers. *Optics Express*, 11(19):1303–14, 2003.
- [Mom95] A. Momose, T. Takeda, and Y. Itai. Phase-contrast x-ray computed tomography for observing biological specimens and organic materials. *Review of Scientific Instruments*, 66(2):1434–6, 1995.
- [Nat86] F. Natterer. *The mathematics of computerized tomography*. John Wiley & Sons Ltd and B G Teubner, Stuttgart, 1986. ISBN: 0 471 90959 9.
- [Nug03] K. A. Nugent, A.G. Peele, H.N. Chapman, and A.P. Mancuso. Unique phase recovery for nonperiodic objects. *Physical review Letters*, 91(20):2039021–4, 2003.
- [Nug91] K. A. Nugent. Partially coherent diffraction patterns and coherence measurement. *Journal of the Optical Society of America A*, 8(10):1574–9, 1991.
- [Nug96] K. A. Nugent, T. E. Gureyev, D. F. Cookson, D. Paganin, and Z. Barnea. Quantitative phase imaging using hard x rays. *Physical Review Letters*, 77(14):2961–4, 1996.
- [Pag01] D. Paganin and K. A. Nugent. Non-interferometric phase determination. *Advances in Imaging and Electron Physics*, 118:85–127, 2001.
- [Pag02] D. Paganin, S. Mayo, T. E. Gureyev, P. R. Miller, and S. W. Wilkins. Simultaneous phase and amplitude extraction from a single defocused image of a homogeneous object. *Journal of Microscopy (Paris)*, 206:33–40, 2002.

- [Pag04a] D. Paganin, A. Barty, P.J. McMahon, and K. A. Nugent. Quantitative phase-amplitude microscopy. III. The effects of noise. *Journal of Microscopy*, 214(12):51–61, 2004.
- [Pag04b] D. Paganin, T.E. Gureyev, K.M. Pavlov, R.A. Lewis, and M. Kitchen. Phase retrieval using coherent imaging systems with linear transfer functions. *Optics Communications*, 234:87–105, 2004.
- [Pag98] D. Paganin and K. A. Nugent. Noninterferometric phase imaging with partially coherent light. *Physical Review Letters*, 80(12):2586–9, 1998.
- [Pag99] D. Paganin. *Studies in phase retrieval*. PhD thesis, School of Physics, University of Melbourne, 1999.
- [Par54] L.G. Parratt. Surface studies of solids by total reflection of x-rays. *Physical Review*, 95:359–69, 1954.
- [Pee05] A.G. Peele, F. De Carlo, P.J. McMahon, B.B. Dhal, and K. A. Nugent. X-ray phase contrast tomography with a bending magnet source. *Review of Scientific Instruments*, 76(8):83707–1–5, 2005.
- [Pog97] A. Pogany, D. Gao, and S. W. Wilkins. Contrast and resolution in imaging with a microfocus x-ray source. *Review of Scientific Instruments*, 68(7):2774–82, 1997.
- [Pre88] W.H. Press, B.P. Flannery, S.A. Teukolsky, and W.T. Vetterling. *Numerical recipes in C: The art of scientific computing*. Cambridge University Press, Cambridge, 1988.
- [Ric98] R.A. Richardson and T.L. Houck. Roll bar x-ray spot size measurement technique. *Joint Accelerator Conferences Website*, LINAC98(TH4063), 1998, <http://accelconf.web.cern.ch/accelconf/198/papers/TH4063.pdf>.
- [Rob75] A. Robinson and G.M. Grimshaw. Measurement of the focal spot size of diagnostic x-ray tubes - a comparison of pinhole and resolution methods. *British Journal of Radiology*, 48:572–80, 1975.
- [Sch94] G. Schmahl, D. Rudolph, G. Schneider, P. Guttmann, and B. Niemann. Phase contrast x-ray microscopy studies. *Optik*, 97(4):181–2, 1994.

- [Sni95] A. Snigirev, I. Snigireva, V. Kohn, S. Kuznetsov, and I. Schelokov. On the possibilities of x-ray phase contrast microimaging by coherent high-energy synchrotron radiation. *Review of Scientific Instruments*, 66(12):5486–92, 1995.
- [Spa99] P. Spanne, C. Raven, I. Snigireva, and A. Snigirev. In-line holography and phase-contrast microtomography with high energy x-rays. *Physics in Medicine and Biology*, 44(3):741–9, 1999.
- [Ste99] A. W. Stevenson, D. Gao, T. E. Gureyev, A. Pogany, and S. W. Wilkins. Hard x-ray phase-contrast imaging with a microfocus source. *Nondestructive Characterization of Materials IX*, CP497:641–8, 1999.
- [Tea83] M. R. Teague. Deterministic phase retrieval: a green’s function solution. *Journal of the Optical Society of America*, 73(11):1434–1441, 1983.
- [Tho05] J. Thornton, B.D. Arhatari, A.G. Peele, and K.A. Nugent. Optimising visibility for the neutron radiography of titanium and nickel gas turbine components. (*a manuscript is in preparation to be published in Elsevier Science*).
- [Tik63] A.N. Tikhonov. Solution of incorrectly formulated problems and the regularization method. *Soviet Mathematics Doklady*, 4:1035–8, 1963.
- [Tot05] R. Toth, J.C. Kieffer, S. Fourmaux, and T. Ozaki. In-line phase contrast imaging with a laser-based hard x-ray source. *Review of Scientific Instruments*, 76:0837011–6, 2005.
- [Tur04a] L. D. Turner, A.G. Peele, B. Dhal, A.P. Mancuso, R. E. Scholten, C. Q. Tran, K. A. Nugent, J. P. Hayes, and D Paterson. X-ray phase imaging: Demonstration of extended conditions for homogeneous objects. *Optics Express*, 12(13):2960–5, 2004.
- [Tur04b] L.D. Turner. *Holographic imaging of cold atoms*. PhD thesis, School of Physics, University of Melbourne, 2004.
- [Wan01] Y. Wang, F. De Carlo, D.C. Mancini, I. McNulty, B. Tieman, J. Bresnahan, I. Foster, J. Insley, P. Lane, G. von Laszewski, C. Kesselman, Mei-Hui Su, and M. Thiebaux. A high-throughput x-ray microtomography system at the advanced photon source. *Review of Scientific Instruments*, 72(4):2062–8, 2001.

- [Wat79] T. Watanabe. The mottling appearing on radiographs of stainless steel weldments and castings. *British Journal of Non-Destructive Testing*, 21(6):299–307, 2004.
- [Wil96] S. W. Wilkins, T. E. Gureyev, D. Gao, A. Pogany, and A. W. Stevenson. Phase-contrast imaging using polychromatic hard x-rays. *Nature (London)*, 384(6607):335–8, 1996.
- [Win95] H. Winick. *Synchrotron Radiation Sources*. World Scientific, 1995.
- [Wu03] X. Wu and H. Liu. A general theoretical formalism for x-ray phase contrast imaging. *Journal of X-Ray Science and Technology*, 11:33–42, 2003.
- [Wu05] X. Wu, H. Liu, and A. Yan. X-ray phase attenuation duality and phase retrieval. *Optics Letters*, 30(4):379–381, 2005.
- [Zab05] S. Zabler, P. Cloetens, J.-P. Guigay, J. Baruchel, and M. Schlenker. Optimization of phase contrast imaging using hard x-rays. *Review of Scientific Instruments*, 76:0737051–7, 2005.
- [Zak04] B. Zakharin and J. Stricker. Schlieren systems with coherent illumination for quantitative measurements. *Applied Optics*, 43(25):4786–95, 2004.
- [Zer42] F. Zernike. Phase contrast, a new method for the microscopic observation of transparent objects. *Physica*, IX(7):686–93, 1942.
- [cxr95] The center for x-ray optics (CXRO) at Lawrence Berkeley National Laboratory. X-ray interactions with matter. http://www.cxro.lbl.gov/optical_constants/.
- [fei93a] Fein Focus Röntgen Systeme GmbH in Garbsen (Germany). website: <http://web.feinfocus.com/index.html>.
- [fei93b] Manual of X-ray system FXE-160.50. Fein focus röntgen - systeme gmbh.



Minerva Access is the Institutional Repository of The University of Melbourne

Author/s:

Arhatari, Benedicta Dewi

Title:

High resolution phase contrast x-ray radiography

Date:

2006

Citation:

Arhatari, B. D. (2006). High resolution phase contrast x-ray radiography, PhD thesis, School of Physics, University of Melbourne.

Publication Status:

Unpublished

Persistent Link:

<http://hdl.handle.net/11343/39074>

File Description:

High resolution phase contrast x-ray radiography

Terms and Conditions:

Terms and Conditions: Copyright in works deposited in Minerva Access is retained by the copyright owner. The work may not be altered without permission from the copyright owner. Readers may only download, print and save electronic copies of whole works for their own personal non-commercial use. Any use that exceeds these limits requires permission from the copyright owner. Attribution is essential when quoting or paraphrasing from these works.